

Universiteit
Leiden
The Netherlands

The Great Collapse

Caputo, D.P.

Citation
Caputo, D. P. (2015, January 22). *The Great Collapse*. *PhD Thesis*. Retrieved from https://hdl.handle.net/1887/31710

Version:	Not Applicable (or Unknown)
License:	Leiden University Non-exclusive license
Downloaded from:	https://hdl.handle.net/1887/31710

Note: To cite this publication please use the final published version (if applicable).

Cover Page



Universiteit Leiden



The handle http://hdl.handle.net/1887/31710 holds various files of this Leiden University dissertation.

Author: Caputo, Daniel P.
Title: The Great Collapse
Issue Date: 2015-01-22

The Great Collapse

Daniel P Caputo

Cover: “The Treachery of Simulations” by author.
ISBN: 978-94-6108-917-5
© 2015 Daniel Caputo

The Great Collapse

Proefschrift

ter verkrijging van
de graad van Doctor aan de Universiteit Leiden,
op gezag van Rector Magnificus prof. mr. C.J.J.M. Stolker,
volgens besluit van het College voor Promoties
te verdedigen op donderdag 22 januari 2015
klokke 13:45 uur

door

Daniel P Caputo
geboren te Massachusetts, USA
in 1981

Promotiecommissie

Promotor:	Prof. dr. Simon Portegies Zwart	
Overige leden:	Dr. Alessandro Patruno	(Universiteit Leiden)
	Prof. dr. Roberto Capuzzo Dolcetta	(Sapienza–Università di Roma)
	Prof. dr. Thomas Tauris	(Universität Bonn)
	Prof. dr. Huub Röttgering	(Universiteit Leiden)

To Samantha, my love, at the end
of our European honeymoon.

Contents

1 Introduction **1**
1.1 This Work . . . 3
1.1.1 Initial Virial Temperature (Chapter 2) . . . 3
1.1.2 Mass Segregation in a Collapsing Cluster (Chapter 3) . 4
1.1.3 The Number of IMBHs (Chapter 4) . . . 4
1.1.4 Supernova in Hierarchical Star Systems (Chapter 5) . 4

2 Subvirial Systems **7**
2.1 Introduction . . . 8
2.1.1 Violent Relaxation . . . 8
2.1.2 Notation . . . 9
2.2 Simulations . . . 9
2.2.1 AMUSE . . . 9
2.2.2 Initial Conditions . . . 10
2.3 Results and Discussion . . . 11
2.3.1 Escape Fraction . . . 12
2.3.2 Mass Segregation . . . 15
2.3.3 Time-scales . . . 19
2.3.4 Minimum Cluster Radius . . . 21
2.3.5 Observables . . . 22
2.4 Application to an observed cluster: R136 . . . 24
2.4.1 Observed Parameters . . . 24
2.4.2 From N-body to Physical Units . . . 25
2.4.3 Initial Virial Temperature of R136 . . . 27
2.4.4 Other Young Clusters . . . 29
2.5 Conclusion . . . 30

3 Mass Segregation **33**
3.1 Introduction . . . 34

3.2 Method . . . 34
3.2.1 Minimum Spanning Tree Method . . . 35
3.2.2 Nearest Neighbor Method . . . 35
3.3 Comparing Results . . . 36
3.3.1 Measurements of the Mass Segregation . . . 36
3.3.2 Speed . . . 40
3.4 Results and Discussion . . . 42
3.4.1 Simulation Methods . . . 42
3.4.2 Mass Segregation . . . 43
3.4.3 Effect of the Initial FoV on Mass Segregation . . . 46
3.5 Conclusion . . . 47

4 Number of Intermediate Mass Black Holes **49**
4.1 Introduction . . . 50
4.2 Observational Constraints HLX-1 and M82 X-1 . . . 50
4.3 Methods . . . 51
4.3.1 Mass Transfer . . . 52
4.3.2 Mass Function . . . 53
4.4 Results and Discussion . . . 54
4.4.1 The Mass of HLX-1's Companion and the Mass Function Around the IMBH . . . 55
4.4.2 The Number of IMBHs . . . 56
4.4.3 IMBHs in Relation to Other Black Holes . . . 58
4.5 Conclusion . . . 59
4.6 Acknowledgments . . . 60

5 Supernova in Multiple-Star Systems **63**
5.1 Introduction . . . 64
5.2 Calculation of post-SN parameters . . . 65
5.2.1 Binary systems . . . 65
5.2.2 Hierarchical triple systems . . . 70
5.2.3 An example of the effect of a supernova in a hierarchical triple . . . 76
5.2.4 Hierarchical systems of multiplicity > 3 . . . 78
5.3 Application: Formation of J1903+0327 . . . 83
5.3.1 Initial conditions . . . 84
5.3.2 Simulations . . . 85
5.4 Conclusion . . . 90
5.5 Acknowledgements . . . 91

6 Summary **93**
6.1 The Role of Simulations 94
6.2 Collapsing Clusters 95
6.2.1 Taking a Star Cluster's Temperature 95
6.2.2 Why do all of the Big Stars Clump Together? 96
6.3 Collapsing Stars 97
6.3.1 Supernova 97
6.3.2 Intermediate Mass Black Holes 98

7 Samenvatting **99**
7.1 De rol van simulaties 100
7.2 Instortende sterrenhopen 101
7.2.1 De temperatuur van een sterrenhoop bepalen 102
7.2.2 Waarom klonteren alle grote sterren samen? 103
7.3 Ineenstortende Sterren 104
7.3.1 Supernova 104
7.3.2 Middelgrote Zwarte Gaten 105

List of publications **107**

Bibliography **109**

Curriculum Vitae **119**

Acknowledgements **121**

CHAPTER 1 Introduction

Stars are the fundamental unit of astronomy. In this thesis I will explore the nature of various types of collapse on stars and star systems.

Stars can be found alone, individual bodies moving through space; or they can be gravitationally bound to one or a few other stars, moving through space together. Of particular interest here are stars in groups of three. Such triple systems can be found in different configurations; the stars may all have orbits, about their collective center of mass, of comparable size in which case the system is very likely to be dynamically unstable due to strong interactions between the stars, though there are some configurations of this type which are stable they occupy a very small fraction of the relevant orbital parameter space. In a hierarchical triple on the other hand, the stars have orbits such that the inner two stars are relatively tightly bound while the third star is much farther away, this *tends* to produce dynamically stable systems.

If one of the stars in a hierarchical triple, or any other stable multiple system, undergoes a supernova—wherein the star's core begins to collapse and then rebounds producing an incredibly powerful explosion—causing the star to almost instantaneously lose the majority of its mass the dynamical stability of the system is placed in jeopardy due to the change in the gravitational force between the stars. This effect in binary systems has been studied many times by Blaauw (1961) and Boersma (1961), Hills (1983), and Tauris and Takens (1998). Complicating matters are the effects of the shell impact on the companion and the supernova kick.

After the supernova the remnant core of the star may become a neutron star, and if that neutron star has a companion which evolves and begins to overflow its Roche lobe causing material to be accreated onto the neutron star it may begin to rotate faster and faster from the transfer of angular moment from the accreating material. This is the suggested formation mechanism for a class of objects called millisecond pulsars. These objects rotate once every few milliseconds.

However, if the supernova progenitor was massive enough, around 20 $M_{\odot}$,

it would not form a neutron star but it would collapse into a stellar mass black hole. There are three astronomically relevant classes of black holes, stellar mass, intermediate mass, and supermassive. Stellar mass black holes have masses <50 or 100 $M_\odot$; supermassive black holes have masses >10^6 $M_\odot$; and intermediate mass black holes have masses between those ranges. Supermassive and stellar mass black hole have been identified with strong constraints placed on their masses, however intermediate mass black holes have never been definitively identified.

Currently there are several intermediate mass black hole (IMBH) candidates; currently the strongest IMBH candidate is the hyperluminous X-ray source HLX-1 with mass estimates generally given to be between some 10^3 and 10^5 $M_\odot$. M82 X-1 is also a strong IMBH candidate with mass estimates ranging from a couple $\times 10^2$ and 10^3 $M_\odot$.

The collapse of star clusters is the result of there being too little kinetic energy relative to potential energy. We know from the virial theorem that in a stable system the time-averaged kinetic energy will be $^1/_2$ the potential energy of the system. If the stars in a cluster have too little kinetic energy, meaning it is subvirial, the system will contract. The inverse is also true, if the stars have too much kinetic energy, supervirial, the system will expand. When a system is subvirial it will experience a radial contraction and a corresponding phase of high density, the collapse, during which time extreme dynamical processes can occur, including violent relaxation.

Violent relaxation was coined by Lynden-Bell (1967) to describe the "violently changing gravitational field of a newly formed galaxy". The theory is rooted in the idea that stars in a collapsing model may be treated as a large set of independent, non-interacting harmonic oscillators. These oscillators treated statistically are expected to find a state of maximum entropy. Thus in a subvirial cluster we would expect to find the effects of violent relaxation.

One possible effect of violent relaxation is very rapid mass segregation[1] of the cluster. Mass segregation has been observed in young clusters, whose age constrains the more common mechanism for mass segregation, i.e. two-body relaxation. It was suggested (Bonnell and Davies 1998) that such rapid mass segregation was not the result of a dynamical mechanism, however this was found to be incorrect by Allison et al. (2009a). What had remained not well understood was when during the collapse, and exactly by what mechanism this rapid dynamical mechanism was occurring.

Two different mechanisms were suggested, which occur at different times

[1] where massive objects are statistically more likely to be found near other massive objects than objects of arbitrary mass

during the collapse. Allison et al. (2009a) first suggested that subvirial collapsing clusters mass segregate more quickly than might be expected due to the dense core formed as the end of the collapse. Whereas, McMillan et al. (2012) claimed that this rapid mass segregation happens not around the time of the "high density bounce", but rather during the entire collapse via the formation of subclumps which mass segregate independently.

In order to investigate and hopefully gain some understanding of these physical systems we have employed the use of computer simulations. We have used codes that calculate the pair-wise gravitational force between stars, codes that model the evolution of stars, and codes which solves sets of analytic solutions we developed to calculate the effects of a supernova in a hierarchical triple. Most, if not all, of this work would be impossible to complete without efficient codes to run, and at least once we had to develop new methods which were fast enough to run the analysis we needed.

With the exception of Chapter 5 all the simulations presented in this work were run in the AMUSE environment. AMUSE is a modular simulation platform which, through a PYTHON interface, links together to a set of simulation codes. Different codes can easily be used on the same initial conditions, allowing for a fast, simple, and clear test of consistency between codes; AMUSE's modular nature makes this easy to do, usually requiring a change to only two lines of code.

The benefit of its modular design is not only being able to test, and thus verify, different codes against one another, but also the ease with which one can add additional physics. For example, including stellar evolution in a hydrodynamics simulation is relatively easy compared to having to merge two codes together by hand.

1.1 This Work

1.1.1 Initial Virial Temperature (Chapter 2)

We investigate the effect of the initial virial temperatures on the dynamics of star clusters and find a strong relationship between the initial virial temperature and many dynamical processes. We investigate in depth the likely initial virial temperature of the young cluster R136 along with 15 other young clusters; we find that the most likely value for the initial virial temperature in all of the clusters we tested to be between $\approx$0.18 and 0.25.

1.1.2 Mass Segregation in a Collapsing Cluster (Chapter 3)

Building off of the simulations from Chapter 2 we attempt to isolate the mechanism by which rapid mass segregation occurs in young clusters. In order to measure the mass segregation for the large data sets we had it was necessary to first develop a new method for measuring the systems mass segregation. We detail the increase in accuracy in measuring mass segregation in complex systems as well as the dramatic increase in speed from our new method. After performing a computational experiment we are able to show the greater role the dense part of the collapse plays in rapid mass segregation.

1.1.3 The Number of IMBHs (Chapter 4)

In this chapter we make an estimate of the number of IMBHs within 100 Mpc, based on the nature of HLX-1 and M81 X-1, and stellar evolution simulations. We expect, within the limits of our assumptions, that there should be of order 10^8 IMBHs within that volume. Furthermore, from the results of our simulations we find a constraint on the mass of HLX-1's proposed stellar companion to have a mass between $\approx$10 and 11 $M_\odot$.

1.1.4 Supernova in Hierarchical Star Systems (Chapter 5)

We explore, for the first time, the effect of supernova on higher multiplicity hierarchical systems. In doing so we develop analytical methods to calculate the orbital parameters for systems that remain bound and the runaway velocities for systems that become dissociated after the supernova. We apply these methods to the case of the unusual millisecond pulsar J1903+0327 and confirm that it could have formed from a triple and constrain many of the system's pre-supernova parameters.

CHAPTER 2 On the Effects of Subvirial Initial Conditions and the Birth Temperature of R136

We investigate the effect of different initial virial temperatures, Q, on the dynamics of star clusters. We find that the virial temperature has a strong effect on many aspects of the resulting system, including among others: the fraction of bodies escaping from the system, the depth of the collapse of the system, and the strength of the mass segregation. These differences deem the practice of using "cold" initial conditions no longer a simple choice of convenience. The choice of initial virial temperature must be carefully considered as its impact on the remainder of the simulation can be profound. We discuss the pitfalls and aim to describe the general behavior of the collapse and the resultant system as a function of the virial temperature so that a well reasoned choice of initial virial temperature can be made. We make a correction to the previous theoretical estimate for the minimum radius, R_{min}, of the cluster at the deepest moment of collapse to include a Q dependency, $R_{min} \approx Q + N^{(-1/3)}$, where N is the number of particles.

We use our numerical results to infer more about the initial conditions of the young cluster R136. Based on our analysis, we find that R136 was likely formed with a rather cool, but not cold, initial virial temperature ($Q \approx 0.13$). Using the same analysis method, we examined 15 other young clusters and found the most common initial virial temperature to be between 0.18 and 0.25.

In collaboration with:
Nathan de Vries & Simon Portegies Zwart.

MNRAS 445, 674 (2014)

2.1 Introduction

Subvirial systems are often used as initial conditions in numerical simulations for both physical and practical reasons. Before the phase of gas expulsion, young stellar clusters must be formed subvirial, since the parent molecular cloud was roughly in virial equilibrium and supported by both gas pressure and (turbulent and systematic) velocities. The resultant stellar cluster is no longer supported by gas pressure, but only by the velocities of the stars, and therefore the energy balance must shift to subvirial.

In practice, subvirial conditions are also used to reduce the computational cost of reaching a mass segregated or otherwise relaxed system. This is because with cold initial conditions mass segregation is established on a free-fall time-scale, but virial systems relax and reach mass segregation on a much longer time-scale. Until now the consequence of changing the initial virial temperature has often been considered insignificant and so physical justification is not given.

If for example, an experiment is designed to investigate mergers (Portegies Zwart et al. 1999; Bédorf and Portegies Zwart 2013) (or another physical phenomenon preferentially occurring in mass segregated systems) the evolution of the system between mergers (or until the system is relaxed) is a time-consuming phase with little scientific value. Since the time until the system segregates and violent relaxation is quenched is much shorter for a cold system than for a virial system, using cold initial conditions could, in the past, be a shortcut to the interesting part of the simulation. While these methods may be justified in some cases we are left to wonder if it is in general a valid approximation to the desired physical system. Or for the case of mergers, what effect a free falling interaction, i.e. when using cold initial conditions, may have on impact parameters that a more gentle spiralling interaction, as in the case of warmer initial conditions, may not have.

2.1.1 Violent Relaxation

Lynden-Bell (1967) attempted to explain the "observed light distributions of elliptical galaxies" and in doing so produced the first theory to describe the steady state resulting from a collisionless gravitational collapse. In that pioneering work we find the first use of the term violent relaxation to describe the "violently changing gravitational field of a newly formed galaxy". The fundamental premise of the theory is that the stars in a galactic model may be treated as a large set of independent, non-interacting harmonic oscillators. These oscillators are treated statistically and are expected to find a state of maximum entropy. The weakness of the theory lies in the last statement. During the collapse the system does not have enough time to explore the phase space and so will not generally come to equilibrium in the predicted state.

Since the work of Lynden-Bell (1967) several other attempts have been made to extend, modify, and completely rework the theory of violent relaxation (e.g. Spergel and Hernquist 1992; Nakamura 2000; Treumann and Baumjohann 2013). In spite of these efforts, difficulties remain in constructing a theory which adequately describes the behavior of what may seem at first glance, a simple system (Arad and Lynden-Bell 2005; Arad and Johansson 2005).

2.1.2 Notation

We recall that the virial temperature is $Q \equiv |T/V|$, where T and V are the kinetic and potential energies, respectively, and that a system in virial equilibrium has a Q value of 0.5. Note that just because the energetics of the system is in equilibrium does not imply that the system as a whole is in equilibrium. For example, a system with a Q value of 0.5 can still be out of equilibrium if the system has a uniform density distribution (homogeneous sphere), as used in this paper, this is because the homogeneous sphere is not a solution to the Fokker–Planck equation.

We define the term fraction of virial (FoV) to be the current system's Q value over the Q value of a virialized system, or simply $2Q$. This definition conveniently results in a virialized system having a FoV= 1. We also define the term velocity multiplier, k, as the value the velocity is initially multiplied by to change the system from virial, that is: $k = v/v_{vir}$, v_{vir} is the virial velocity of a particle. So we find that initially

$$\begin{aligned} \text{FoV} = 2Q &= 2\frac{\sum_i \frac{1}{2} m_i (k v_i)^2}{\sum_i V_i} \\ &= k^2 \times 2Q_{vir} = k^2. \end{aligned}$$

2.2 Simulations

2.2.1 AMUSE

Our simulations were run in the AMUSE software environment (Portegies Zwart et al. 2012). AMUSE is a modular simulation platform which provides a set of simulation codes linked together through a PYTHON interface. Different codes can be used on the same initial conditions, allowing for a fast, simple, and clear test of consistency between codes; AMUSE's modular nature makes this easy to do, usually requiring a change to only two lines of code. For example, we tested our simulations with three different N-body integrators, namely: HERMITE (Hut et al. 1995), PHIGRAPE (Harfst et al. 2007), and PH4 (McMillan in preparation). Again the AMUSE framework ensured the changes to the

code were trivial, and by testing with different integrators we obtain an assurance that our results are not code-dependent, since all three codes gave similar results. When using the same set of initial conditions for example, plots of the half-mass radius versus time are nearly indistinguishable, and the number of bound particles at the end of the simulation never differ by more than 55 particles and on average differ by fewer than nine particles (less than 0.37 and 0.06 per cent of the total number of particles respectively). We are now comfortable to assert that the results we present within this work are not the effect of a bug or a strange implementation found in one code, but represent the outcome of physical processes acting on our initial conditions.

All the data presented in this work were produced using PH4. A parallel fourth-order HERMITE integrator PH4 can, and for us does, use GPUs to accelerate the computational work (this is accomplished through the use of the Sapporo library (Gaburov et al. 2009, 2012, Bédorf in preparation)). We find it important to use a direct integrator for these simulations, as opposed to a tree code, because strong interactions play a role in the systems we aim to investigate. In the analysis, we made extensive use of the group finding code hop (Eisenstein and Hut 1998). The runs were performed on the Little Green Machine, a local GPU cluster using NVIDIA GPUs.

2.2.2 Initial Conditions

As this paper is focused on the effect initial conditions have on the resultant physical system we thought it only appropriate to explain exactly how the initial conditions presented within these pages were created. We chose the initial conditions in the following way: a number of particles are distributed in a homogeneous sphere. A homogeneous sphere is used in order to isolate the effects of violent relaxation which can become muddled when using more complex distributions. The mass of the whole system is set to 1.0 N-body mass (Heggie and Mathieu 1986) and either the mass is divided equally amongst all star particles or, in order to study the effects of a more realistic mass function, a Salpeter mass function, having a slope of 2.35 (Salpeter 1955), with a mass range N-body mass equivalence between 0.3 and 100 $M_{\odot}$ is applied or the mass is divided equally amongst all star particles. Each particle is given a velocity drawn randomly from a Gaussian distribution centered at zero, producing an isotropic velocity distribution. If a black hole has been included, it is given a velocity of zero and placed at the center of the cluster. Then the whole system is scaled to be in virial equilibrium. Finally, all unbound particles (particles with an energy > 0) are removed; this is the only time that particles are removed from the system. These particles, along with their position and velocity, are saved to a file. We repeat this procedure with different random initializations always requiring that the final number of objects bound to each system be the number

Table 2.1: Outline of Simulations

No. of runs	No. bound particles	Density	$M_{\rm bh}$ [N-body mass]	Mass function
4×21	15210	Uniform	0	Equal mass
4×21	15210	Uniform	0	Salpeter
4×21	15210	Uniform	0.02	Equal mass
4×21	15210	Uniform	0.02	Salpeter
21	15210	Uniform	0.05	Salpeter
21	15210	Uniform	0.10	Salpeter
21	15210	Plummer	0.02	Salpeter
21	15210	King ($\omega = 6$)	0.02	Salpeter
21	2048	Uniform	0.02	Salpeter
21	4096	Uniform	0.02	Salpeter
21	8192	Uniform	0.02	Salpeter
7	131072	Uniform	0.05	Salpeter

of objects desired ± 5 (never differing by more than 5). Each set of initial conditions is produced four times, each with a different random realization of the particle positions to quantify the effects from initial position on the evolution of the system and to measure the statistical noise.

Before the start of the simulation, the velocities are scaled to whatever Fo Vis being investigated in that run, that is we multiply the velocity by k, the velocity multiplier. Using the same set of initial conditions for an entire set of runs ensures that the differences in each simulation are only due to the difference in velocity. We use 21 values of k (from 0.0 to 2.0 in 0.1 increments) to explore the effect of the FoV on the system. Note that for the supervirial runs particles may be initially unbound, and in many of the subvirial cases particles become unbound after some time, but these particles are never removed from the simulation.

2.3 Results and Discussion

The simulations we ran are described in Table 2.1. Column 1 gives the number of runs performed with each set of initial conditions. Each set of initial conditions (save the last set) are run with 21 different FoV, ranging from 0.0 to 4.0 ($Q = 0.0 - 2.0$); the first four sets are simulated with four different random realizations of the particle distribution in order to reduce statistical error. The FoV is chosen such that the velocity multiplier, k, is equally spaced in 0.1 intervals, i.e. 0.0, 0.1, 0.2,..., 1.9, 2.0. Column 2 of Table 2.1 gives the number of bound particles at the start of each simulation (see Section 2.2.2 for more

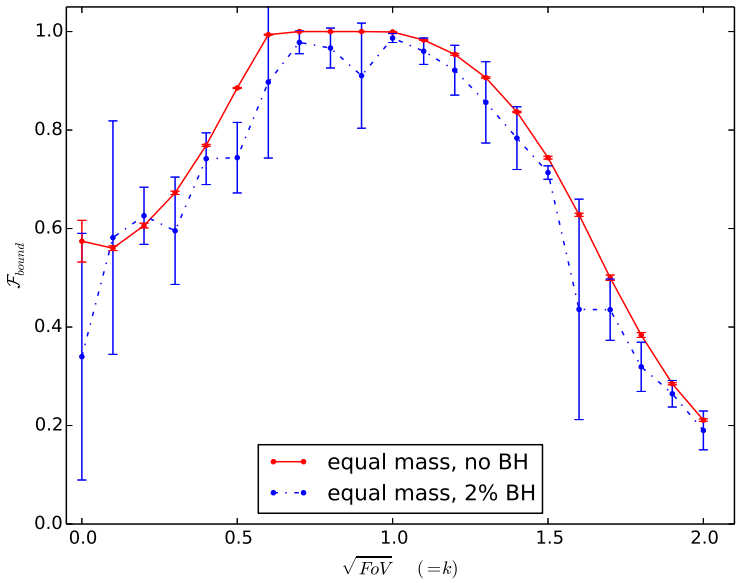
information about our initial conditions). The Salpeter mass function was generated with an N-body mass unit equivalent to 0.3-100 $M_{\odot}$. All simulations are run for a minimum of 10 N-body time units (Heggie and Mathieu 1986) with a data output rate of 50 snapshots per N-body time. We use a softening length, ϵ, such that $\epsilon^2 = 10^{-8}$ for all simulations except for the simulations with 131,072 bound particles where we use an $\epsilon^2 = 10^{-16}$ to be sure we capture the detail of the interactions. In total we ran 490 simulations.

2.3.1 Escape Fraction

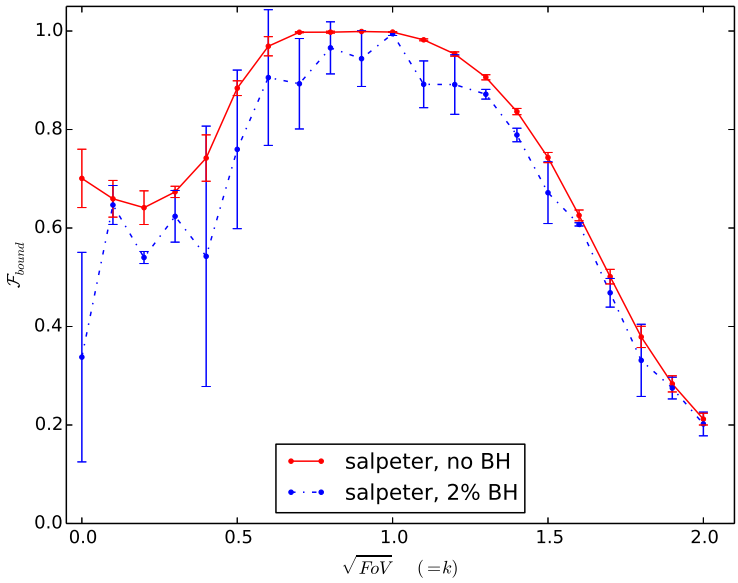
Figure 2.1 is a plot of FoV versus the fraction of objects that remain bound to the system after 10 N-body times. Each data point is an average of at least four runs, and the bars indicate one standard deviation, i.e. a measure of the spread, not the error. Figure 2.1a shows the results of simulations, with equal mass particles (save the black hole) both with and without a black hole. The black hole, when present, contains 2 per cent of the total mass of the system. Figure 2.1b is a plot of the same simulations with the exception that the objects' masses are chosen from a Salpeter mass function; again the cases with and without a black hole are shown and the error bars represent one standard deviation. Though not shown we also ran simulations using a black hole with 5 and 10 per cent of the cluster mass. These simulations showed a similar shape to the curves shown in Figure 2.1 but generally with fewer particles remaining bound as the mass of the black hole was increased.

We note an uptick in retained number of particles with a FoV of 0.0 versus 0.01 for the equal mass systems without a black hole, and a FoV of 0.0 versus 0.04 for systems with a Salpeter mass function without a black hole. To verify that the uptick was not simply an artifact of our four standard realizations, 21 more runs with different random realizations were performed (for a total of 25 realizations) with a FoV $= 0.0$, no black hole, and Salpeter mass function. The results of all 25 realizations are plotted for that point in Figure 2.1.

A possible interpretation for such an uptick is that when the system begins cold (FoV $= 0.0$) there is no radial motion so the particles follow a nearly free-fall trajectory towards the center of mass and so spend the least amount of time in the very high density of the collapse. (The reduced time spent in the highest density of the collapse for cold systems can be seen by comparing the Lagrangian radii in both panels of Figure 2.3.) However, as the FoV increases there is increasing radial velocity leading to an in fall trajectory which is more spiral-like than free-fall-like. With a low but non-zero FoV still leading to a very dense collapse and the particles spending more time near the center of mass at the time of deepest collapse the probability of interactions increases resulting in a higher likelihood for scattering events. When a black hole is added a free-fall path aimed directly at the center is almost a guarantee for a strong scatting



(a) Equal mass particles



(b) Salpeter mass function

Figure 2.1: The fraction of objects remaining bound to the system versus the Fo V. The solid, red line is for simulations run without a black hole, and the dashed, blue line is for simulations with a black hole of 2 per cent of the total mass of the system. The error bars represent one standard deviation.

event, as can be seen in the cases with a black hole (dashed, blue line) and a FoV $= 0.0$.

In the cases with a mass function the fraction of *mass* retained by the system is always greater than or equal to the fraction of particles retained indicating that we keep the more massive particles preferentially and thus tend to lose low-mass particles as expected.

We find in both panels of Figure 2.1 the effect of including a black hole is to, in general, reduce the number of bodies remaining bound to the system, as well as to produce more noise in the measurement. We can understand this by noting that interactions leading to ejections between particles with similar masses only, as is the case when a system does not possess a black hole, produce the loss of bodies as seen in the red lines in Figure 2.1. Introducing a black hole to a system does not change the number of interactions between particles with similar masses and so ejection rates between such particles remain similar to the case without a black hole. However, as the black hole interacts with particles there is the additional case of large mass ratio interactions leading to ejections from the system over the similar mass ejection rate baseline. Thus, the reason the systems without a black hole tend to provide an upper limit on the number of particles remaining bound to the system is due to the addition of a strong scatter in the systems with a black hole while not changing, very much, the probability of smaller mass ratio scattering events. The additional noise found in these measurements of systems with a black hole is the result of the scattering by the black hole being sensitive to the exact nature of the interaction and thus to the random realization of the particles initial positions and their relative velocity.

Proszkow and Adams (2009) and Adams et al. (2006) measured the number of objects that remain bound after 10 Myr for different FoV but include additional effects such as primordial mass segregation, a static gas potential, and gas removal. The difference in the shape of the fraction remaining bound in Proszkow and Adams (2009) is likely due to their static gas potential and analytic gas removal, resulting in a change of the potential energy of the system. It seems this would be similar to a change in the initial FoV, though it is not clear that such a simple substitution would be correct. For instance, if the gas is removed from the system before or even shortly after the collapse (see Figure 2.3 and Section 2.3.2 for a description of what is meant by collapse) the system's evolution will be different than if the gas is removed after the system has relaxed and has reached, or very nearly reached, virial equilibrium. Gritschneder and Lin (2013) show that the amount, time, and even region of mass loss from a collapsing system all have a strong impact on the future evolution of the system, so using the FoV as a proxy for gas removal is very unlikely to by physically correct. Moreover, the nature of gas removal from clusters (e.g. the amount removed, the age of the cluster when it is removed, the dependence

of gas removal on cluster mass, et cetera) is still being investigated (see e.g. Dale et al. 2014; Pelupessy and Portegies Zwart 2012).

2.3.2 Mass Segregation

Bound versus Unbound: A Cautionary Note

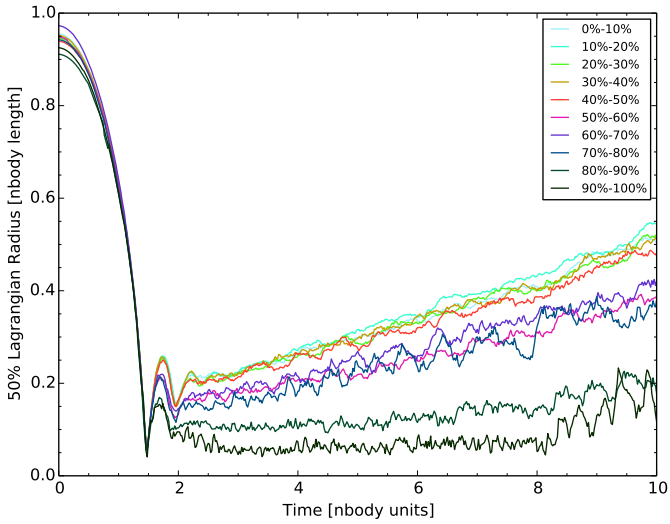
In Figure 2.2, we plot the 50 per cent Lagrangian radii, i.e. the half-mass radius, using data from a simulation with an initial FoV=0.0 and a black hole containing 2 per cent of the total mass. First, the system collapses in approximately a free-fall time to a depth which is often given as $\approx N^{-1/3}$ for N-body simulations. In Sections 2.3.3 and 2.3.4 we discuss the time and depth of the first collapse in more detail. Next, the system rebounds and undergoes a second collapse which is not as deep as the first, similar to a damped oscillator.

Before plotting Figure 2.2 we divide the objects, excluding the black hole, into bins of 10 per cent of the total mass, thus the more massive bins have fewer particles. After the collapse the bins with the most massive objects tend towards smaller radii (bottom of the plot), and conversely bins with the least massive objects can be found with larger half-mass radii. For example, in both panels the bottom line contains the most massive objects which collectively comprise a total of 10 per cent of the system mass, and while the mass represented in each bin is the same it will represent different numbers of objects.

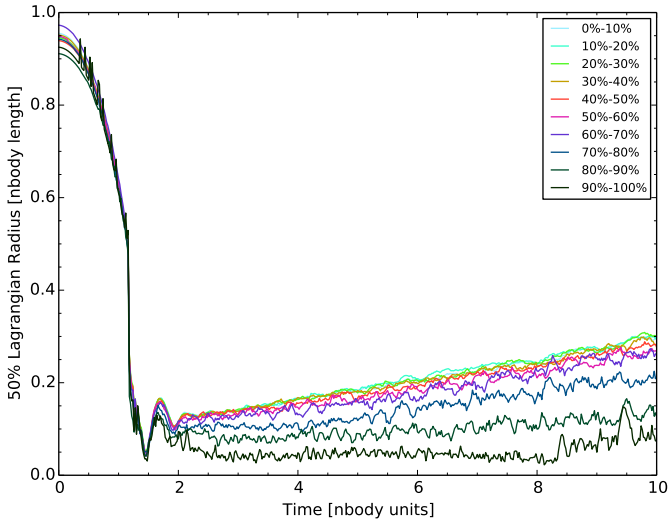
The top panel, Figure 2.2a, shows the half-mass radii of the system when including both bound and unbound particles; whereas the bottom panel, 2.2b, shows the half-mass radius of the system including only the particles bound to the system at each snapshot. The distinction is important particularly for the simulations with low values of the FoV which lose a large fraction of the initial objects. The top panel of Figure 2.2 is in good agreement with the results from McMillan et al. (2012).

When plotting all particles, as compared to only the bound particles, the system appears to have a larger half-mass radius due to the unbound particles tending to be further away from the system and thus increasing the apparent half-mass radius. This is particularly noticeable in the lower mass bins since they are preferentially lost.

However, by taking both bound and unbound particles into account for the analysis the expansion of the cluster appears to be much faster than when only the bound particles are plotted. This would likely lead to a wrong estimate of the evaporation time-scale for the system (presumably other measures of system-wide parameters would be similarly affected). Furthermore, the cluster appears mass segregated even in the lower mass bins, but in fact the selective expulsion of low-mass stars is mimicking mass segregation for these stars. The bottom panel makes clear that the (bound) cluster expands much more slowly and the



(a) Includes all particles (bound and unbound)



(b) Includes only the bound particles

Figure 2.2: The 50 per cent Lagrangian radius (or half-mass radius) for 10 per cent mass bins of a system with a $\mathrm{FoV}{=}0.0$. Each bin contains 10 per cent of the mass and in general the upper lines represent lower mass objects while the lower lines represent higher mass objects. The top panel has all the particles which were originally in the system plotted regardless of whether they remain bound to the system. The bottom panel has only the particles which are bound to the system at that given time. Each different decade of mass is clearly identifiable and more spread out in the top plot, whereas the data are more compressed and mixed in the bottom plot.

mass segregation is only significant for the highest mass bins.

There appears to be more mass segregation when all particles are plotted. For example, in Figure 2.2a the 40 per cent of the mass contained in the least massive particles (i.e. the top four lines in the plot) is not segregated but segregation is noticeable between the most massive 40 per cent and the 50–60 per cent range, and each decade of mass after that. Whereas for Figure 2.2b there is no appreciable segregation in the 0 to 70 per cent range of the mass. The degree of segregation between the various decades of mass is more pronounced when plotting all particles, i.e. the differences between the half-mass radius for the top 10 per cent of the mass (the very dark green line in the plots) and the decade below that (the green line) are larger when plotting all particles (the top panel). These differences would lead to a much different conclusion about the nature of an observed or modeled cluster. Since most objects which become unbound from a system are likely to be long gone at the time of observation, the plots with only bound stars demonstrate a more correct system.

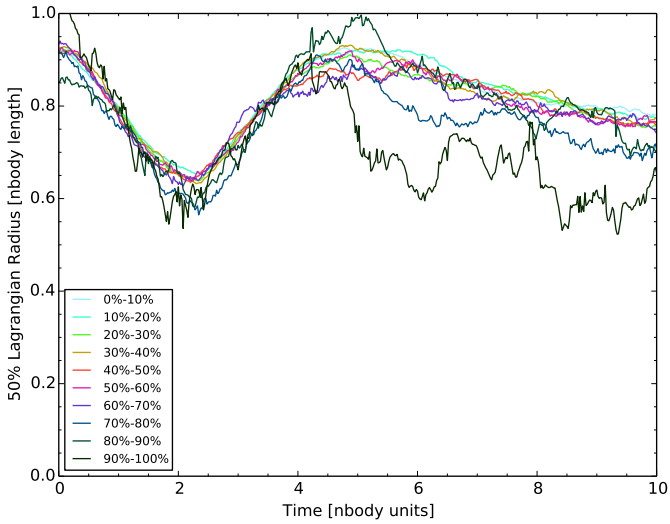
Moreover, without making this distinction the apparent results from the simulation do not reflect the dynamics occurring in the system, since unbound particles which, in time, have almost no impact on the dynamics are still being analyzed as if they were dynamically important. Unless noted otherwise, we shall only use the bound objects at each snapshot for further analysis.

Effect of the Initial FoV on Mass Segregation

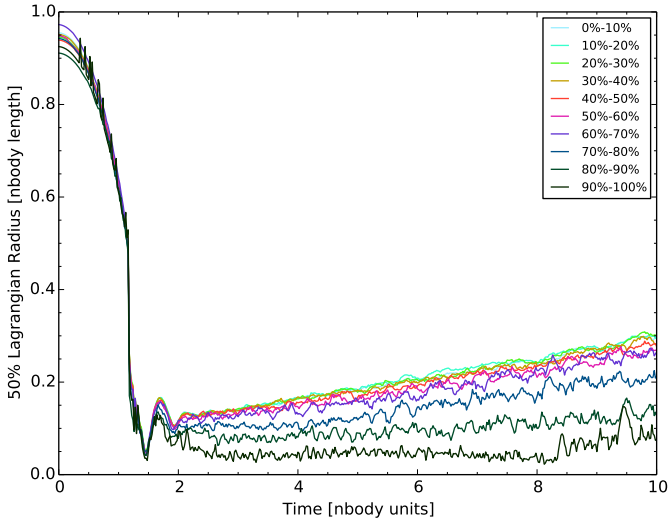
In Figure 2.3, we plot the half-mass radii, just as we did in Figure 2.2b. The upper panel, Figure 2.3a, shows the half-mass radii for a system with an initial FoV of 1.0 (virial), while the system in the lower panel, 2.3b, had an initial FoV of 0.0 (cold). Just as before, the very dark green line represents the most massive particles which comprise 10 per cent of the mass, and the green line above that represents the second set of most massive particles which comprise the next 10 per cent of the mass.

The depth of collapse (i.e. the minimum radius of the system during collapse) is often given as $R_{min} \approx N^{-1/3}$. We find this relationship to only hold for the case where the initial FoV=0.0, see Figure 2.5 and Section 2.3.4 for the better fit we find for different initial FoV. The depth of collapse becomes deeper when the initial FoV is lower (also see Figure 2.5).

Segregation begins during the collapse for both systems and is realized at the deepest collapse. This fast mass segregation has been examined by Allison et al. (2009a) and Allison et al. (2010), and observed in other simulations (e.g. Geller et al. (2013)). In the case of the cold system the bounce occurs at ≈ 1.8 N-body times, whereas for the virial case it requires ≈ 5 N-body times. The virial case takes longer to segregate due to its longer time until collapse, as seen in the insert of Figure 2.4. The increase in density found at the depth of



(a) FoV = 1.0



(b) FoV = 0.0

Figure 2.3: The 50 per cent Lagrangian radius plotted for 10 per cent mass bins. The upper plot shows the half-mass radii for a system with FoV=1.0 (virial) and the lower plot for a system with FoV=0.0 (completely cold).

collapse is what allows the segregation to occur so quickly, and since the deeper the collapse the higher the density so the faster segregation can occur.

We observe, as mentioned above, the collapse is much deeper and shorter in the cold case, Figure 2.3b, than in the virial case, Figure 2.3a, but we find it to have a very different segregation signature. That is, the difference in how the mass is segregated, not so much in the degree of segregation but rather in the degree of segregation between the different mass ranges. This is an example where the attempt to shortcut the cost of evolution using a cold system is clearly seen.

Many of the system properties change as a function of the FoV. Cold initial conditions are sometimes used to more quickly reach a relaxed system (see Figure 2.4 for evidence of faster relaxation for cold systems). In doing so, the implicit assumption is that a relaxed cluster has no memory of the initial FoV but clearly this is not the case; clusters with different initial FoV result in clusters with different relaxed radii and number of bound particles, for example. Some, but not all, of these differences might be resolved by scaling of the initial and final systems, though this would likely come at the expense of faster relaxation.

Moreover, we cannot suggest a way to scale the segregation signature and without scaling it the system will always remain physically distinct. This might however provide an interesting way to diagnose the initial FoV of observed young clusters, though more work would be required in understanding the impact the initial FoV has on the segregation signature (see Section 2.4).

It should be noted that the collapse seen in the system with FoV $= 1$ (Figure 2.3a) is not due to non-equilibrium in the global energetics of the system, but rather due to the spatial and velocity distributions of the particles not being in a relaxed state (i.e. not a solution to the Fokker–Planck equation).

2.3.3 Time-scales

The inset of Figure 2.4 is a plot of the time until the deepest collapse of the system, and the blue circles plot the time between the moment of deepest collapse of the half-mass radius until the end of the bounce for each FoV. The red diamonds mark the time from the beginning of the simulation until the end of the bounce.

We assume that after the bounce the effect of violent relaxation is minimal and the system enters a new regime where two-body relaxation begins to dominate. The time required to reach a virially relaxed state increases as the FoV increases, this should be expected since this time is simply the sum of the time until collapse (inset in Figure 2.4) and the time from collapse until rebound (the blue circles in Figure 2.4) both of which increase with FoV.

The red diamonds in Figure 2.4, provide evidence that warm initial condi-

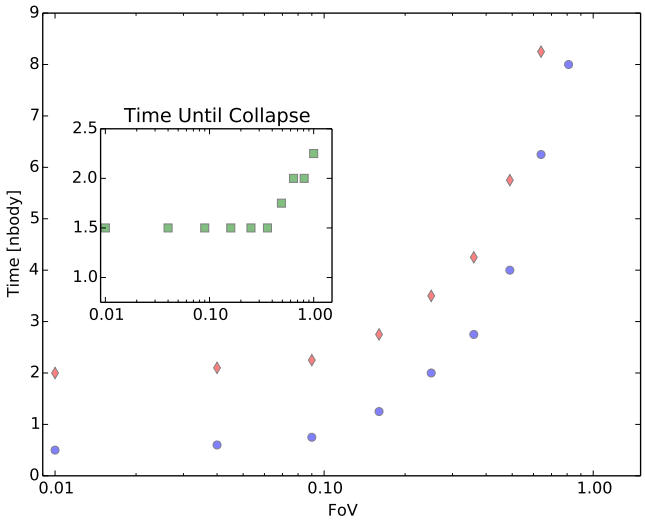


Figure 2.4: The green squares, of the inset plot, mark the time from the beginning of the simulation until collapse. The blue circles indicate the time from the collapse until the end of the bounce. The red diamonds mark the length of time from the beginning of the simulation until the end of the bounce for each FoV; in other words, the minimum time required to simulate in order to reach a mass segregated and relaxed system.

tions in fact do require simulating for more crossing times than cold ones. Note that it takes more than five times longer for the initially virialized case than for the initially cold case to reach the end of the bounce (>10 N-body times compared to 2 N-body times). The end of the bounce for the virial case (FoV $= 1$) is not seen before the 10 N-body times for which we ran these simulations.

The inset in Figure 2.4 shows the time until the system reaches the deepest point of collapse, or R_{min}. We know that the free-fall time-scale, which is the time for collapse of a homologous contraction, is

$$\tau_{\mathrm{FF}} = \sqrt{\frac{3\pi}{32G\rho}}\,. \tag{2.1}$$

Keeping with our use of N-body units, $G = M = 1$, thus $\rho = \frac{3}{4\pi R^3}$ and our equation reduces to

$$\tau_{\mathrm{FF}} = \frac{\pi}{2}\sqrt{\frac{R^3}{2}}. \tag{2.2}$$

At the beginning of the simulations, we measure the most distant particle to be ≈ 1.2 N-body lengths from the center of mass of the system, using that value

for the radius we find a constant value for the time of collapse in our simulations to be

$$\tau_{\texttt{collapse}} \approx 1.46. \tag{2.3}$$

This value is close to what is plotted in the inset of Figure 2.4 for a FoV between 0.0 and 0.36. However, we show it is not valid to assume a free-fall time-scale as the relevant time-scale for collapse in a system with an initial FoV >0.36 ($Q > 0.18$).

2.3.4 Minimum Cluster Radius

In Figure 2.5, we show the half-mass radius at the point of deepest collapse, i.e. the minimum radius during the collapse, versus the FoV. In this figure, we demonstrate the dependence of the depth of the collapse as a function of FoV.

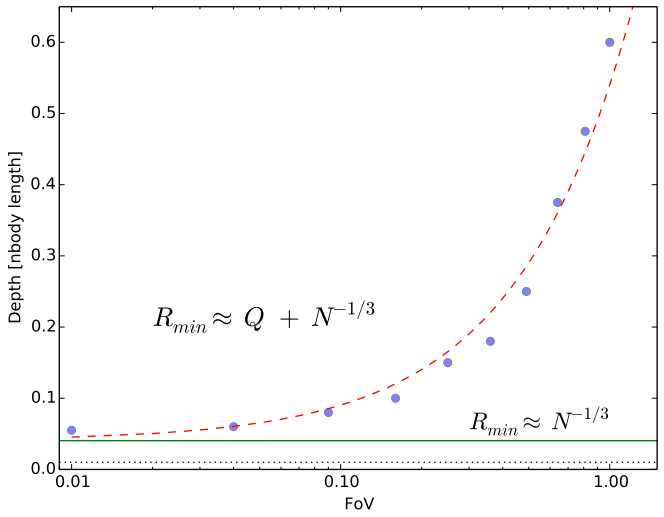


Figure 2.5: The half-mass radius at the point of deepest collapse versus the FoV. The red dashed line is the fit we propose with a Q dependency, the green solid line is the theoretically predicted value, and the black dotted line is the softening length.

The depth of the collapse, R_{min} of collapse, is often given as $\approx N^{-1/3}$ (Aarseth et al. 1988), where N is the number of particles. We recover a value very close to this for the case of a cold collapse finding a difference of only 0.01 N-body lengths. However, as we show in Figure 2.5, and can also be seen in Figure 2.3, the depth of collapse is also dependent on the FoV. In our experiments, we hold N constant and change FoV and we find that as the system becomes more virial the collapse becomes less deep, that is R_{min} becomes larger.

We find that

$$R_{min} \approx \frac{1}{2} \times \mathrm{FoV} + N^{(-1/3)} \tag{2.4}$$

provides a good fit to our data, and is a substantially better approximation for R_{min} in non-cold systems.

Recall from our definition of FoV that $\frac{\mathrm{FoV}}{2}$ is equal to Q. So finally we propose that the minimum radius of collapse is dependent not only on N but also on the virial temperature in the following way:

$$R_{min} \approx Q + N^{(-1/3)}, \tag{2.5}$$

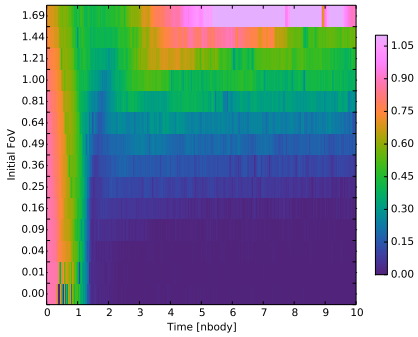
where $Q \equiv |T/V|$ and N is the number of particles being simulated.

2.3.5 Observables

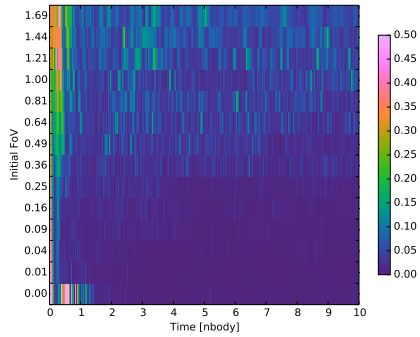
In Figure 2.6 we provide plots of three observable parameters: the core radius, the slope of the density distribution, and the mass segregation ratio. We calculate the core radius by following Casertano and Hut (1985) with a density weighting factor of 2. To measure the slope of the density distribution, we perform a linear least-squares fit of the density and radial distance from the center of the cluster in log–log space. In measuring both the core radius and density distribution we determine the local density using hop (Eisenstein and Hut 1998) with a 7 neighbor particle radius. The mass segregation ratio is calculated using the minimum spanning tree method described in Allison et al. (2009b). We use the 20 most massive particles to construct the "massive" tree and 50 different sets of random particles to construct the "random" trees. The left column of Figure 2.6 shows data from simulations with a Salpeter mass function, with particles initially distributed in a homogeneous sphere, and no black hole, while the right column of Figure 2.6 has a similar set of initial conditions with the addition of a black hole containing 2 per cent of the cluster mass.

We note several regimes in the plots: the first is at early times regardless of the FoV (the far left of the plots) there is a relatively large core radius, flat density distribution, and a small degree of mass segregation. This of course is due to the initial conditions.

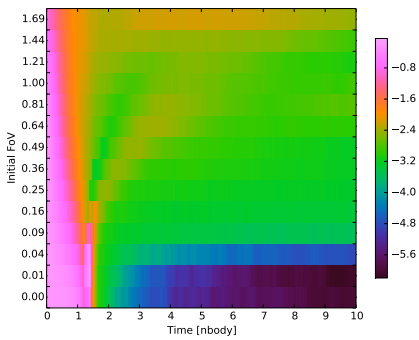
The second regime we note is the lower-right quadrant (small FoV and late times) where the systems have had time to relax. Here we find the smallest core radii, the most extreme density distribution, and the highest degree of mass segregation. By mapping these quantities from an observed young cluster to Figure 2.6 along with other derived properties of a cluster (e.g. minimum age), constraints can be placed on the initial conditions of the system. Additionally, the plots can be used to determine what range of FoV would be ideal to use in the initial conditions for a simulation which aims to reproduce a physical system or investigating a phenomenon in clusters with a particular observable parameter.



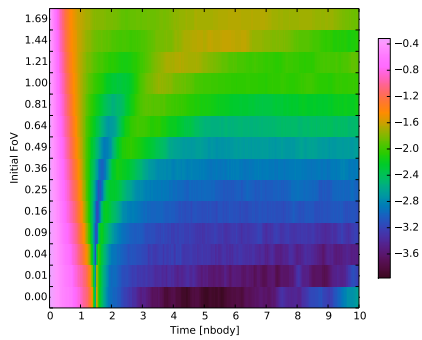
(a) Core Radius



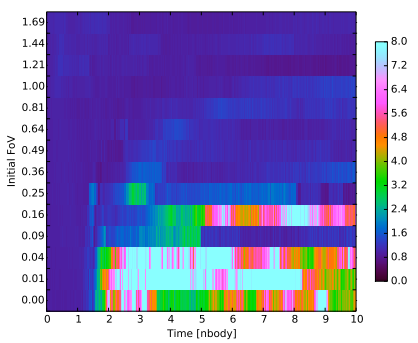
(b) Core Radius



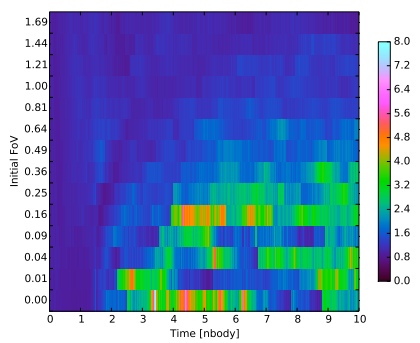
(c) Slope of the Density Distribution



(d) Slope of the Density Distribution



(e) Mass Segregation



(f) Mass Segregation

Figure 2.6: Observable quantities plotted against initial FoV and time. Left (2.6a,2.6c, and 2.6e: system with no a black hole. Right: system with black hole containing 2 per cent of the cluster mass. Top: colors denote the core radius in N-body units. Middle: colors denote density distribution slope. Bottom: colors denote mass segregation ratio.

2.4 Application to an observed cluster: R136

R136 is in the center of NGC 2070 (30 Doradus), which is in the Tarantula Nebula, a young star cluster in the Large Magellanic Cloud (LMC). This region is the subject of many observations including two surveys: The VLT-FLAMES Tarantula Survey (Evans et al. 2011) and the Hubble Tarantula Treasury Project (Sabbi et al. 2013). In the following, we simulate R136 as an isolated cluster in order to constrain the initial FoV and other properties. For this purpose, we performed an additional set of simulations with initial conditions like the second row in Table 2.1: 15,210 bound particles, no black hole, a Salpeter mass function, with particles distributed in a homogeneous sphere. However, we run these simulations for 20 N-body times, producing 1000 snapshots for each simulation.

2.4.1 Observed Parameters

Hunter et al. (1995) found a core radius for R136 of 0.02 pc, a value that was refined to 0.025 ± 0.004 pc by Andersen et al. (2009). The methods used to determine the core radius in Hunter et al. (1995) are disputed for example by Brandl et al. (1996), who found core radii as a function of stellar mass cutoff ranging from ≈ 0.038 to 0.3 pc for high- to low-mass cutoffs, respectively. Other values for the core radius that have been proposed include 0.063 pc (Campbell et al. 1992), 0.1 and 0.15 pc (using different filters, de Marchi et al. 1993), 0.2 pc (Moffat et al. 1985), 0.24 pc (Malumuth and Heap 1994), and 0.33 pc by both Meylan (1993) and Mackey and Gilmore (2003), though Mackey and Gilmore state that due to crowding in their images their value represents an upper limit.

Selman et al. (1999) provide us with a fit to the density profile with a single power law with an exponent of -2.85. There seems to be a much stronger consensus about the value of this observable in the literature and so we will use -2.85 with a spread similar to the range found in other works (section 3.3 in Selman et al. (1999) provides a good overview).

Sabbi et al. (2012) found that R136 likely started forming stars ≈ 2 Myr ago and was still active up to ≈ 1 Myr ago. There are other, older age estimates for the cluster (e.g. Brandl et al. (1996) favor an age of ≈ 3.5 Myr), but since Sabbi et al. (2012) differentiate between R136 and a separate clump to the northeast of R136, which is older and seems to be included in previous age estimates, we choose to use their value. The young age of this cluster is ideal for comparing to our simulations since two-body relaxation has not yet had a strong effect on the system.

Finally, Hénault-Brunet et al. (2012) offer an in-depth analysis of the current virial state of R136. After accounting for the rotation velocity and angle, variable stars, and binaries (see Gieles et al. (2010) for more about the impact

of binaries on the virial state of young clusters) Hénault-Brunet et al. (2012) find that R136 is in virial equilibrium.

2.4.2 From N-body to Physical Units

So far we have shown our results in N-body units (Heggie and Mathieu 1986) however if we are to compare the results to R136 we will need to convert to physical units. When the initial conditions (i.e. the physical scales) are known, this conversion is straightforward. For example, by taking the ratio of the observed virial radius to the measured simulated virial radius, and the ratio of the observed mass of the cluster to the measured mass of the simulated cluster, and setting the gravitational constant to unity a complete converter from N-body to physical units is formed. This converter can then be applied to each snapshot.

However, because we are attempting to constrain the initial conditions we cannot make an assumption about the initial physical scales (i.e. the mass and radius) of the system. Moreover, as we are comparing our results to a known physical system for which we are not certain of the age in crossing times, i.e. N-body time units, we cannot assume that any particular snapshot is the one which represents the observed state. Thus, we are forced to evaluate each snapshot as if it were the one which corresponds to the observed state and thus each snapshot must have its own conversion to physical units.

Our conversion from N-body units to physical units is accomplished in the following way: for every snapshot, we measure the half-mass radius of the bound particles, then, to simulate an observation which is seen in projection, we select all (bound and unbound) particles within a cylinder with a radius equal to the measured half-mass radius. Next, we measure the mass of all of the particles within that cylinder. The final measurement we make is of the virial radius of the system. This measurement must be done carefully since often these systems are out of virial equilibrium, so we use a definition based on the potential energy

$$R_{vir} = -GM^2/(2V),$$

where V is the potential energy.

Still all of these measurements are in N-body units, to convert we use a virial radius of 2.89 pc (Portegies Zwart et al. 2010) and a total cluster mass of $10^5 M_\odot$ (Andersen et al. 2009). We simply take the ratio of the observed virial radius to the simulated virial radius, and the total observed cluster mass to twice the simulated measure of the half-mass. These values along with setting $G = 1$ make a complete unit conversion possible. This procedure is repeated for every snapshot, in this case 1000 snapshots for each value of the initial FoV.

Since each snapshot has a different conversion factor there is counterintuitive behavior in some of the measurements. As said, in many applications a

simple (constant) conversion from N-body time units to physical age is possible, but since our snapshots are produced at fixed intervals of N-body time, and each one has a different conversion factor, the apparent age does not increase linearly, and sometimes may even decrease. For example, if the radius of the cluster expands fast enough the time conversion factor may decrease more quickly than the time in N-body units has increased.

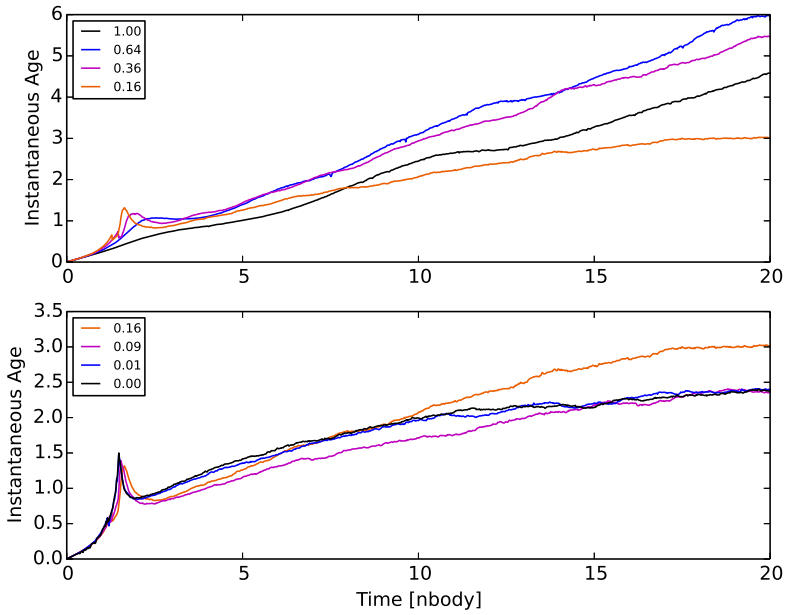


Figure 2.7: The physical age at each snapshot using our converter from N-body units. Each line corresponds to a different initial FoV with 0.16 plot in both panels.

In Figure 2.7, we plot the calculated instantaneous age of each snapshot versus the N-body time using the conversion described above. The bottom panel of Figure 2.7 are plots of the age for initial FoV of 0.0 to 0.16 while in the top panel the plots for 0.16 to 1.21.

The prominent spike in many of the simulations around 1.5-2 N-body times is due to the collapse of the system. During the collapse the simulated half-mass radius is decreasing very rapidly while the simulated mass interior to the projected half-mass radius is remaining constant so the physical time evolved per snapshot becomes very large. Another way to word it is that as the system collapses the number of crossing times per snapshot is increasing.

Again we would like to point out, as we did in Section 2.3.2, the importance of discerning when it is appropriate to use only the bound particles or all

(bound and unbound) particles. To demonstrate this point, we performed the conversion as described above but using the bound and unbound particles to make the measure of the radius (instead of using the particles in the selection cylinder as we did for this analysis). When making this measurement on all the simulated particles we obtained different results, but most strikingly we found that the instantaneous age of each snapshot began to monotonically *decline* after a few N-body times. This is due to the virial radius growing too large too quickly, because of the escaping unbound particles. Clearly such behavior is unphysical, since it would imply that even with an infinitely long simulation the physical age would not increase beyond a certain point, but without such a plot it might not be obvious that something was amiss.

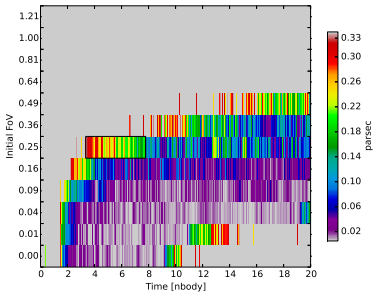
2.4.3 Initial Virial Temperature of R136

We define the central region of R136 for our purposes as the volume interior to its virial radius, or ≈ 2.9 pc (Figure 4 of Hénault-Brunet et al. (2012) presents a nice image of the region with markings for several radii).

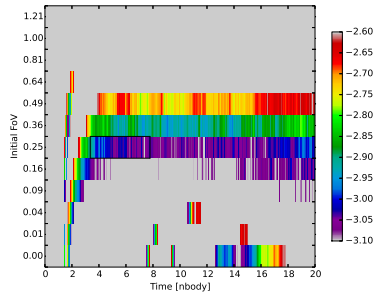
We ran simulations (without a black hole, with a Salpeter mass function, and particles initially distributed in a homogeneous sphere) for 20 N-body times. We show the relevant data in Figure 2.8. The observables shown in Figure 2.8 are not for all bound particles but rather for all particles within a cylinder of radius 2.9 pc from the center of the system; this is done to mimic a projection on to the sky as would be found in the observations. To reduce noise, we plot the average of every two snapshots thereby reducing the number of data points for each initial FoV from 1000 to 500.

In the top-left panel of the figure, we plot the core radius from our simulations with the color coding, in parsecs, representing the ranges outlined above and values not falling between these ranges are plotted in gray. In the top-right panel, we plot the slope of the density distribution. We expect anything within the range of -2.6 to -3.1 to be consistent with the observed value of -2.85 (Harfst et al. 2010). The middle left panel is a plot of the instantaneous dynamical age of the system with values outside of the measured 1 to 2 Myr plotted in gray. While we start each simulation with a set FoV it quickly evolves, we have plotted, in the middle right panel, the FoV as it evolves in time. Since R136 is currently expected to be in virial equilibrium we plot in color the snapshots which have a FoV of 1 ± 0.1. And finally, in the lowest panel, we show the core radius for only the systems which have a valid measurement for all of the above observables (i.e. core radius, slope of the density distribution, dynamical age, and virial temperature).

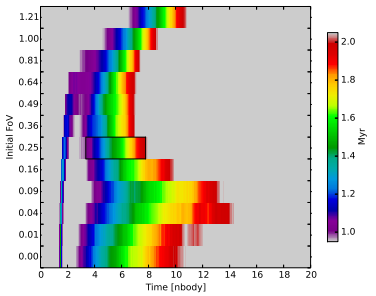
We find that within the observational constraints listed above our simulations limit the initial FoV to a likely value between 0.16 and 0.25, with a most likely value of 0.25. There is also a valid solution at 0.36 but it ranges over



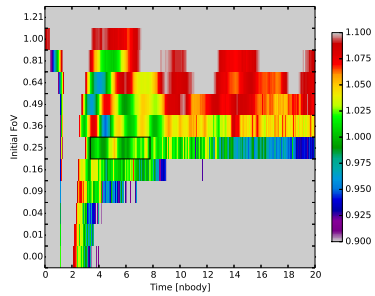
(a) Core Radius



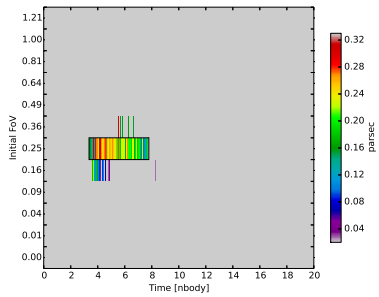
(b) Slope of the Density Distribution



(c) Instantaneous Age



(d) Evolved FoV



(e) Result (core radius)

Figure 2.8: Several measures of simulated systems with only the values matching the observational limits of R136 plotted in color. (a) The core radii within observational limits, (b) the slope of the density distribution within observational limits, (c) the age for each snapshot within observational limits, (d) the FoV at each snapshot, and (e) the core radii for snapshots which satisfy all the observational limits. The regions in gray do not produce an accepted value. See the text for more information on the limits. These systems all began as a homogeneous sphere, with a Salpeter mass function, and without a black hole.

a much shorter time and it is not continuous, for this reason we do not find this solution to be as probable. The continuous solution at 0.16 lasts for nearly 0.2 Myr whereas the solution at 0.25 lasts for ≈ 1 Myr so we consider the 0.25 case to be the most likely.

Using the initial FoV of 0.25, we note that in our simulations the core radius is most likely found around 0.2 pc, ranging from about 0.1 to 0.33. We find very few solutions that allow for the small core radius of the order found in Hunter et al. (1995) or Andersen et al. (2009). The range of the simulated FoV is close to 1.0, with the deviations from unity unlikely to be detectable in observations.

We note that these results are based on isolated systems with some simplifications, such as instantaneous star formation and ignoring primordial binaries. And while R136 is likely to have formed with more complicated initial conditions and is not in isolation, these results provide only a first-order estimate for the initial FoV of R136. Moreover, this method may be useful when applied to other young clusters which could aid in determining their initial virial temperatures. We hope this example case has also demonstrated the significance the initial virial temperature has on the evolution of a system.

2.4.4 Other Young Clusters

Using the same analysis techniques we used for R136 we analyzed 15 other extragalactic young clusters. A list of young clusters within and outside the Local Group can be found in Tables 3 and 4, respectively, of Portegies Zwart et al. (2010). We required each cluster to have a reported core radius as well as an "Age/t_{dyn}" (the last column in the tables) of less than 20. Age/t_{dyn} is the inferred age of the cluster divided by dynamical time-scale, or in other words the number of times the typical star has crossed the system (see Gieles and Portegies Zwart (2011) on the usefulness of this measurement). The clusters which we analyzed are: 3cl-a and a1 in M51; B015D, B040, B257D, B448, and Vdb0 in M31; NGC 1711, NGC 1847, NGC 2004, NGC 2100, NGC 2157, NGC 2164, and NGC 2214 in the LMC; and NGC 330 in the Small Magellanic Cloud.

As these systems are not as well studied as R136 we only used the age and core radius as constraining parameters, but otherwise the analysis remained the same as was performed above for R136. In 11 of the 15 cases the initial FoV can be fitted well by a value of 0.36 or 0.49 ($Q \approx 0.18$ or 0.25). In one case, 3cl-a, the initial FoV is large with a value between 0.64 and 0.81 ($Q \approx 0.32$ or 0.40), this was the only case with a likely initial FoV greater than 0.49. In the remaining three cases — B015D ,B040, and B448 — the initial FoV was lower than the typical value. B015D and B448 were best fitted by an initial FoV by 0.04 and 0.09, whereas B040 was best fitted by 0.16 or 0.25.

We find the most typical value (i.e. the mode) for the best-fitting initial FoV in all of the clusters we tested (including R136) to be 0.36 and 0.49 ($Q \approx 0.18$ and 0.25), collectively these two values fit nearly 70 per cent of the clusters tested. A probability-weighted average of the distribution of the initial FoV for these clusters yields a value of 0.30 ($Q = 0.15$).

There may be observational evidence for clusters forming with a rather low initial FoV as we have found here; for example, André (2002) studied ρ Ophiuchi and found evidence of collapse. Additionally, Walsh et al. (2004) found subsonic motion of star-forming cores in NGC 1333 implying subvirial velocities, and Peretto et al. (2006) found signs of global collapse in two massive cluster-forming clumps, namely NGC 2264-C and NGC 2264-D. Moreover, Proszkow et al. (2009) found that subvirial initial conditions were required in their model in order to explain the kinematic observations of the Orion Nebula Cluster.

2.5 Conclusion

While we suspect that the use of "cold" initial conditions is done too often for computational convenience, and with little consideration to physical reasoning, we do not, and cannot, claim that using any particular subvirial temperature is incorrect or less physically consistent since the distribution of the initial virial temperature is unknown. We simply aim to demonstrate that the choice of virial temperature is important to consider when formulating initial conditions as this choice has a profound impact on evolution of the resulting cluster.

We also stress the importance of performing analysis only on relevant particles in a simulation, in our case usually the bound particles. We show an example of the error that can result by analyzing all particles and not only the bound particles in Figure 2.2. Furthermore, we found that the improper use of unbound particles in the conversion from N-body to physical units lead to unphysical results.

We examined the effect the initial FoV has on the number of particles lost in cases with equal mass particles as well as with a mass function in Figure 2.1. In the same figure, we find that the addition of a black hole to a cluster has the effect of reducing the number of bound particles after 10 N-body times, as compared to the same system without a black hole, since the black hole acts like a strong scatter. Additionally, we note an uptick in the number of bound particles for cold systems. We speculate that this effect is due to the particles initially having no radial motion and so passing through the core on a nearly free-fall trajectory causing them to spend the least amount of time in the very high density core during the collapse. We then discussed how the mass segregation is dependent on the FoV, not only in degree but also in what

we called the mass segregation signature (essentially the difference in degree of mass segregation between different mass ranges).

Next we considered the strong influence the choice of initial FoV has on the time-scales (Figure 2.4) and the radius of a system (Figure 2.5). In doing so, we find that the minimum radius, R_{min}, of a system in violent collapse has a strong dependency on the virial temperature, Q, as well as the number of particles, N. We find that $R_{min} \approx Q + N^{(-1/3)}$. Figure 2.4 also provides an estimate to the extra computational expense to reach a mass segregated cluster in a steady state for different initial FoV.

After plotting observable quantities, i.e. the core radius, the slope of the density function, and the mass segregation ratio as a function of time and initial FoV in Figure 2.6 we discuss the impact of the inclusion of a black hole as the system evolves. We finally compare our simulated system (particles initially distributed in a homogeneous sphere, with a Salpeter mass function, and without a black hole) to the young cluster R136. In doing so, we find that given R136's age estimate, the observed current FoV, as well as the observed slope of the density distribution, and the many observational constraints on the core radius, R136 would most likely have had an initial FoV of 0.25 ($Q \approx 0.13$). We repeated the same analysis on 15 other young clusters for which we found 0.36 and 0.49 ($Q = 0.18$ and ≈ 0.25, respectively) to be the most likely initial FoV in nearly 70 per cent of all 16 young clusters (including R136) and a probability-weighted mean of the distribution of initial FoV to be 0.30 ($Q = 0.15$). While these results are robust, we do note that these values are based on an idealized system.

Finally, we hope that this work has convinced the reader of the importance of the initial virial temperature used in simulations. Whether used as the initial velocities of particles or of merging galaxies, the effect of the virial temperature can be profound and as such should be carefully chosen.

Acknowledgments

It is a pleasure to thank Steve McMillan for helpful conversations and the anonymous referee for the thoughtful comments.

CHAPTER 3 Rapid Mass Segregation in Collapsing Clusters

We introduce a new method to measure and quantify mass segregation which we then use to explore the mechanism driving rapid mass segregation. The method is based on measuring how statistically likely n number of high mass particles are expected to be closer to one another than a random set of n particles drawn from the same system. This method, which we call the nearest neighbor method, is shown to provide similar results for simple star systems, a better measure of mass segregation in complex systems, while providing a significant speedup over the previous, minimum spanning tree, method.

We apply our new method to measure the mass segregation in simulations of cold, collapsing star clusters. Two, dynamical, hypotheses have been put forward to explain the mechanism causing the rapid mass segregation in collapsing clusters; we have designed and implemented an experiment to distinguish between. We find that the rapid mass segregation of star clusters is primarily driven by the very high density of the cluster toward the end of the collapse and is not the result of multiple sub-clusters forming and mass segregating during the collapse.

In collaboration with:
Nathan de Vries & Simon Portegies Zwart.

In Preperation

3.1 Introduction

Mass segregation describes the phenomenon wherein a given system massive astronomical objects are statistically more likely to be found near other massive objects than objects of arbitrary mass. This will be the working definition of mass segregation throughout this paper.

Several mechanisms, e.g. dynamical friction (Chandrasekhar 1943), can account for mass segregation in general, understanding the mass segregation observed specifically in young star clusters, i.e. in the Trapezium of Orion, places a time constraint on the mechanism. Because these clusters are young the mass segregation must happen much faster than expected or the system must have formed in such a way that the most massive stars were born close together, so called premodial mass segregation. Determining the mechanism for such rapid mass segregation could have significant implications for where in a cluster stars form, which additionally could provide an indication on the formation mechanism of massive stars.

Bonnell and Davies (1998) suggested that a dynamical mechanism could not satisfy the time constraint of rapid mass segregation. However, Allison et al. (2009a) found that for clusters which were initially subvirial and initially had substructure dynamical mass segregation can satisfy the time constraint from young clusters. Olczak et al. (2011) and Caputo et al. (2014) showed that even subvirial cluster without initial substructure (distributed in a homogeneous sphere in the latter case) could produce mass segregation on a very short time scale as well, suggesting that the initial virial temperature may be the more relevant metric for rapid mass segregation driven by dynamics.

Allison et al. (2009a) suggested that subvirial collapsing clusters mass segregate more quickly than might be expected due to the dense core formed as a result of the collapse (see Caputo et al. 2014, for a detailed study of the effect of the virial temperature on collapsing clusters). McMillan et al. (2012) claimed that this rapid mass segregation happens not around the time of the "high density bounce", but rather during the entire collapse. Using the simulation data from Caputo et al. (2014) with nearly 500 simulations of collapsing systems we investigate the phenomenon of rapid mass segregation.

3.2 Method

In order to examine the effect of mass segregation on collapsing star cluster we must consider how to measure the degree of mass segregation. Allison et al. (2009b) presented a method for measuring mass segregation by using a minimum spanning tree. The minimum spanning tree (MST) is a method to connect a number of points, or vertices, in a space by the shortest path without any

loops. The MST determines the length of this path. (We used Kruskal's method (Kruskal 1956) when reimplementing their method.) Earlier methods tended to be dependent on models of the density profile or mass function and on the number of mass bins among other parameters (see Gouliermis et al. 2004). Additionally, these methods assumed the mass segregation would be found in and around the cluster's center, the definition of which was not always clear.

3.2.1 Minimum Spanning Tree Method

To determine the mass segregation the n number of most massive particles are selected and the MST length of those particles is found, $\ell_{massive}$. Next, n number of particles are selected at random from the cluster and the MST length for these particles is found, ℓ_{random}. This step of finding the MST length for random sets is repeated some number of times, Allison et al. (2009b) suggest that 50 times is adequate but that hundreds produce smoother trends. They then find the average of the MST length for all of the random sets and determine the ratio of these two lengths:

$$\Lambda_{MST} = \frac{\langle \ell_{random} \rangle}{\ell_{massive}} \pm \frac{\sigma_{random}}{\ell_{massive}}. \tag{3.1}$$

Where σ_{random} is the standard deviation of the measurements of the randomly selected sets. If Λ_{MST} is around 1 it suggests that the separation between the n most massive particles is similar to the separation between the particles in the system in general, i.e. there is no mass segregation. If Λ_{MST} is significantly > 1 it suggest that separation between the n most massive particles is much smaller than the separation between the particles in the system in general, i.e. the system is mass segregated. Finally, if Λ_{MST} is significantly < 1 it suggest that separation between the n most massive particles is much larger than the separation between the particles in the system in general, i.e. inverse mass segregation.

3.2.2 Nearest Neighbor Method

We have developed a new method which we have dubbed the Nearest Neighbor (NN) method. The method is similar to the MST method in that it calculates a length for the n most massive particles and then the length is measured again for some number of randomly selected groups each with n particles as well. The difference is that in place of calculating the minimum spanning tree we calculate the average distance to the nearest neighbor for each set. Other than the distance measurement the remainder of the algorithm is the same, Λ_{NN} is calculated just as it was for Λ_{MST}:

$$\Lambda_{NN} = \frac{\langle \ell_{random} \rangle}{\ell_{massive}} \pm \frac{\sigma_{random}}{\ell_{massive}}, \tag{3.2}$$

and the interpretation of the results is the same as well.

As we will show, the advantages of the NN method over the MST method include better detection of mass segregation in clusters with complex structure as well as a dramatic reduction in computation time.

3.3 Comparing Results

3.3.1 Measurements of the Mass Segregation

Simple Mass Distribution

In order to compare the MST method to the NN method we have constructed an artificial data set of a star cluster; the cluster is constructed such that there are 16K (i.e. 2^{14}) particles arranged in a plummer sphere with a Salpeter mass function (Salpeter 1955), with masses from 1 to 50 $M_{\odot}$, which are assigned randomly to the particles in the cluster. The inner 160 particles ($\approx$ 1 per cent of the cluster) are then reassigned masses based on a Salpeter mass function with masses from 50 to 100 $M_{\odot}$. This produces a cluster in which the 160 most massive particles are mass segregated, in a core, from the remainder of the cluster, however there should be no significant mass segregation outside of the core.

In Figure 3.1 we plot the mass segregation ratio for the artificial cluster described above out to the 200 most massive particles. The red line is produced by the NN method (this paper), whereas the blue line is produced by the MST method, in both cases 50 random sets were used in order to calculate $\langle \ell_{random} \rangle$. The two methods give nearly identical results. The region shaded in red is the $\pm 1\sigma$ level of error from the NN method, we chose not to show the error from the MST method because the two of them were so similar that showing both resulted in confusion in the plot. The horizontal, solid green line indicated a mass segregation ratio of 1, i.e. no mass segregation, and the vertical, dotted green line is placed at 160 particles, the number of mass segregated particles (by construction).

Both methods indicate the presence of mass segregation of the 160 most massive particles.

Using the NN method we plot, in Figure 3.2, the mass segregation ratio for the artificial data set described above; each line represents the data from using a different number of random sets, from 1 to 100, to calculate $\langle \ell_{random} \rangle$. We plot the data for sets from 1 to 100, though we only show every other value in the legend so as to make it (nearly) readable. Using the NN method we are able to do this out to 512 particles due to its increased speed, however after several months the MST version of the same plot is not finished running.

Figure 3.2 demonstrates how using more random sets reduces the noise in

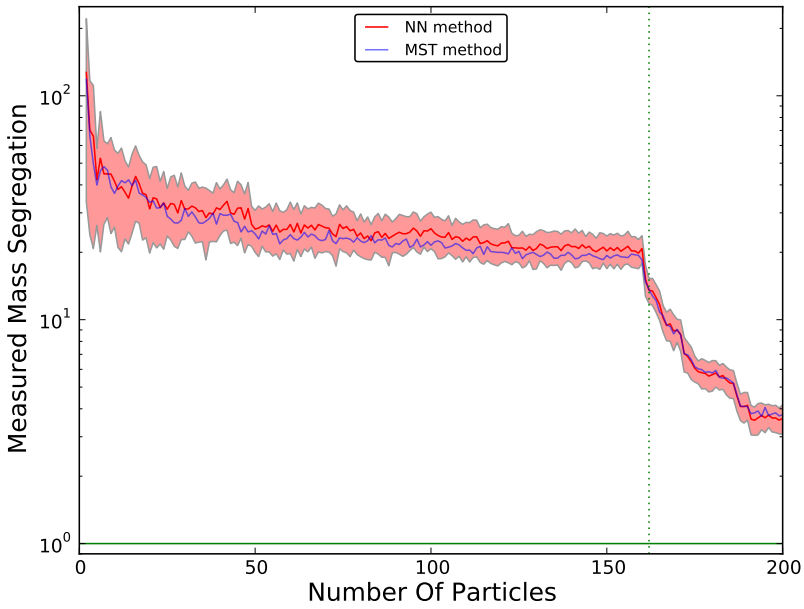


Figure 3.1: Results from the NN (red line) and MST (blue line) methods on an artificial data set in which the 160 most massive particles are mass segregated in the center of the system, see text for more details. The red shaded area represents the ± 1 σ error level of the NN method. The horizontal, solid green line indicates a mass segregation ratio of 1, i.e. no mass segregation; the vertical, dotted green line indicates 160 particles, the number of particles which are mass segregated in the data set.

the measurement, of course this comes at the expense of more computing time needed. Also note how the values for the mass segregation drop off after the 160^{th} particle, after which there is no mass segregation. The value decays to around 2 for 512. This decay, instead of a fast drop, is the result of the first 160 most massive particles having an effect on the mass segregation ratio of the remainder of the particles; for example, when calculating the mass segregation ratio for the first 161^{st} particles the result is dominated by the first 160, mass segregated, particles, and at the 320^{th} particle the first half of the particles are mass segregated so the mass segregation ratio will show values greater than 1 even though there is no mass segregation at that value. For this reason it is important that these methods be used with a regular interval of particles, calculating the mass segregation ratio out to only one particle value, i.e. only calculating the mass segregation ratio for the first X-number of particles while not doing so for the particles before it may result in results which cannot be interperted correctly.

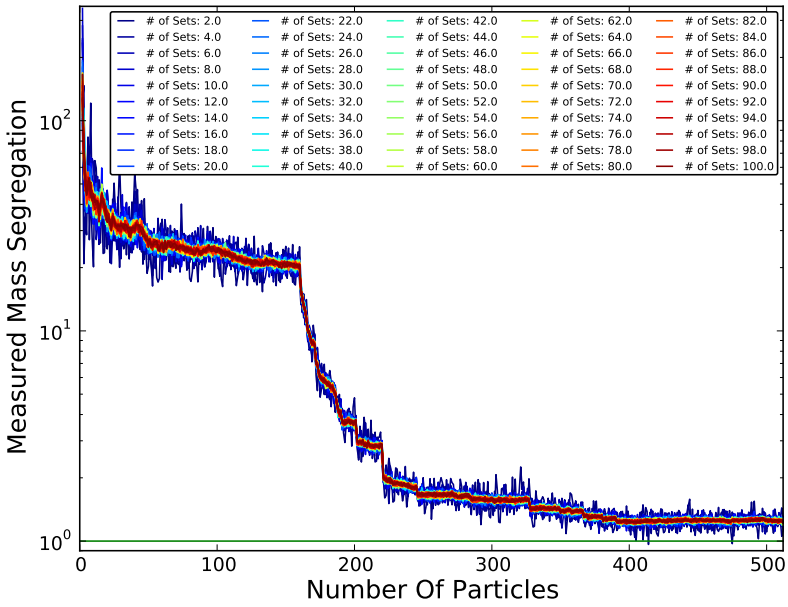


Figure 3.2: The mass segregation ratio, using the NN method, out to 512 particles for the same data as in Figure 3.1. Calculated with different number of random sets, up to 100, as indicated in the legend. For the sake of readability only the even number of sets are labeled in the legend, however all number of sets, from 1 to 100 are plotted.

What is the benefit then of this new method if the results are essentially the same?

Complex Mass Distribution

We produced another artificial system to test the difference between the NN and MST methods. For this test case we created a system just as we did above with all of the most massive particles located in the center, but this time with the nine separate cluster each with $^1/_9{}^{th}$ the number of particles (both massive and non-massive). We then place all nine identical, mass segregated systems into a single volume. Of the nine systems one is placed in the center and the remaining eight are placed equally around a sphere such that the radius of each system does not overlap with the radius of any other systems.

Each subsystem has 1,820 particles with 18 massive particles in their center, resulting in a total of 16,380 particles and 162 massive particles. Figure 3.3 is a plot of the mass segregation measure of this system out to the 200 most massive particles using 50 random sets to calculate ℓ_{random}. The solid red line

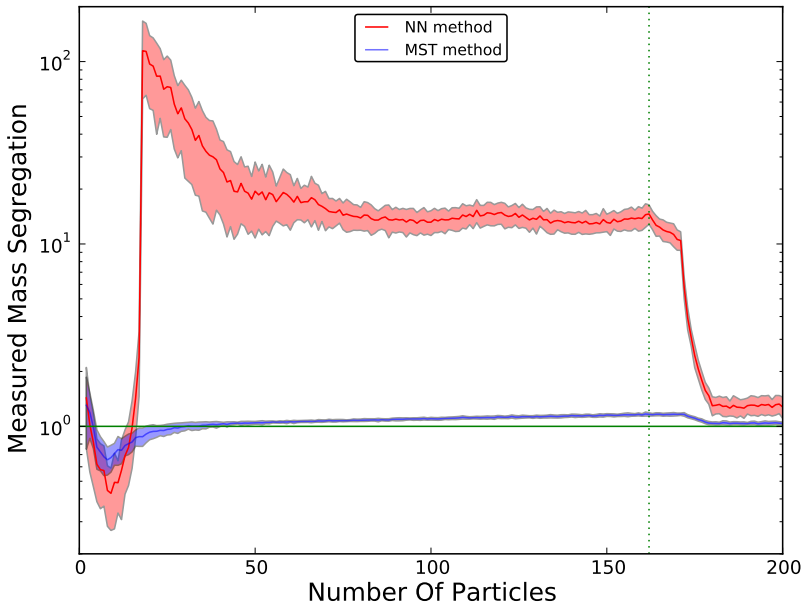


Figure 3.3: Results from the NN (red line) and MST (blue line) methods on an artificial data set in which the 162 most massive particles are mass segregated in the center of nine sub-clusters arranged in a non-overlapping way, see text for more details. The red and blue shaded area represents the ± 1 σ error level of the NN and MST methods respectively. The horizontal, solid green line indicates a mass segregation ratio of 1, i.e. no mass segregation; the vertical, dotted green line indicates 162 particles, the number of particles which are mass segregated in the data set.

is the measurement from the NN method, with a $\pm 1\sigma$ error shown by the red shaded area; the blue line is the measurement from the MST method, a $\pm 1\sigma$ error is shown by the blue shaded area. The solid, horizontal green line is plotted at 1.0, i.e. no measured mass segregation, and the vertical dashed line marks the 162 most massive particle, i.e. the end of the designed mass segregation.

The system is mass segregated, but in small sub-clusters. For the first nine most massive particles (the single most massive particle from each of the sub-clusters) both the NN and MST method show inverted mass segregation, the most massive particles are more separated from each other than randomly selected particles are seperated. This is because the length of the NN and length of the MST for the nine most massive particles is measuring the separation between the sub-clusters, but when measuring the respective length for the random sets of particles if any two particles are selected from the same sub-clump then the length for the random set will be significantly shorter than the length

for the most massive particles. However, after the ninth most massive particles the two methods diverge in their respective measurement of the mass segregation. The MST method remains, and always will remain, dominated by the separation between the sub-clusters, whereas with the NN method the measured length for the most massive particles is a measure of the distance between those particles and not the sub-clusters.

The MST method is unable to identify mass segregated sub-clusters that are spread over the total system volume, but the NN method can make good measurements of simple systems while also adjusting to more complex systems. While not fool-proof, there are cases that both the NN and MST methods would be poor at accurately measuring mass segregation, we have shown that the NN method is more graceful at adapting to different mass distributions.

More importantly, we have shown that the NN method is able to measure mass segregation of sub-clusters, a required step if we are to distinguish between the two proposed mechanisms of dynamical rapid mass segregation.

But wait there is more, the NN method is also much faster.

3.3.2 Speed

The MST method was a considerable improvement over previous methods which either did not quantify the degree of mass segregation and/or were model dependent. However, to quantify mass segregation using this method when provided with an unknown system one must preform the method on a regular interval for every number of most massive particles up to the final degree of mass segregation one desires to test. That is, if one wished to know if a given a system of 10^4 particles was 10 per cent mass segregated the method would have to preformed 1000 times; constructing the MST for the 2 most massive particles, then 3, 4, . . . , 1000 particles, each time constructing 50 other MSTs for the random sets.

The MST method has a runtime complexity of $O(E\log E)$ where E is the number of edges, i.e. the number of connections between points. Since we assume all points can connect to all other points we have a complete graph which has $n(n-1)/2$ edges. So to highest order the complexity is $O(n^2\log(n^2))$. However, before we calculate the MST length we must also calculate the length of all the edges which has a complexity of $O(n^2)$; so in total our expected runtime complexity is $O(n^2 + n^2\log(n^2))$.

The Nearest Neighbor Method requires the calculation of all of the distances between all particles, the exact same calculation as determining the length of all the edges, which has a runtime complexity of $O(n^2)$[1]. This means the

[1]This is for the naive implementation, using a more sophisticated approach, such as a k-d tree has a complexity of $O(\log(n)[n+1])$.

Nearest Neighbor method should be roughly $2\log(n)+1$ times faster than the MST method for each iteration.

In the case we want to know the the mass segregation out to 10 per cent of a cluster with 10^4 particles the NN method would be faster by a factor of $\sum_{2}^{1000} 2\log(n)+1$, which is a whopping 6,100 times faster than the MST method. In Figure 3.4 we plot the number of particles, n, used for the NN and MST method versus the time it takes for each iteration, the solid lines, and the cumulative time, the dashed lines. The red lines are for the NN method and the blue lines for the MST method. We show that for $n > 11$ particles the total cumulative time for the NN method is shorter than the time needed for a *single step* with the MST method. Moreover, the cumulative time using the MST method for $n = 200$ particles is a factor 1000 times longer than the NN method. The savings in runtime we obtain from the NN method over the MST method is so large it allows us to explore portions of the parameter space that were not avalible before; e.g. in trying to run the simulations to produce Figure 3.2 the NN method took ≈ 8 hours (iterating from 2 to 512 particles and from 1 to 100 random sets), at the time of writing the MST method had been running for *3 months* and at that point was only to particle 344.

However, Figure 3.2 is a very artificial examination of the method rather than a useful science tool. Where this speedup becomes needed is to do science when the number of particles in a system is very large. Allison et al. (2009b) tested their method on systems on 1000-body clusters, measuring the mass segregation ratio of up to 10 per cent of the cluster size (i.e. up to 100 particles). The MST method works well enough at those numbers, but simulations are becoming ever larger (even simulations with $N = 10^{10}$ are becoming possible see e.g. Bédorf et al. (2014), though Portegies Zwart and Boekholt (2014) provides an interesting counter-example). Testing mass segregation for up to 10 per cent of systems with $N = 10^4$ become very tedious with the MST method and simply unobtainable for $N = 10^5$.

We find that for the NN method using 50 random sets the cumulative time, in seconds, grows as power law with the form $\approx 0.03n^{1.23}$ (see the red dotted line in Figure 3.4); whereas, the cumulative time for the MST method, again using 50 random sets, grows as $\approx 0.001n^{3.1}$ (see the blue dotted line in Figure 3.4). Assuming these holds for very large values it implies that calculating the mass segregation for 10 per cent of a 10^6-body system, that is calculating the mass segregation out to 10^5 particles, would take about 12 hours with our NN method, and much longer than a career time for the MST method. The NN method makes exploring mass segregation much more practical for nearly any size system, and obtainable even for large systems.

The NN method will always have a speedup over the MST method which is not something that can be compensated for by improving the MST algrithum

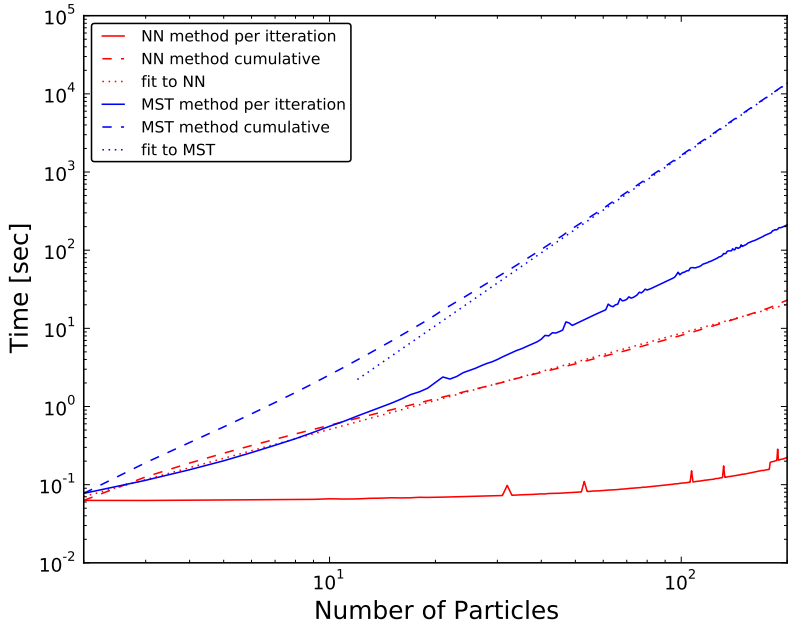


Figure 3.4: The solid lines show the per iteration time in seconds, the dashed lines show the cumulative time, and the dotted lines show the fit to the cumulative time. The red lines are for the NN method (this paper) and the blue lines are for the MST method. The fit to the NN method (red, dotted line) is of the form $0.03\ n^{1.23}$ and is in good agreement with the cumulative time for the NN method. The fit to the MST method (blue, dotted line) is of the form $0.001\ n^{3.1}$ and is in good agreement with the cumulative time for the MST method after $n \approx 30$. We used 50 sets of data to calculate $\langle \ell_{random} \rangle$.

or moving the two methods to other archatectures, e.g. graphics processing units, because the NN method is a required part of the MST method. While preforming the MST method one must find all of the

3.4 Results and Discussion

3.4.1 Simulation Methods

We have simulated systems with 15,210 particles initially spatially distributed in a homogeneous sphere. The masses of the particles are drawn from a Salpeter mass function in N-body units with a physical equivalent of 0.3 to 100 $M_{\odot}$. The systems examined below, unless otherwise noted, are produced cold, i.e. with a virial fraction of 0.0. They are then simulated for 10 N-body times in the AMUSE environment (Pelupessy et al. 2013) using the fourth-order Hermite

code ph4 (McMillan in prep.). For more details about the simulation setup see Section 2 in Caputo et al. (2014).

In analyzing the mass segregation of the simulations we primarily make use of the NN method outlined above. To calculate the density of the cluster core we use the code hop (Eisenstein and Hut 1998) with 50 nearest neighbors.

3.4.2 Mass Segregation

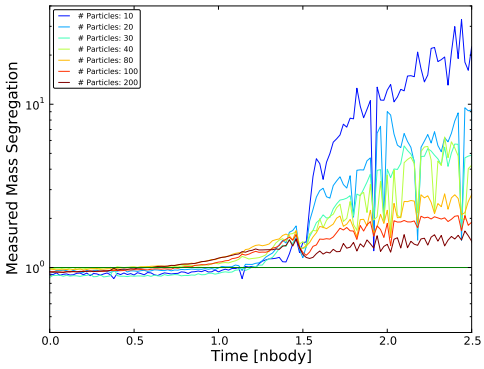
McMillan et al. (2012) suggested that rapid mass segregation happens as a result of a collapsing system forming sub-cluster which due to their small size mass segregate on their, fast, dynamical timescale; whereas, Allison et al. (2009a) had proposed rapid mass segregations is due to the short-lived, but very dense state that happens as the cluster's collapse reaches a maximum. In order to distinguish between these two scenarios, or uncover a different mechanism, we have designed an experiment to disentangle these cases.

The experiment works in the following way: first, we run a simulation of a collapsing cluster and plot the mass segregation ratio as a function of time. Second, we take a snapshots from that simulation at 0.9, 1.25, 1.5, 1.75, and 2.1 N-body time units (or Henon time units Heggie and Mathieu 1986) and randomly swap the masses (it is important to note that we do not produce new or different masses, we simply rearrange the masses). Finally, we continue running the simulations from that point with the swapped masses, and when each one finishes we again measure the mass segregation ratio as a function of time for the new simulation.

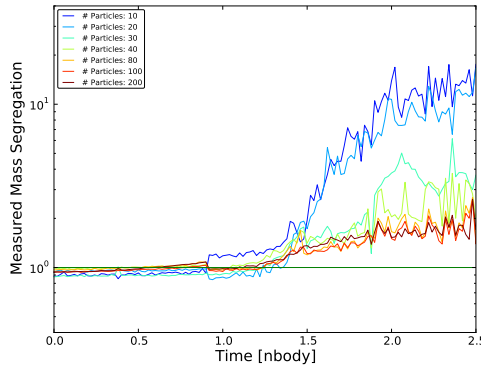
By swapping the masses we are able to remove all of the effect of dynamical mass segregation up to that point and determine what amount of dynamical mass segregation is effecting the cluster after that point. We have plotted the results of this experiment in Figure 3.5.

In Figure 3.5a we plot the "natural" evolution of the cluster, with no mass swapping going on. The horizontal green line, which is common to all six subfigures, is plot at a mass segregation ratio of 1, which is exactly non-segregated. The other lines mark the mass segregation ratio for different number of particles, n, from 3 to 193 particles in steps of 10, as shown in the legend.

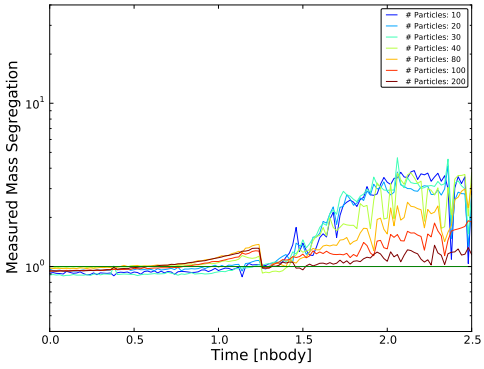
We note that the mass segregation is highest for the fewest number of particles; this is expected since when we measure the mass segregation for 3 particles it is the the 3 most massive particles and for 13 it is the 13 most massive, so it follows that the most massive particles would be the most mass segregated. Caputo et al. (2014) examined these type of collapsing clusters in detail and found that at for an initially cold system, such as in this case, the deepest moment of collapse, the moment with the highest density, happens at 1.46 N-body times, which is visible with a local peak in the mass segregation at the same time in Figure 3.5. Also note the gradual rise in the mass segregation



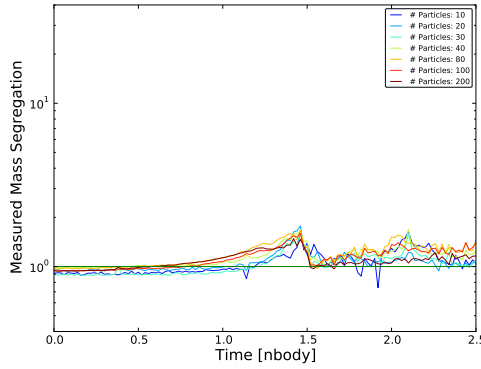
(a) No masses switched.



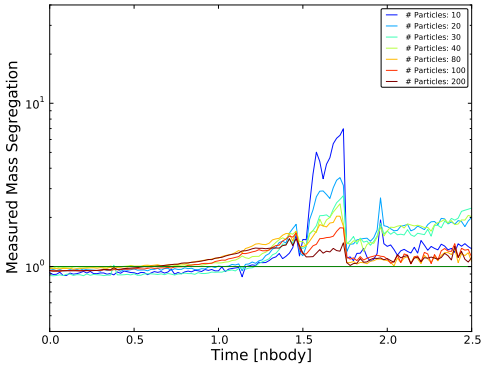
(b) Masses randomly switched at 0.9 N-body times.



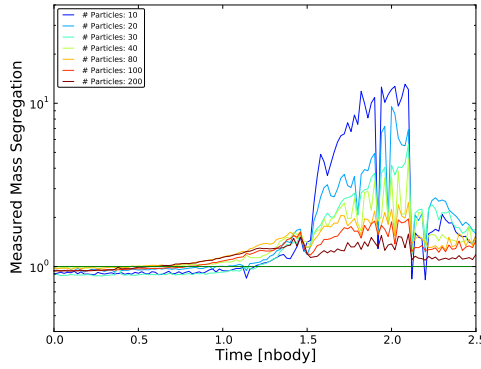
(c) Masses randomly switched at 1.25 N-body times.



(d) Masses randomly switched at 1.5 N-body times.



(e) Masses randomly switched at 1.75 N-body times.



(f) Masses randomly switched at 2.1 N-body times.

Figure 3.5: Mass segregation as a function of time for different number of particles as show in the legend. (a) shows the evolution of the mass segregation as it would normally occur, i.e. without switching mass. (b)–(f) show the evolution of the mass segregation with the masses being randomly switch at 0.9, 1.25, 1.5, 1.75, and 2.1 N-body times, respectively.

starting around 0.6 N-body times for most particle sets. This rise maybe the result of sub-clusters forming and then mass segregating or it maybe the result of an increase in density as the density of the whole cluster increases. Finally, we note that with the exception of the set of three particles the none of the other sets even rise to a mass segregation ratio of two before or during the collapse.

Figures 3.5b–3.5f show the simulations where we have randomly swapped the masses at different times: 0.9, 1.25, 1.5, 1.75, and 2.10 N-body times respectively. In Figure 3.5d we swap the masses just as the cluster is at the deepest part of its collapse; and the other plots are spaced at 0.25 and 0.6 N-body times before and after that time. The swap can be seen in each plot by the sudden drop in the mass segregation ratio at the designated time.

Peculiarly the mass swap shown in Figure 3.5b actually produces an increase in the mass segregation of the three most massive particles. While this is not the intended effect of the swapping the masses, it is a natural outcome when randomly reassigning the masses to sometime put the more massive particles close together; this can be seen as similar to primordial mass segregation (the effects of which we do not explore here).

We observe the general trend that the when the mass is swapped before the deepest moment of the collapse, 1.46 N-body times, after the collapse the mass is always highly segregated compared to when the mass is swapped at or after the collapse which leads to no or at a minimum much reduced mass segregation. This leads us to conclude that the whatever the mechanism is that is driving the future mass segregation it is happening before or at the moment of deepest collapse, i.e. 1.46 N-body time.

In order to distinguish between the two mechanisms suggested above we must carefully examine Figures 3.5b and 3.5c. In Figure 3.5b we are just able to see the steady rising of the mass segregation that we mentioned above started around 0.6 N-body times, then we swap the masses and the segregation ratio gets reset to unity. It then starts to slowly rise again with most of the particle sets reaching the same degree of mass segregation at the local maxima around 1.5 N-body times, though decidedly without the strong drop off following that peak as seen in Figure 3.5a.

Figure 3.5c again shows the rise from around 0.6 N-body times, and since the simulation runs longer without the mass being swapped it reaches a higher level of segregation before it is rushed back to unity with the masses being swapped at 1.25 N-body times. Just a before the segregation ratio rises again, but the particle sets do not tend to reach the same degree of mass segregation as before.

While there are minor differences between the mass segregation in these simulations up to the collapse, they are more similar than not after another N-body time, particularly when compared to the other cases (3.5d–3.5f). The fact that the systems show such similarities after we had removed the effect of early

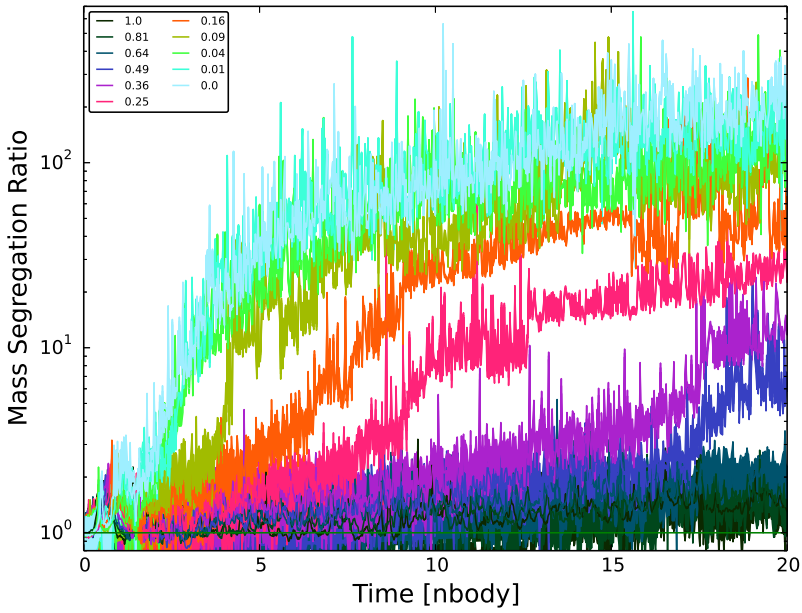


Figure 3.6: The mass segregation ratio as a function of time for several FoVs as indicated in the legend.

segregation (possibly from sub-clusters segregating) suggest that the dominate mechanism leading to this rapid mass segregation is due to the short duration of very high density at the moment of deepest collapse.

3.4.3 Effect of the Initial FoV on Mass Segregation

Caputo et al. (2014) defined FoV to be $2Q$ where Q is the more traditionally defined virial ratio, $Q \equiv |T/V|$ where T and V are the kinetic and potential energies, respectively. For example, since a system in virial equilibrium has a Q value of 0.5, its FoV would be 1.0. Caputo et al. (2014) showed that many cluster parameters are directly impacted, and in some cases even dominantly controlled, by the initial FoV. In Figure 3.6 we show the significance on the initial FoV on the evolution of the mass segregation of a cluster.

Figure 3.6 is a plot of time versus the mass segregation ratio for initial FoVs ranging from 0.0 to 1.0. Lower initial FoVs, initially colder systems, are toward the left of the plot because they seem to segregate more quickly than initially warmer systems. Caputo et al. (2014) found that the most likely initial FoV for a cluster was between 0.36 and 0.49, which corresponds to the purple and blue curves in the plot, and that R136 most likely formed with an initial FoV

of 0.25 which corresponds to the pink curve.

The effect of increasing initial FoV seems to be two fold: first, the time at which the mass begins to segregate is delayed with an increase in FoV, and second, the degree of mass segregation tends to decrease as FoV increases. The second of these effects are explained by observations in Caputo et al. (2014). We note that the depth of the collapse is a function of FoV, namely $R_{min} \approx Q + N^{-1/3}$ where R_{min} is the minimum radius reached during the collapse, Q is as defined above FoV$/2$, and N is the number of particles, which for these simulations is constant. That we find a correlation between a deeper collapse, i.e. smaller FoV, and the more mass segregated the system becomes seems natural.

3.5 Conclusion

We have introduced a new method to measure and quantify mass segregation. This method is based on determining the ratio of the average nearest neighbor distance of the most massive particles with respect to the average the nearest neighbor distance of several sets of randomly chosen particles. This method is very similar in principle and results to the MST method developed by Allison et al. (2009b), however we show that this new method is dramatically faster, providing an ≈1000 times speedup over the MST method for 200 particles. With such a speedup we are able to do science that was unaccessible using the previous method, such as measuring the mass segregation ratio of 10 per cent of simulations with $10^4 - 10^6$ particles. We estimate that our new method would require nearly 12 hours to measure the mass segregation, out to 10 per cent, of a 10^6 particle system, the old method would require more than a career's worth of time (using current hardware, not hardware from 20 years from now).

We then applied this method to simulations of a collapsing cluster to better understand the mechanism which drives rapid mass segregation. We perform an experiment to disentangle whether the rapid mass segregation is a result of sub-clusters mass segregating or the result of the very high density near the deepest part of the collapse. The experimental technique was to randomly swap the masses of particles at and near the critical moment of deepest collapse, thus allowing us to nullify any earlier mass segregation and so to isolate the degree of mass segregation that could be produced from that point forward.

The results are definitively that something prior to or at the collapse is required to drive the rapid mass segregation. By changing the time before the deepest part of the collapse we are able to show that while the sub-cluster mass segregation mechanism may play a role, the dominate drive of the rapid mass segregation is environment when the cluster is nearly at the deepest part of the collapse, likely the very high density.

CHAPTER 4 On Estimating the Total Number of Intermediate Mass Black Holes

Black holes have been detected with masses less than 10^2 and greater than 10^6 $M_\odot$, but black holes with masses in the intermediate range are conspicuously absent. However, recent estimates of the mass of HLX-1, currently the strongest intermediate mass black hole (IMBH) candidate, suggest an approximate mass of 10^4 $M_\odot$, and recent estimates of the mass of M82 X-1 suggest a mass of 4×10^2, placing them within the missing black hole range. This raises the question of whether these are unique objects or if many more of these objects should be expected. In this letter, based on stellar evolution simulations and reasonable assumptions, we estimate the number of HLX-1 like IMBHs expected within the distance of 100 Mpc to be within an order of $\approx 10^6$, or $\approx 10^2$ IMBHs within a galaxy, and about two orders of magnitude more when considering less massive IMBHs using M82 X-1 as a prototype.

In the process of estimating this value we determine the form of the mass function within the sphere of influence of a newly formed IMBH to be a power law with a slope of -1.83. Furthermore, we find we are only able to fit both the period and luminosity of HLX-1 with a stellar companion with a mass between $\approx 10 - 11$ $M_\odot$, a result which is fairly robust to the mass of the IMBH between 10^3 and 10^5 $M_\odot$.

In collaboration with:
Nathan de Vries, Alessandro Patruno & Simon Portegies Zwart.

Submitted to MNRAS (2014)

4.1 Introduction

It is generally accepted that both stellar mass and supermassive black holes have been definitively detected in large numbers. Intermediate mass black holes (IMBHs), on the other hand, have never been detected with such certainty and even the strong candidates are few in number (Gladstone 2013). Moreover, there has been a long history of IMBH candidates turning out to be not needed or other, less exotic, objects (e.g. Baumgardt et al. 2003; Schödel et al. 2005). There are indeed several IMBH candidates, but still definitive proof and precise mass measurements of them elude the community. In this letter we estimate the number of IMBHs in the local universe, based on the assumption that IMBHs do in fact exist, that the strongest IMBH candidate is representative of the yet unknown population of IMBHs, and that all the X-ray outburst from suspected IMBHs are the result of mass transfer directly from stars in orbit around the IMBH which are overflowing their Roche lobe (Kaaret and Feng 2007; Lasota et al. 2011).

The benefit of estimating the size of a hereunto unknown population of IMBHs is in understanding the expectation of observing additional IMBHs in the future. If IMBHs are plentiful then they will play an important, and interesting, role in the evolution of galaxies (Ebisuzaki et al. 2001). In that case it will be important to seek out these objects to fully understand their role, and doing so will require carefully constructed experiments and observation time on telescopes to carry out those experiments. If, however, IMBHs are indeed very rare, were they the seeds of the current supermassive black holes or could the few examples simply be "failed" supermassive black holes? In this case, theorists need to work hard to understand why Nature, while so willing to allow for both its small and truly massive brethren, is stingy with these middle-child black holes.

Currently the strongest IMBH candidate is HLX-1. Though there are other suggestions about its true nature (King and Lasota 2014), its very unusual properties give it the strongest chance of being an IMBH. M82 X-1 is also a strong IMBH candidate, with mass estimates ranging from a couple $\times 10^2$ to 10^3 $M_\odot$. For this work we will consider HLX-1 and M82 X-1 as the only bona fide ultra luminous X-ray source IMBHs observed to date.

4.2 Observational Constraints HLX-1 and M82 X-1

Ultraluminous X-ray sources are defined as being extra-nuclear in location and having an X-ray luminosity in excess of 10^{39} erg s^{-1} (Roberts 2007). Farrell et al. (2009) identified a unique, extra-nuclear source in the edge-on spiral

galaxy ESO 243-49 with an X-ray luminosity in excess of 10^{42} erg s^{-1}. Using the term coined by Matsumoto et al. (2004), hyperluminous X-ray source (HLX), Farrell et al. (2009) called this object HLX-1. Based on the nature of HLX-1 they suggested that it was the premier IMBH candidate. Mass estimates for HLX-1 have ranged from > 500 $M_\odot$ (Farrell et al. 2009), to between 9.2×10^3 and 9.2×10^4 $M_\odot$(Webb et al. 2012), to between 6.3×10^3 and 1.9×10^5 $M_\odot$ (based on modeling of the accretion disk while varying the spin of the hole; Straub et al. 2014). After continued observations Webb et al. (2012) showed a very regular X-ray outburst frequency of once per year, although the most recent outburst, starting at the end of 2013, was delayed by more than 30 days (Godet et al. 2014). The peak luminosity corresponds to an accretion rate of 4×10^{-4} $M_\odot$ yr^{-1} (Godet et al. 2012). Wiersema et al. (2010), using Hα emission, found HLX-1 to be at a redshift consistent with ESO 243-49, and placed HLX-1 inside ESO 243-49, at a distance of 95 Mpc. Another popular IMBH candidate, M82 X-1, is located 5.2 Mpc away (Liu and Bregman 2005), with an X-ray luminosity of 5×10^{40} erg s^{-1} and 62 day period (Kaaret and Feng 2007), and a mass between $\approx 3 \times 10^2$ and 10^3 $M_\odot$ (Pasham et al. 2014; Mucciarelli et al. 2006). Though several estimates place its mass as low as ≈ 20 $M_\odot$ (Dewangan et al. 2006; Okajima et al. 2006).

4.3 Methods

In order to estimate the number of IMBHs in the local universe we must know the probability of detecting such objects. This probability is based on the likelihood of a star of a given mass orbiting the black hole, the length of time that star would be transferring enough mass to produce an X-ray flux above the background, and the probability of detecting such an object given the sensitivity of the observatory. The number of observed IMBHs can thus be described as:

$$N_{obs} = N_{IMBH} \times N_{mass\ transfer} \times P_{detection}. \tag{4.1}$$

We find the number of IMBHs by solving for N_{IMBH}:

$$N_{IMBH} = \frac{N_{obs}}{N_{mass\ transfer} \times P_{detection}}. \tag{4.2}$$

Where N_{IMBH} is the number of IMBHs, N_{obs} is the number of IMBHs observed as ULXs, we assume currently this limited to HLX-1 and M82 X-1. $N_{mass\ transfer}$ is the average number of stars that an IMBH will have in an orbit such that the star could overflow its Roche lobe (RLOF) and thus able to transfer mass onto the hole. Extrapolating from a linear fit of the simulation data of Blecha et al. (2006) we find that a 10^3 and 10^4 $M_\odot$ black hole should have, on average, 2.2 and 19.6 stars, respectively, in a mass transferring orbit

over the duration of their simulations (100 Myr). $P_{detection}$ is dependent on the probability that the system is in an 'active' state. But different stellar masses have different active times so we must scale the probability a system is active by the probability that a given mass would be present around an IMBH, i.e. using the normalized mass function found around the black hole; that is,

$$P_{detection} = \int_{M_{min}}^{M_{max}} P_{active} \times P_{mass|mass\ function} dm. \tag{4.3}$$

The likelihood of finding the star-black hole system in an active state, i.e. P_{active}, is the fraction of the star's lifetime spent transferring mass above a given rate. Because the star is transferring mass its evolution and lifetime are altered and so we must perform stellar evolution simulations of stars which are losing mass via RLOF. In Section 4.3.1 we provide more details about the simulations we perform. We convert the measured mass transfer rate to an X-ray luminosity using a 10 per cent efficiency rate and assuming that all of the mass lost from the star is accreted onto the black hole, and then we calculate the fraction of time spent over a given luminosity.

Lastly, $P_{mass|mass\ function}$ is measured from data taken from simulations of IMBH formation via collision run away (Fujii et al. 2012). Measurement of this value is addressed at length in Section 4.3.2.

4.3.1 Mass Transfer

In order to measure the fraction of time a star of a given mass would spend transferring mass to its IMBH companion to the total age of the star, P_{active}, we have run stellar evolution models of stars as they transfer mass to an IMBH. We have used a stellar evolution code and numerical methods to model a star in orbit around an IMBH wherein we vary the mass of both the IMBH and stars, as well as the eccentricity of the orbit. The star is placed on an orbit with a given eccentricity and its semi-major axis is allowed to grow such that it is always just over flowing its Roche lobe at pericenter, it is then evolved, using the AMUSE framework (Portegies Zwart et al. 2012; Pelupessy et al. 2013), with the stellar evolution code MESA (Paxton et al. 2011). At every step of the evolution the amount of mass transfer, $\dot{m}$, from the star to the IMBH is calculated based on the analytical prescription described below and that mass loss is provided to the stellar evolution code which adjust the evolution accordingly. With such models we determine the time spent transferring mass above a certain rate, the lifetime of the star given this mass loss rate, and if such a model could produce a system as described in Lasota et al. (2011).

We calculate the mass loss from the donor by solving Equation 1 in Portegies Zwart et al. (2004) which provides a calculation for the change of the

semi-major axis, $\dot{a}$, based on the effects of gravitational radiation, Roche lobe overflow and mass loss via stellar wind. For our calculations we neglect the wind and assume that the mass in the system is conserved, then solving for $\dot{m}$ we find:

$$\dot{m} = \left(\frac{\dot{a}}{a} - \frac{64}{5} \frac{G^3}{c^5} \frac{m_\star m_\bullet m_t}{a^4} \right) / \left(\frac{2}{m_\star} - \frac{2}{m_\bullet} \right), \tag{4.4}$$

where a and $\dot{a}$ are the semi-major axis and its time derivative respectively; G and c are the gravitational constant and the speed of light in vacuum respectively; and finally $m_\star$, $m_\bullet$, and m_t are the masses of the donor star, the black hole, and the total system mass respectively.

Our simulations are very similar to those found in Patruno et al. (2005), Madhusudhan et al. (2008), and Patruno and Zampieri (2008), the primary difference being that we calculate the mass loss from the donor via the methods in Portegies Zwart et al. (2004) for $\dot{m}$ and then evolve the companion in a stellar evolution code to which we provide the mass loss rate we have calculated. The secondary difference between our method and those of the previous works is that we calculate the size of the Roche lobe with a correction for the eccentricity of the orbit based on Equations 51 and 52 of Sepinsky et al. (2007). Even with these two differences our work agrees well with the previous work.

From these simulations we calculate the mass transfer per unit time, i.e. the luminosity, and the orbital period of the star around the black hole.

4.3.2 Mass Function

In order to calculate the probability of a star being in orbit around an IMBH, $P_{mass|mass\ function}$, we must first know how the stellar masses are distributed, i.e. the mass function near the black hole. We perform these calculations using two different mass functions. First, we calculate the probability of a star of a given mass orbiting a black hole by using a Salpeter mass function (Salpeter 1955) with masses between 1 and 100 $M_\odot$. This generic stellar mass distribution yields a probability distribution function of:

$$PDF_{SP} = 1.35 \times M^{-2.35}. \tag{4.5}$$

Where M is the mass of the star in units of $M_\odot$.

The second mass function we used is derived from N-body simulations by Fujii et al. (2012). In their set of simulations stars were allowed to collide and merge which in some cases resulted in a collision runaway, producing very massive stars of up to about 500 $M_\odot$. Upon their death stars of such a mass would produce an IMBH (Portegies Zwart and van den Heuvel 2007). Portegies Zwart and McMillan (2002) suggested this method for IMBH formation. Fujii et al. (2012) have provided a successful test of this possible formation theory. In that work they used the Salpeter function as their initial mass function,

but after 3 Myr the mass function near the black hole had changed dramatically with a larger fraction of high mass stars near the black hole than the Salpeter function would have predicted. As we will mention later, this has a dramatic effect on the number of predicted IMBHs, and we speculate that the careful choice of a realistic mass function will have a similarly profound impact on the results of other studies. But the significance for this work lies in being able to measure the distribution of stellar masses near a newly formed IMBH. By deriving the mass function from a self-consistent N-body simulation of collision runaway we are able to produce a much more realistic mass function for what might be found around an IMBH. We used the data from when the cluster was ≈ 3 Myr old, as that corresponds to when the very massive star would collapse into an IMBH (Portegies Zwart et al. 1999). We find that a broken power law of the form:

$$\frac{M^{-2}}{65}, \quad \text{for } 1\ M_\odot \leqslant M \leqslant 11\ M_\odot \tag{4.6}$$

$$40M^{-1.05}, \quad \text{for } 11\ M_\odot \leqslant M \leqslant 100\ M_\odot \tag{4.7}$$

describes this more realistic mass function for the 500 stars closest to the black hole in these simulations. However, if we consider only the stars in the sphere of influence of the black hole we find that the data are best fit by a single power law of the form:

$$M^{-1.83}, \quad \text{for } 1\ M_\odot \leqslant M \leqslant 75\ M_\odot. \tag{4.8}$$

From this we obtain a probability distribution function of:

$$PDF = 0.85 \times M^{-1.83}. \tag{4.9}$$

4.4 Results and Discussion

We have run stellar evolution simulations of stars transferring mass to black holes with masses of 10^3, 10^4, and 10^5 $M_\odot$ with 17 different stellar masses between 4 and 40 $M_\odot$ and orbital eccentricities of 0.7, 0.8, 0.9, 0.95, and 0.99. Figure 4.1 is a plot of the stellar mass (bottom panel) and corresponding X-ray luminosity due to mass accreation onto the black hole (top panel). The mass of the black hole is 10^4 $M_\odot$ and the orbital eccentricity is 0.99. For clarity we have only plotted five different initial stellar masses of the 17 such simulations we ran for all black hole masses and eccentricities we examined.

From Figure 4.1 we note that the average X-ray luminosity increases with initial stellar mass. However, the peak luminosity is more consistent; we find a dramatic increase in luminosity at the end of the star's luminosity curve. This results from these stars going through a giant stage, quickly growing the stellar

radius and so a large amount of mass falls outside of the Roche lobe at pericenter. This can be seen in the bottom panel of Figure 4.1 with the sudden mass loss at the same time. After this impressive mass loss the star's envelope remains well within the Roche lobe and so there is generally no more mass loss. For initial masses less than or equal to 11 $M_\odot$ this can, but does not always, happen a second time though generally with a lower luminosity. The peak luminosity, $\approx 10^{42}$ erg s^{-1}, is fairly constant for these events, with only a weak dependency on initial mass. We find these results hold regardless of black hole mass and orbital eccentricity, but that is partially due to our assumptions that all of the mass lost from the star falls onto the black hole and that we do not allow the orbit to circularize. Allowing the orbit to circularize would have a limited effect because mass transfer rates are only very weakly related to the eccentricity of the orbit in our approximation (see e.g. Equation 4.4).

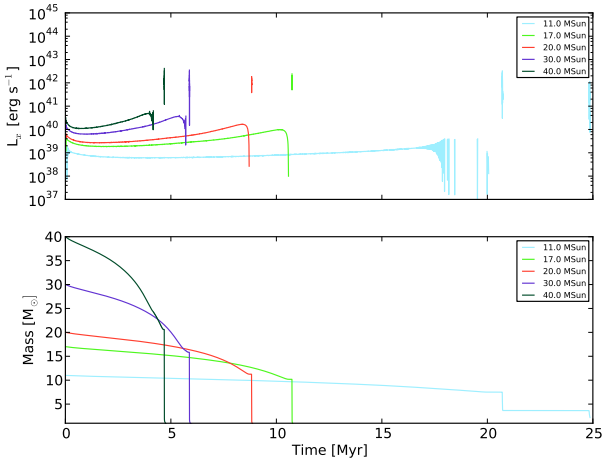


Figure 4.1: The mass and X-ray luminosity as a function of time. The top panel shows the X-ray luminosity while the bottom panel shows the mass for five different initial masses as shown in the legend.

4.4.1 The Mass of HLX-1's Companion and the Mass Function Around the IMBH

Though we have not plotted it here, we also determine the evolution of the associated orbital period for all the simulations. If our aim were to reproduce HLX-1 with the added constraint of its roughly one year period we find only a relatively small range of initial stellar masses, between 10 and 11 $M_\odot$, that can produce the observed peak luminosity and the period simultaneously. This

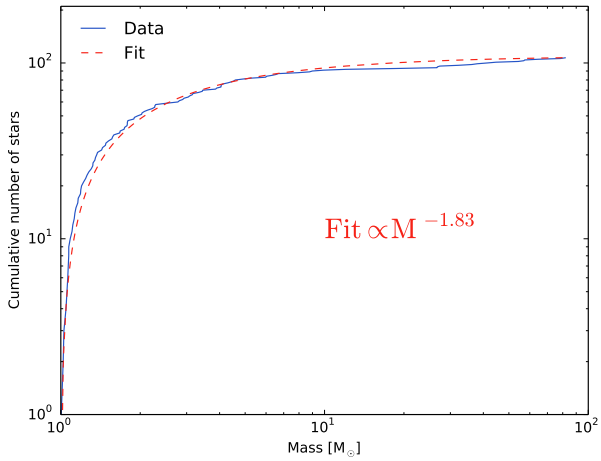


Figure 4.2: The cumulative number of stars as a function of mass. The red dashed line is the fit to the data (solid blue line). The fit is a power law with a slope of -1.83.

mass estimate is less than the turnoff mass of the young cluster around HLX-1 based on the age estimate from Soria et al. (2012) and is inline with the turnoff mass from the age estimate of Farrell et al. (2012), 6 and 13 Myr respectively. This would exclude the both sets of results which suggest a companion mass of either ≈ 2 or 20 $M_{\odot}$.

In Figure 4.2 we have plotted the stellar mass function in the sphere of influence of an IMBH just after formation via collision runaway. The solid blue line plots the cumulative number of stars as a function of mass, and the dashed red line plots the fit to the data. We find that the best fit is a power law with a slope of -1.83.

4.4.2 The Number of IMBHs

Using the stellar evolution simulations, the mass function near a newly formed IMBH, and Equation 4.2 we find that there should be $\approx 10^6$ black holes like HLX-1 within 100 Mpc. If these were to be distributed uniformly throughout that volume we would expect ≈ 1 IMBHs per cubic Mpc, however these objects will be preferentially found in and around galaxies. Using Gourgoulhon et al. (1992) we estimate $\approx 10,000$ galaxies within that volume and assuming IMBHs are equally distributed amongst all galaxies we predict ≈ 100 such IMBHs per galaxy. Of course, if these numbers are dryamtically wrong it would suggest that, for example, our mass transfer model is wrong or that HLX-1 is not an IMBH.

Applying the same methods to M82 X-1 we find there should be $\approx 10^6$ M82 X-1black holes within 22 Mpc (the distance at which M82 X-1 would become unobservable with a flux limit of 10^{38} erg s^{-1} Mpc^{-2}). Assuming a constant IMBH density we extrapolate that there should be $\approx 10^8$ of these lower-mass IMBHs within 100 Mpc. Again using the 10,000 galaxies from Gourgoulhon et al. (1992) we estimate there should be $\approx 10^4$ M82 X-1 like black holes within an average galaxy.

While 10^4 may seem large, the mass of M82 X-1 is estimated to be between a couple $\times 10^2$ and 10^3 $M_\odot$ and if IMBH masses are distributed along a continuum it does not seem unreasonable that there would be, for example, many more 5×10^2 $M_\odot$ than 10^4 $M_\odot$ IMBHs (such as HLX-1). An additional concern may be where to harbor so many objects; globular clusters seem to be a natural place to find such objects and with about 160 globular clusters in our Galaxy our prediction for the number of more massive objects, i.e. the $\approx$ 100 which are HLX-1 like, would, as an order of magnitude estimate, fit neatly within the number of globular clusters.

The lower mass,$10^2 - 10^3$ $M_\odot$, IMBHs could form, via collision runaway, and reside in young clusters as suggested in van den Heuvel and Portegies Zwart (2013), who also claim the signature of the formation of these IMBHs would be superluminous supernovae (SLSNe). Assuming SLSNe always produce an IMBH we can estimate IMBH numbers from the number of SLSNe. Gal-Yam (2012) provides a rate for SLSNe of 10^{-8} Mpc^{-3} yr^{-1}, giving:

$$10^{-8}\ \mathrm{Mpc}^{-3}\mathrm{yr}^{-1} \times 10^{10}\mathrm{yr} \times (10^2\mathrm{Mpc})^3 = 10^8\ \mathrm{SLSNe} \qquad (4.10)$$

within the age of the Universe and out to a distance of 100 Mpc. Perhaps surprisingly, this second method, using a physically unrelated model, serendipitously agrees with the results we found using the method outlined above. Additionally, we note that van den Heuvel and Portegies Zwart (2013) suggest that these events, and hence IMBHs, are not equally distributed amongst galaxies but rather they find that the Milky Way is expected to under-produce these events by a factor of 10^2 compared to compact blue galaxies. This means the number of lower mass IMBHs in the Milky Way could be as low as 10^2.

As these young clusters evaporate, if they evaporate, their IMBHs would be left with at most only the few stars within the IMBH's sphere of influence. If there are such low-mass IMBHs threading their way though the Milky Way then Gaia may provide a unique opportunity to spot them.

As Gaia (de Bruijne 2012) observes a billion or so stars in the Milky Way, making very high precision measurements of the peculiar motion of the stars, it should observe some systems for which their motions can only be explained with the addition of an IMBH. However, if there are in fact only 10^2 such IMBHs in the Milky Way, and Gaia is only sampling 1 out of every 10^2 stars

in the Milky Way we would expect to detect on order of 1 of these objects. Of course, as with the rest of this letter, caution must be taken when considering such low number statistics.

The spatial distribution of these systems should not deviate much from their initial distribution, at least not as a result of dynamical friction since for the 10^3 $M_\odot$ case dynamical friction should only result in an inward migration of the black hole of ≈ 40 pc, and only ≈ 0.4 kpc even for a 10^5 $M_\odot$ black hole in 13 Gyr (assuming a value of 6 for the Coulomb logarithm). Additionally, the all-sky, X-ray survey provided by eROSITA (Merloni et al. 2012), with an anticipated launch data in 2016, will likely provide many more IMBH candidates with its sensitivity and long expected exposure time.

4.4.3 IMBHs in Relation to Other Black Holes

Finally, in Table 4.1 we compile the number and total mass of different types of massive objects (stars, stellar mass black holes (StMBHs), IMBHs, and SMBHs) in both our Galaxy and with a sphere with a radius of 100 Mpc. Here we outline how we arrived at these values: In the Milky Way there is one observed SMBH, Sgr A*, with a mass of 4.1×10^6 $M_\odot$ (Ghez et al. 2008). Caramete and Biermann (2010) estimate a total number of SMBHs within 100 Mpc with masses $> 10^7$ $M_\odot$ to be about 2.4×10^4 and from the mass density provided therein we estimate a total mass of 2.8×10^{11} $M_\odot$ within the same volume. We must be careful to note that while the number of SMBHs within 100 Mpc may be larger due to excluding the SMBHs with masses $< 10^7$ Caramete and Biermann (2010) claim the total mass is barely dependent on the cutoff due to a flattening of the integral mass function at lower mass. In this work we have calculated the values for the number of IMBHs within 100 Mpc and within the Milky Way. In order to estimate the total mass of the IMBHs we used the data of Moran et al. (2014) and find an average IMBH mass of $\approx 6.7 \times 10^3$ $M_\odot$ and we assume this value for both within 100 Mpc and the Galaxy. To find the number of StMBHs we estimate that approximately 1 out of every 1000 stars in a Kroupa mass function (Kroupa 2001) are massive enough ($> 20\,M_\odot$) to produce a StMBH at the end of their life, and Özel et al. (2010) provided an estimate of typical Galactic StMBH to be 7.8 $M_\odot$—again we assume this value is valid within 100 Mpc in addition to the Milky Way. The number of stars in the Milky Way is $\approx 3 \times 10^{11}$ and we measure the average stellar mass from a Kroupa mass function to be ≈ 0.4 $M_\odot$ for a total mass of 1.2×10^{11} $M_\odot$. To find the number of stars within 100 Mpc we take the stellar mass density from Dickinson et al. (2003) and find a total stellar mass of 4×10^{14} $M_\odot$, continuing to use an average stellar mass of 0.4 $M_\odot$ we then find 1×10^{15} stars. We find an ideal fit of the number of black holes versus mass

	In Milky Way		Within 100 Mpc	
	Number	$M_{total}[M_\odot]$	Number	$M_{total}[M_\odot]$
SMBH	10^0	4.1×10^6	2.4×10^4	2.8×10^{11}
IMBH	1×10^4	6.7×10^7	1×10^8	6.7×10^{11}
StMBH	3×10^8	2.1×10^9	4×10^{11}	2.8×10^{12}
Stars	3×10^{11}	1.2×10^{11}	1×10^{15}	4×10^{14}

Table 4.1: The estimated number and total mass of SMBHs, IMBHs, StMBHs, and Stars within the Milky Way (left two columns) and within 100 Mpc (right two columns).

with a power law of the form:

$$N = 4.95 \times 10^9 M^{-1.47}, \tag{4.11}$$

where N and M are the number and average mass of the black holes, respectively.

4.5 Conclusion

We have determined the stellar mass function within the sphere of influence of a newly formed IMBH to be of the form $M^{-1.5}$. This mass function combined with the fraction of time a star is transferring mass to the black hole, the probability that an IMBH would have a star in an orbit that it could transfer mass via RLOF, and the number of IMBHs observed allows us to estimate the number of IMBHs within 100 Mpc (the distance to HLX-1). We find that within 100 Mpc there should be on the order of 10^8 IMBHs, the majority being M82 X-1 like ($10^2 - 10^3$ $M_\odot$) with only 10^6 being HLX-1 like (10^4 $M_\odot$). This translates into $\approx 10^4$ IMBHs within each galaxy in that volume assuming they are equally distributed amongst 10^4 galaxies. The uncertainty in our estimation is dominated by our assumptions (e.g. that IMBHs exist in this current epoch, that HLX-1 and M82 X-1 are such IMBHs and are representative of a larger population, that ULX IMBHs are powered by RLOF and there are not more than a few other RLOF powered IMBHs currently in an active state, etc.) which make estimating the error a bit artificial; if for example, the mass is not being accreted via RLOF or HLX-1 and M82 X-1 are not IMBHs then our model is not able to estimate this population. However, if there is dramatically more than an order of magnitude of unidentified RLOF powered IMBHs within the flux limits of current surveys then we could have underestimated the number. Due to these difficulties we estimate the error to be at least an order of magnitude. We are hopeful that results from Gaia and the upcoming X-ray mission eROSITA (Merloni et al. 2012) will help to clarify many of these outstanding questions and perhaps identify IMBHs through dynamical means.

As an unexpected result we found that a simultaneous fit to the mass loss and apparent period of the star overflowing its Roche lobe to HLX-1 was only possible in our simulations with a companion mass between 10 and 11 $M_{\odot}$. This is also in line with the turnoff mass based on the age estimate of the young cluster around HLX-1. However, this mass estimate would exclude a suggestion that the companion is 2 or 20 $M_{\odot}$.

Finally, we show in Table 4.1 how our results of expected number of IMBHs compares to other estimates of numbers and mass of stars, StMBHs, and SMBHs in our Galaxy and within 100 Mpc. We find that the number and total mass in IMBHs that we predict seems to fit well within these ranges. Fitting the number of black holes versus mass with a power law we find $N = 4.95 \times 10^9 M^{-1.47}$ produces a fit with an R^2 value of 1.0.

4.6 Acknowledgments

We are very grateful to Michiko Fujii for providing us with her data, as well as Alex Rimoldi and Edwin van der Helm for their thoughtful comments.

CHAPTER 5 Asymmetric Supernova in Hierarchical Multiple Star Systems and Application to J1903+0327

We develop a method to analyze the effect of an asymmetric supernova on hierarchical multiple star systems and we present analytical formulas to calculate orbital parameters for surviving binaries or hierarchical triples and runaway velocities for their dissociating equivalents. The effect of an asymmetric supernova on the orbital parameters of a binary system has been studied to great extent (e.g. Hills 1983; Kalogera 1996; Tauris and Takens 1998), but this effect on higher multiplicity hierarchical systems has not been explored before. With our method, the supernova effect can be computed by reducing the hierarchical multiple to an effective binary by means of recursively replacing the inner binary by an effective star at the center of mass of that binary.

We apply our method to a hierarchical triple system similar to the progenitor of PSR J1903+0327 suggested by Portegies Zwart et al. (2011). We confirm their earlier finding that if PSR J1903+0327 could have evolved from a hierarchical triple that became unstable and ejected the secondary star of the inner binary, it would be most probable to have had a small supernova kick velocity, the inner binary would likely have had a large semi-major axis, and the fraction of mass accreted onto the neutron star to the mass lost by the secondary most likely be between 0.35 and 0.5.

In collaboration with:
Tjibaria Pijloo & Simon Portegies Zwart.

MNRAS 424, 2914 (2012)

5.1 Introduction

Asymmetric supernovae in binary and hierarchical multiple star systems form a crucial phase in the formation of stellar systems containing a compact stellar remnant - neutron star or black hole. In previous studies of supernovae in binaries two effects of the supernova are considered: 1) sudden mass loss of, and 2) a random kick velocity imparted on the compact remnant of the star undergoing the supernova. The combined effect which changes the orbital parameters causes the binary to dissociate in the majority of the cases.

The study of binaries surviving a supernova (SN) explosion of one of its components was first performed by Blaauw (1961) and Boersma (1961), assuming a symmetric SN (i.e. only mass loss). The necessity of asymmetry in the SN, resulting in the kick velocity, was first suggested by Shklovskii (1970). The statistical study on pulsar scale heights by Gunn and Ostriker (1970) firmly supported the asymmetric SN model and to date the adding of the kick velocity to the newly born neutron star (or black hole) is a commonly excepted mechanism (van den Heuvel and van Paradijs 1997). Both the type of explosion mechanism and whether the exploding star is in a binary system are found to influence the effect of the kick velocity (see e.g. Podsiadlowski et al. 2004), but the exact physical process underlying the production of kicks remains unclear. The analysis of the effect of asymmetric supernovae on binaries has been sufficient to explain most of the observed post-SN stellar systems, and little to no effort has gone into studying the effect on hierarchical multiple star systems.

Millisecond pulsar (MSP) J1903+0327 (spin period $\simeq$ 2.15 ms), first observed by Champion et al. (2008) and later, in more detail, by Freire et al. (2011), is part of what may be the first observed MSP binary to have evolved from a hierarchical triple progenitor. MSP J1903+0327 is orbited by a main sequence star in a wide (orbital period $\simeq$ 95.2 days) and eccentric (eccentricity $e \simeq 0.44$) orbit. Based on these observables it seems impossible that this binary (hereafter J1903+0327) formed via the traditional mechanism in a binary progenitor (Champion et al. 2008). Portegies Zwart et al. (2011) proposed that the progenitor system was a binary accompanied by a third and least massive main-sequence star in a wider orbit about this binary. During the low-mass X-ray binary (LMXB) phase of the inner binary, the orbit of the LMXB expanded due to mass transfer from the evolving inner companion (donor) star to the neutron star, which was formed in the SN. This eventually caused the triple to become dynamically unstable and to eject the inner companion resulting in the observed system J1903+0327.

J1903+0327 is not a unique case, however: there is a significant number of systems like the progenitor of J1903+0327 as suggested in Portegies Zwart et al. (2011) and similar hierarchical stellar systems of higher multiplicity. The Multiple Star Catalog lists 602 triples, 93 quadruples, 22 quintuples, 9 sextuples

and 2 septuples (Tokovinin 1997) of which 90 systems contain at least one star with a mass $M \geqslant 10$ M$_\odot$. Each of these multiples will eventually experience a core-collapse SN of the most massive star. After the SN these systems are either fully dissociated, dissociate into lower multiplicity multiple star systems, or survive the SN.

We begin the study of the effect of an asymmetric SN on hierarchical multiple star systems by first readdressing the SN effect on a binary and subsequently treating the effect in a hierarchical triple. We show that a hierarchical triple can effectively be regarded as a binary system comprised of the center of mass of the inner binary and the tertiary star. The effect of a SN on a hierarchical triple system, now reduced to an effective binary, can be calculated using the prescription for a SN in binary. We ultimately generalize this effective binary method to hierarchical multiple star systems of arbitrary multiplicity. In the second part of the paper we perform Monte Carlo simulations of a hierarchical triple star system similar to the progenitor of J1903+0327 suggested in Portegies Zwart et al. (2011) to determine the (stable) survival rates, and evaluate whether such a formation route is plausible.

5.2 Calculation of post-SN parameters

5.2.1 Binary systems

We consider a binary system of stars with mass, position and velocity for the primary and secondary star, given by ($m_{1,0}$,$\mathbf{r_1}$,$\mathbf{v_{1,0}}$) and (m_2,$\mathbf{r_2}$,$\mathbf{v_{2,0}}$) respectively[1], in which the primary undergoes a SN. The binary system is uniquely described by the semi-major axis, a_0, eccentricity, e_0, and true anomaly, θ_0. The separation distance is $\mathbf{r_0}$. We assume that the SN is instantaneous, meaning an instantaneous removal of mass of the primary, no SN-shell impact on the companion (secondary) star, and the orbital motion during this mass loss phase is neglected, i.e. $\mathbf{r} = \mathbf{r_0}$ and $\mathbf{v_2} = \mathbf{v_{2,0}}$.

After the SN the orbital parameters have changed to: semi-major axis, a, eccentricity, e, and true anomaly, θ. For a general Kepler orbit of two objects with masses m_1 and m_2 respectively, a relative velocity, v, semi-major axis, a, and separation distance, r, the orbital energy conservation equation is

$$v^2 = G(m_1 + m_2)\Big(\frac{2}{r} - \frac{1}{a}\Big), \tag{5.1}$$

[1]The contingent suffix 1, 2, etc. indicates which star we are considering (e.g. 1 for the primary). The contingent suffix 0 denotes the pre-SN state and when it is absent, it either refers to the post-SN state or the absence indicates that there is no difference in the pre- and post-SN states of that parameter.

where G is Newton's gravitational constant. The specific relative angular momentum $\mathbf{h}$ is related to the orbital parameters as follows

$$\begin{aligned} |\mathbf{h}|^2 &= |\mathbf{r} \times \mathbf{v}|^2 && (5.2) \\ &= G(m_1 + m_2)a(1 - e^2), && (5.3) \end{aligned}$$

where the first equality holds for all Kepler orbits and the second only applies to bound orbits. For thorough studies on SNe in a binary system see Hills (1983), Kalogera (1996), and Tauris and Takens (1998); the latter authors also take into account the shell impact on the companion star using a method proposed by Wheeler, Lecar, and McKee (1975). Following the mentioned works as guides for our calculations on the binary system we use a total pre-SN mass of $M_0 = m_{1,0} + m_2$. Without loss of generality, we choose a coordinate system in which at $t = 0$ the orbit lies in the xy-plane, the center of mass of the binary (cm) is at the origin, the y-axis is the line connecting the primary and the secondary (the cm coordinate system; see Figure 5.1), and we choose a reference frame in which at $t = 0$ the cm is at rest (the cm reference frame).

Before the SN the separation distance between the stars is

$$\mathbf{r} = \mathbf{r_1} - \mathbf{r_2} = \left(0, -\frac{a_0(1 - e_0^2)}{1 + e_0 \cos\theta_0}, 0\right). \tag{5.4}$$

Using the following notation

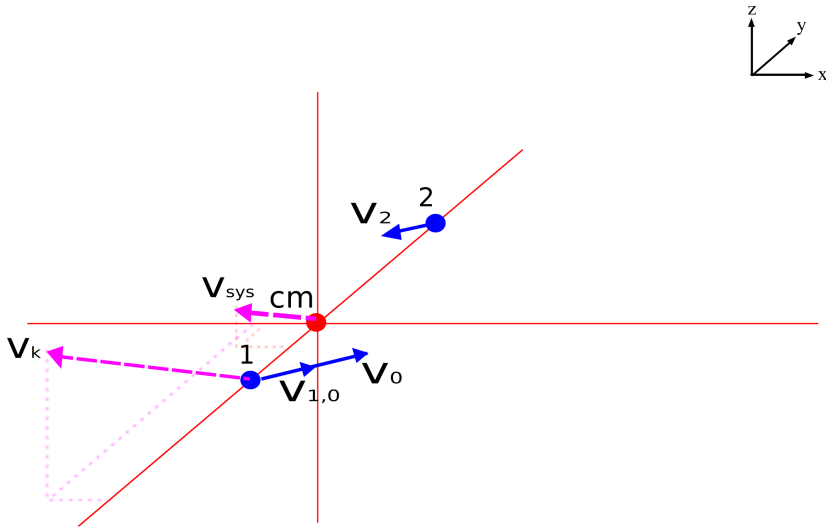
$$\begin{aligned} x &= a_0\sqrt{1 - e_0^2}\cos\gamma_0 \cos\theta_0 + a_0 \sin\gamma_0 \sin\theta_0, \\ y &= -a_0\sqrt{1 - e_0^2}\cos\gamma_0 \sin\theta_0 + a_0 \sin\gamma_0 \cos\theta_0, \\ v_{0x} &= v_0 \frac{x}{\sqrt{x^2 + y^2}}, \\ v_{0y} &= v_0 \frac{y}{\sqrt{x^2 + y^2}}, \end{aligned}$$

in which γ_0 is the pre-SN eccentric anomaly defined by $r = a_0(1 - e_0 \cos\gamma_0)$, the velocity of the primary relative to the secondary is

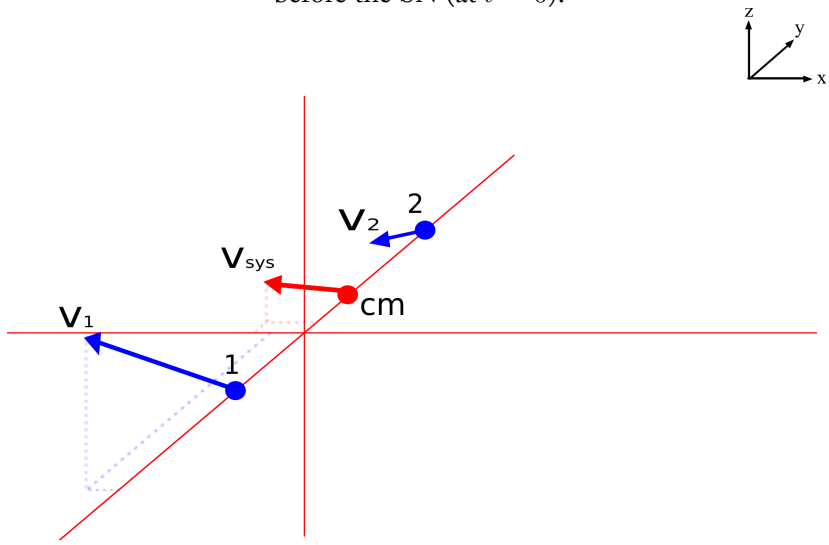
$$\mathbf{v_0} = \mathbf{v_{1,0}} - \mathbf{v_2} = (v_{0x}, v_{0y}, 0). \tag{5.5}$$

After the SN the primary has lost a part of its mass, Δm, and has obtained a velocity kick $\mathbf{v_k}$ in a random direction, which makes an angle ϕ with the pre-SN relative velocity $\mathbf{v_0}$. The velocity of the primary relative to the secondary, after the SN, is

$$\mathbf{v} = \mathbf{v_0} + \mathbf{v_k} = (v_{0x} + v_{kx}, v_{0y} + v_{ky}, v_{kz}), \tag{5.6}$$



a. The cm coordinate system in the cm reference frame for a binary system before the SN (at $t = 0$).



b. The cm coordinate system in the cm reference frame for a binary system after the SN.

Figure 5.1: Schematic representation of a binary system in the pre- and post-SN phase. The solid blue circles denote the primary and secondary star; the solid red cirle denotes the cm. The solid arrows denote the velocities the stars or cm have at that phase; the dashed arrows denote the velocity the SN imposes on the stars or cm which will change its velocity in the next phase. a. In the pre-SN phase the coordinate system is centered on the cm being at rest. b. In the post-SN phase the coordinate system is no longer centered on the cm - the cm has been translated in the y-direction, towards the secondary, and has gained a velocity v_{sys}. In both cases the inner binary orbital plane lies in the xy-plane and the y-axis is the line connecting the primary and the secondary.

the mass of the primary is $m_1 = m_{1,0} - \Delta m$ and the total binary mass is $M = M_0 - \Delta m$. Applying these relations and equations (5.1) and (5.2) to the binary system, we obtain equations relating the post-SN semi-major axis, a, and eccentricity, e, to both the pre- and post-SN orbital parameters and velocities. Using $v_{c,0} = v_0|_{r=a_0} = (GM_0/a_0)^{1/2}$ as the pre-SN relative velocity (Hills 1983), we obtain

$$\frac{a}{a_0} = \Big(1 - \frac{\Delta m}{M_0}\Big)\Big(1 - \frac{2a_0}{r}\frac{\Delta m}{M_0} - 2\frac{v_0}{v_{c,0}}\frac{v_k}{v_{c,0}}\cos\phi - \frac{v_k^2}{v_{c,0}^2}\Big)^{-1} \tag{5.7}$$

$$e^2 = 1 - (1-e_0^2)\frac{M_0^2}{(M_0-\Delta m)^2}\Big(1 - \frac{2a_0}{r}\frac{\Delta m}{M_0} - \frac{v_k^2}{v_{c,0}^2} - 2\frac{v_0}{v_{c,0}}\frac{v_k}{v_{c,0}}\cos\phi\Big) \tag{5.8a}$$

$$= 1 - \frac{a_0^2(1-e_0^2)^2}{a(1+e_0\cos\theta_0)^2}\frac{(v_{0x}^2 + v_{kx}^2 + v_{kz}^2 + 2v_{0x}v_{kx})}{G(M_0-\Delta m)}, \tag{5.8b}$$

which are consistent with Kalogera (1996). In §5.2.3 we present a few examples regarding the effect of mass loss and the supernova kick on the orbital parameters of hierarchical triples. To compute the systemic velocity of the binary system due to the SN, we begin by writing the pre-SN velocities of the primary and secondary in the cm reference frame; using the pre-SN mass ratio $\mu_0 = m_2/M_0$, these velocities are given by

$$\mathbf{v_{1,0}} = \mu_0\Big(v_{0x}, v_{0y}, 0\Big), \tag{5.9}$$

$$\mathbf{v_2} = (\mu_0 - 1)\Big(v_{0x}, v_{0y}, 0\Big). \tag{5.10}$$

As a result of the assumption of an instantaneous SN and neglecting the shell impact, the instantaneous velocity of the secondary remains unchanged after the SN, but the instantaneous velocity of the primary changes to

$$\mathbf{v_1} = \Big(\mu_0 v_{0x} + v_{kx}, \mu_0 v_{0y} + v_{ky}, v_{kz}\Big). \tag{5.11}$$

We now use the post-SN mass ratio $\mu = m_2/M$, and find the systemic velocity of the binary system:

$$\mathbf{v_{sys}} = (1-\mu)\mathbf{v_1} + \mu\mathbf{v_2} = (1-\mu)\Big(\frac{\mu_0-\mu}{1-\mu}v_{0x} + v_{kx}, \frac{\mu_0-\mu}{1-\mu}v_{0y} + v_{ky}, v_{kz}\Big). \tag{5.12}$$

These results are consistent with the previously mentioned studies on SN in binaries. As a conseqence a binary in which the compact object does not receive a kick in the supernova explosion moves through space like a frisbee.

Dissociating binary systems

The mass loss and the kick velocity have a potentially disrupting effect on the binary system. However, in cases where the mass loss alone would have been large enough to unbind the binary, the combination of the two can result in the binary system surviving the SN (Hills 1983). If the binary system dissociates, the two stars move away from each other on a hyperbolic or, in a limiting case, a parabolic trajectory. This corresponds to the cases where $a < 0$ and $e > 1$ (hyperbola) or $a \to \infty$ and $e = 1$ (parabola). From equation (5.7) we see that for a dissociating binary the angle ϕ between the kick velocity $\mathbf{v_k}$ and the pre-SN relative velocity $\mathbf{v_0}$ satisfies (Hills 1983):

$$\cos\phi \quad \geqslant \quad \Big(1 - \frac{2a_0}{r}\frac{\Delta m}{M_0} - \frac{v_k^2}{v_{c,0}^2}\Big)\Big(2\frac{v_k}{v_{c,0}}\sqrt{\frac{2a_0}{r} - 1}\Big)^{-1}. \qquad (5.13)$$

If the right-hand side of equation (5.13) is less than -1, the binary dissociates for all ϕ; but if it is greater than 1 the binary survives for all ϕ. If the right-hand side is within the range -1 to 1, the probability of dissociating the binary is (Hills 1983):

$$P_{diss} \quad = \quad \frac{1}{2}\Big(1 - \Big(1 - \frac{2a_0}{r}\frac{\Delta m}{M_0} - \frac{v_k^2}{v_{c,0}^2}\Big)\Big(2\frac{v_0}{v_{c,0}}\frac{v_k}{v_{c,0}}\Big)^{-1}\Big). \qquad (5.14)$$

Tauris and Takens (1998) presented analytical formulas to calculate the dissociation velocities for a binary with a pre-SN circular orbit. We follow their calculation for deriving the runaway velocities of the two stars in dissociating binaries, but for a pre-SN orbit of arbitrary eccentricity and we ignore the SN shell impact. We use the cm coordinate system, explained above. Using the

following shorthand relations

$$\begin{aligned}
\tilde{m} &= \frac{M}{M_0}, \\
j &= \frac{v_{0x}^2}{v_0^2} - 2\tilde{m}\frac{a_0}{2a_0 - r} + \frac{v_k^2}{v_0^2} + \frac{2v_{0x}v_{kx}}{v_0^2}, \\
k &= 1 + \frac{j}{\tilde{m}}\frac{2a_0 - r}{a_0} - \frac{v_{ky}^2}{\tilde{m}v_0^2}\frac{2a_0 - r}{a_0}, \\
l &= \frac{1}{\mu}\Big(\frac{\sqrt{j}}{\tilde{m}v_0}v_{ky}\frac{2a_0 - r}{a_0} - \frac{j}{\tilde{m}}\frac{2a_0 - r}{a_0} - 1\Big), \\
n &= \frac{1}{\mu}\Big(1 + \frac{j}{\tilde{m}}\frac{2a_0 - r}{a_0}(k+1)\Big),
\end{aligned}$$

we find the runaway velocities for the primary and secondary star:

$$\begin{aligned}
\mathbf{v_{1,diss}} &= \Big(v_{kx}\Big(\frac{1}{l} + 1\Big) + \Big(\frac{1}{l} + \mu_0\Big)v_{0x}, \mu_0 v_{0y} \\
&\quad + v_{ky}\Big(1 - \frac{1}{n}\Big) + \frac{k\sqrt{j}}{n}v_0, v_{kz}\Big(\frac{1}{l} + 1\Big)\Big), \qquad (5.15) \\
\mathbf{v_{2,diss}} &= \Big(-\frac{m_1 v_{kx}}{m_2 l} - \Big(\frac{m_1}{m_2 l} + 1 - \mu_0\Big)v_{0x}, (\mu_0 - 1)v_{0y} \\
&\quad + \frac{m_1 v_{ky}}{m_2 n} - \frac{m_1 k\sqrt{j}}{m_2 n}v_0, -\frac{m_1 v_{kz}}{m_2 l}\Big). \qquad (5.16)
\end{aligned}$$

5.2.2 Hierarchical triple systems

We now consider a hierarchical system of three stars with the primary, secondary and tertiary star having mass, position and velocity given by ($m_{1,0}$,$\mathbf{r_1}$,$\mathbf{v_{1,0}}$), (m_2,$\mathbf{r_2}$,$\mathbf{v_2}$) and (m_3,$\mathbf{r_3}$,$\mathbf{v_3}$) respectively. The primary star undergoes a SN and the inner binary configuration and parameters are the same as in section 5.2.1. The inner binary center of mass (cm) has a mass of $m_{cm,0} = m_{1,0} + m_2 = M_0$, is at position

$$\mathbf{r_{cm,0}} = (1 - \mu_0)\mathbf{r_1} + \mu_0\mathbf{r_2} \qquad (5.17)$$

and has a velocity

$$\mathbf{v_{cm,0}} = (1 - \mu_0)\mathbf{v_{1,0}} + \mu_0\mathbf{v_2}. \qquad (5.18)$$

The cm and tertiary constitute an outer binary defined by the semi-major axis, A_0, eccentricity, E_0, and true anomaly, Θ_0. The separation distance between the cm and the tertiary star we denote by $\mathbf{R_0}$. Before the SN the outer binary orbital plane has an inclination i_0 with respect to the inner binary and

the separation distance of the outer binary projected onto the xy-plane makes an angle α_0 with the separation distance of the inner binary. This inner-outer binary configuration is to some extent acceptable, because the triple is hierarchical. This implies that the separation distance of the cm and the tertiary is large compared to the separation distance of the primary and secondary, i.e. $R_0 \gg r_0$, so that the tertiary experiences gravitational influence of the inner binary as if it was coming from one star at the cm. We assume an instantaneous SN[2]. Due to the primary undergoing a SN, the inner binary experiences a mass loss Δm and an effective kick velocity is imparted to the cm: the systemic velocity of the inner binary $\mathbf{v_{sys}}$ given by equation 5.12. In addition, because of the reduction in mass of the primary, the position of the cm has changed due to an instantaneous translation along the y-axis

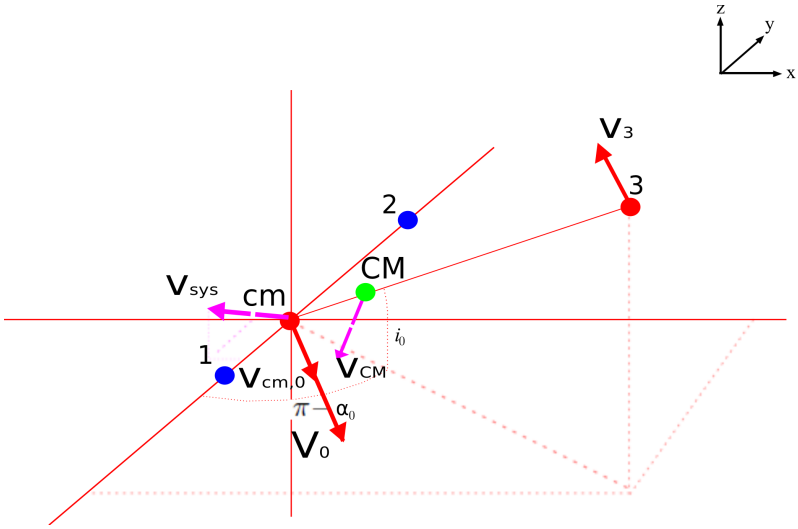
$$\begin{aligned} \mathbf{\Delta R} &= \mathbf{r_{cm}} - \mathbf{r_{cm,0}} \\ &= (\mu - \mu_0)\frac{a_0(1-e_0^2)}{1+e_0\cos\theta_0}\Big(0,1,0\Big). \end{aligned} \tag{5.19}$$

The orbital parameters change as a result of the SN: the inner binary parameters change according to the description in section 5.2.1 and the outer binary orbital parameters change to semi-major axis, A, eccentricity, E, and true anomaly, Θ. The hierarchical triple before the SN has a total mass $M_{t,0} = M_0 + m_3$. We use the cm coordinate system to pin down the inner binary and add to this coordinate system the tertiary at a position such that $R_0 \gg r_0$ (see Figure 5.2). We now select a reference frame in which the center of mass of the triple (CM) is at rest (the CM reference frame).

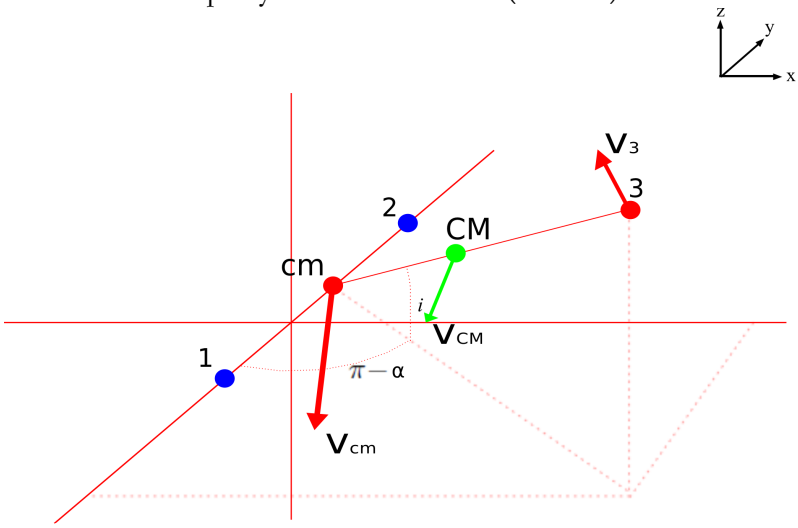
Prior to the SN the separation distance between the cm and the tertiary is

$$\mathbf{R_0} = \frac{A_0(1-E_0^2)}{1+E_0\cos\Theta_0}\Big(\cos i_0 \sin\alpha_0, -\cos i_0\cos\alpha_0, \sin i_0\Big), \tag{5.20}$$

[2]See section 5.2.1 and note that the statements about the inner companion (the secondary) also hold for the outer companion (the tertiary).



a. The cm coordinate system in the CM reference frame for a hierarchical triple system before the SN (at $t = 0$).



b. The cm coordinate system in the CM reference frame for a hierarchical triple system after the SN.

Figure 5.2: Schematic representation of a hierarchical triple star system in the pre- and post-SN phase. The solid blue circles denote the primary and secondary (inner binary); the solid red cirles denote the cm and the tertiary (outer binary); the green cirle denotes the CM. The solid arrows denote the velocities the stars or cm have at that phase; the dashed arrows denote the velocity the SN imposes on the stars or cm which will change its velocity in the next phase. a. In the pre-SN phase the coordinate system is centered on the cm being at rest. a. In the pre-SN phase the coordinate system is centered on the cm and the CM is at rest. b. In the post-SN phase the coordinate system is no longer centered on the cm - the cm has been translated in the y-direction, towards the secondary - and the CM is no longer at rest. In both cases the inner binary orbital plane lies in the xy-plane and the y-axis is the line connecting the primary and the secondary.

and, using the following shorthand notation

$$\begin{aligned}
X &= A_0\sqrt{1-E_0^2}\cos\Gamma_0\cos\Theta_0 + A_0\sin\Gamma_0\sin\Theta_0 \\
Y &= -A_0\sqrt{1-E_0^2}\cos\Gamma_0\sin\Theta_0 + A_0\sin\Gamma_0\cos\Theta_0 \\
X' &= X\cos\alpha_0 - Y\cos i_0\sin\alpha_0 \\
Y' &= X\sin\alpha_0 + Y\cos i_0\cos\alpha_0 \\
Z' &= Y\sin i_0 \\
V_{0x} &= V_0\frac{X'}{\sqrt{X'^2+Y'^2+Z'^2}} \\
V_{0y} &= V_0\frac{Y'}{\sqrt{X'^2+Y'^2+Z'^2}} \\
V_{0z} &= V_0\frac{Z'}{\sqrt{X'^2+Y'^2+Z'^2}}
\end{aligned}$$

in which Γ_0 is the pre-SN outer orbit eccentric anomaly defined by $R_0 = A_0(1 - E_0\cos\Gamma_0)$, the velocity of the cm relative to the tertiary is

$$\mathbf{V_0} = \mathbf{v_{cm,0}} - \mathbf{v_3} = (V_{0x}, V_{0y}, V_{0z}). \tag{5.21}$$

The effective kick velocity $\mathbf{v_{sys}}$ makes an angle Φ with the pre-SN relative velocity of the cm with respect to the tertiary star $\mathbf{V_0}$. After the SN the separation distance between the cm and the tertiary star is

$$\begin{aligned}
\mathbf{R} &= \mathbf{R_0} + \mathbf{\Delta R}, \\
&= \frac{A_0(1-E_0^2)}{1+E_0\cos\Theta_0}\Big(\cos i_0\sin\alpha_0, (\mu-\mu_0)\frac{a_0(1-e_0^2)}{1+e_0\cos\theta_0} \\
&\quad \times\frac{1+E_0\cos\Theta_0}{A_0(1-E_0^2)} - \cos i_0\cos\alpha_0, \sin i_0\Big),
\end{aligned} \tag{5.22}$$

the velocity of the cm relative to the tertiary star is

$$\begin{aligned}
\mathbf{V} &= \mathbf{V_0} + \mathbf{v_{sys}} \\
&= (V_{0x} + v_{sys,x}, V_{0y} + v_{sys,y}, V_{0z} + v_{sys,z}),
\end{aligned} \tag{5.23}$$

the cm mass is $m_{cm} = M_0 - \Delta m$ and the total triple mass is $M_t = M_{t,0} - \Delta m$. The inclination of the outer binary orbital plane with respect to the inner binary orbital plane is given by:

$$\sin i = \frac{|\mathbf{R_0}|}{|\mathbf{R}|}\sin i_0. \tag{5.24}$$

The angle of the outer binary separation distance projected onto the xz-plane relative to the inner binary separation distance is given by:

$$\sin\alpha = \frac{|\mathbf{R_0}|}{|\mathbf{R}|}\frac{\cos i_0}{\cos i}\sin\alpha_0. \tag{5.25}$$

Applying the relevant equations above and equations (5.1) and (5.2) to our triple system, we obtain equations relating the post-SN semi-major axis, A, and eccentricity, E, to both the pre- and post-SN orbital parameters and velocities. Using $V_{c,0} = V_0|_{R_0=A_0} = (GM_{t,0}/A_0)^{1/2}$ as the pre-SN relative velocity when $R_0 = A_0$, and using $\rho = (R_0 - R)/(R_0 R)$, we obtain

$$\begin{aligned}\frac{A}{A_0} &= \Big(1-\frac{\Delta m}{M_{t,0}}\Big)\Big(1-\frac{2A_0}{R}\frac{\Delta m}{M_{t,0}} - 2\frac{V_0}{V_{c,0}}\frac{v_{sys}}{V_{c,0}}\cos\Phi \\ &\quad -\frac{v_{sys}^2}{V_{c,0}^2} + 2A_0\rho\Big)^{-1},\end{aligned} \tag{5.26}$$

$$\begin{aligned}E^2 &= 1-(1-E_0^2)\frac{M_{t,0}}{(M_{t,0}-\Delta m)}\Big(\frac{2A_0}{R} + \frac{M_{t,0}}{M_{t,0}-\Delta m} \\ &\quad \times\Big(1-\frac{2A_0}{R_0} - \frac{v_{sys}^2}{V_{c,0}^2} - 2\frac{V_0}{V_{c,0}}\frac{v_{sys}}{V_{c,0}}\cos\Phi\Big)\Big).\end{aligned} \tag{5.27}$$

With the pre-SN mass ratio $\nu_0 = m_3/M_{t,0}$, the pre-SN velocities of the cm and the tertiary in the CM reference frame are

$$\mathbf{v_{cm,0}} = \nu_0\Big(V_{0x}, V_{0y}, V_{0z}\Big) \tag{5.28}$$

$$\mathbf{v_3} = (\nu_0 - 1)\Big(V_{0x}, V_{0y}, V_{0z}\Big). \tag{5.29}$$

We calculate the instantaneous velocity of the cm after the SN (as before, because of the assumption of an instantaneous SN, the velocity of the tertiary after the SN remains unchanged):

$$\mathbf{v_{cm}} = \nu_0\Big(V_{0x} + \frac{v_{sys,x}}{\nu_0}, V_{0y} + \frac{v_{sys,y}}{\nu_0}, V_{0z} + \frac{v_{sys,z}}{\nu_0}\Big). \tag{5.30}$$

Using the post-SN mass ratio $\nu = m_3/M_t$, the systemic velocity of the outer binary (and therefore of the triple) is

$$\begin{aligned}\mathbf{V_{sys}} &= (1-\nu)\mathbf{v_{cm}} + \nu\mathbf{v_3} \\ &= (1-\nu)\Big(\frac{\nu_0-\nu}{1-\nu}V_{0x} + (\mu_0-\mu)v_{0x} + (1-\mu)v_{kx}, \\ &\quad \frac{\nu_0-\nu}{1-\nu}V_{0y} + (\mu_0-\mu)v_{0y} + (1-\mu)v_{ky}, \\ &\quad \frac{\nu_0-\nu}{1-\nu}V_{0z} + (1-\mu)v_{kz}\Big).\end{aligned} \tag{5.31}$$

Summarizing, one can consider a hierarchical triple system as a effective binary system composed of an effective star (i.e. the inner binary center of mass (cm)) and the tertiary. The effective star undergoes an effective asymmetric SN resulting in three effects: 1) sudden mass loss Δm, 2) an instantaneous translation $\mathbf{\Delta R}$, and 3) a random kick velocity $\mathbf{v_{sys}}$. The calculation of the post-SN parameters and velocities of a hierarchical triple system is now reduced to the prescription for a SN in a binary as presented in section 5.2.1. Note that the mass loss does not occur from the position of the effective star, but from the position of the primary star; a clear distinction from a physical binary system. However, from what position the mass loss occurs is not important when an instantaneous SN is considered. When the effect of the shell impact on the companion star(s) is considered, this off-center mass loss must be taken into account. In addition, if it was not the primary which underwent the SN, but for example the tertiary, the computation would be done by *reducing* the inner binary to an effective star, as shown in this section. One would again have a binary configuration to calculate the effect of the SN; in such a system there is no off-center mass loss. In section 5.2.4 we show how one can reduce any hierarchical multiple star system to an effective binary in a recursive way using the effective binary method and in § 5.2.4 we do the computation of the effect of a SN on a binary-binary system.

Dissociating hierarchical triple systems

For the triple system, dissociation can occur in two ways: the inner binary can dissociate ($a < 0$ and $e > 1$ or $a \to \infty$ and $e = 1$) (see section 5.2.1) and the outer binary can dissociate ($A < 0$ and $E > 1$ or $A \to \infty$ and $E = 1$), i.e. the inner binary and the tertiary become unbound. The inner binary dissociation scenario generally results in complete dissociation of the system. However, hypothetical scenarios exist in which one of the inner binary components is ejected towards the tertiary star to either collapse with it or to form a binary by gravitational or tidal capture. Nevertheless, these scenarios have a small probability since the ejection conditions (e.g. the solid angle in which that particular inner binary component has to be ejected in) and the capture conditions are extremely specific. From equation 5.26 we see that for the inner binary to dissociate from the tertiary, the angle Φ has to satisfy

$$\cos\Phi \quad \geqslant \quad \Big(1 - \frac{2A_0}{R}\frac{\Delta m}{M_{t,0}} - \frac{v_{sys}^2}{V_{c,0}^2} + 2A_0\rho\Big)\Big(2\frac{V_0}{V_{c,0}}\frac{v_{sys}}{V_{c,0}}\Big)^{-1}. \tag{5.32}$$

The probability of this type of dissociation is

$$P_{diss}^{outer} = \frac{1}{2}\Big(1 - \Big(1 - \frac{2A_0}{R}\frac{\Delta m}{M_{t,0}} - \frac{v_{sys}^2}{V_{c,0}^2} + 2A_0\rho\Big) \times \Big(2\frac{V_0}{V_{c,0}}\frac{v_{sys}}{V_{c,0}}\Big)^{-1}\Big). \quad (5.33)$$

In the case of the dissociation of the outer binary, using the following short hand relations

$$\begin{aligned}
\tilde{M} &= \frac{M_t}{M_{t,0}} \\
J &= \frac{V_{0x}^2}{V_0^2} - 2\tilde{M}\frac{A_0}{2A_0 - R_0}\frac{R_0}{R} + \frac{v_{sys}^2}{V_0^2} + \frac{2V_{0x}v_{sys,x}}{V_0^2} \\
K &= 1 + \frac{J}{\tilde{M}}\frac{2A_0 - R_0}{A_0}\frac{R}{R_0} - \frac{v_{sys,y}^2}{\tilde{M}V_0^2}\frac{2A_0 - R}{A_0}\frac{R}{R_0} \\
L &= \frac{1}{\nu}\Big(\frac{\sqrt{J}}{\tilde{M}V_0}v_{sys,y}\frac{2A_0 - R_0}{A_0}\frac{R}{R_0} \\
&\quad - \frac{J}{\tilde{M}}\frac{2A_0 - R_0}{A_0}\frac{R}{R_0} - 1\Big) \\
N &= \frac{1}{\nu}\Big(1 + \frac{J}{\tilde{M}}\frac{2A_0 - R_0}{A_0}\frac{R}{R_0}(K+1)\Big)
\end{aligned}$$

the runaway velocities of the inner binary system and the tertiary are (following and generalizing Tauris and Takens (1998)):

$$\begin{aligned}
\mathbf{v_{cm,diss}} &= \Big(v_{sys,x}\Big(\frac{1}{L} + 1\Big) + \Big(\frac{1}{L} + \nu_0\Big)V_{0x}, v_{sys,y}\Big(1 - \frac{1}{N}\Big) \\
&\quad + \nu_0 V_{0y} + \frac{K\sqrt{J}}{N}V_0, v_{sys,z}\Big(\frac{1}{L} + 1\Big)\Big) \quad (5.34) \\
\mathbf{v_{3,diss}} &= \Big(-\frac{Mv_{sys,x}}{m_3 L} - \Big(\frac{M}{m_3 L} + 1 - \nu_0\Big)V_{0x}, (\nu_0 - 1)V_{0y} \\
&\quad + \frac{Mv_{sys,y}}{m_3 N} - \frac{MK\sqrt{J}}{m_3 N}V_0, -\frac{Mv_{sys,z}}{m_3 L}\Big). \quad (5.35)
\end{aligned}$$

Note that these equations are more general than the ones in section 5.2.1, because we cannot assume $\mathbf{R} = \mathbf{R_0}$ in the triple case.

5.2.3 An example of the effect of a supernova in a hierarchical triple

For two simple sets of initial conditions we investigated the effect of mass loss, Δm, and kick velocity, $\mathbf{v_k}$, on the survivability of a triple system. We distinguish

between four different post-SN scenarios: (1) the triple survives as a whole ($e < 1$ and $E < 1$) with new orbital parameters, (2) the inner binary survives and the third star escapes ($e < 1$ and $E > 1$), (3) the inner binary dissociates and the outer binary survives ($e > 1$ and $E < 1$) and (4) the triple completely dissociates ($e > 1$ and $E > 1$). The third scenario is a rather special case and can only be of temporary nature: in this scenario, even though the inner binary has just dissociated, the third star remains bound to the inner binary center of mass. This is a temporal solution which eventually will lead to the full dissociation of the triple, except in the extreme case in which the tertiary star captures one of the ejected inner stars to form a new binary system.

For each set of initial conditions we used a hierarchical triple system with primary, secondary and tertiary stars of masses $m_{1,0}$, m_2, m_3 = 3, 2, 1 $M_\odot$ respectively and inner and outer binary semi-major axes a_0, A_0 = 10, 50 $R_\odot$ respectively, and we varied the kick velocity direction $\hat{\mathbf{v}}_\mathbf{k}$. For the two different sets of initial conditions we determine for what combinations of Δm and v_k which post-SN scenario occurs and we show our results in Figure 5.3; the used initial conditions are specified below the respective figures.

In Figure 5.3a. we used a circular inner and outer orbit, not inclined with respect to each other, with all stars on one line and the kick velocity in the same direction as the pre-SN inner binary relative velocity. We see that for zero kick velocity, the inner binary dissociates for a mass loss ratio of $\Delta m/M_0 = 0.5$, which is consistent with earlier work (e.g. Hills 1983). For zero mass loss, we see that the inner binary dissociates for a kick velocity of $\mathbf{v_k} \sim 128$ km/s - this velocity is exactly the difference between the inner binary escape velocity ($v_{esc} = \sqrt{2GM_0/a_0} \sim 437$ km/s) and pre-SN relative velocity ($v_0 = \sqrt{GM_0/a_0} \sim 309$ km/s) - but that the third star escapes for a slightly lower value of the kick velocity. This is because the inner binary systemic velocity (which is the effective outer orbit kick; see Section 5.2.2) plus the pre-SN outer orbit relative velocity already exceed the outer orbit escape velocity. We furthermore see that the total triple survival scenario allows lower kick velocities for higher mass losses. Above a kick velocity of $\mathbf{v_k} \sim 128$ km/s the inner binary always dissociates, irrespective of the mass loss, (eventually) leading to total dissociation.

In Figure 5.3b. we keep the same configuration as described for Figure 5.3a., but with a kick velocity in the opposite direction with respect to the orbital velocity of the exploding star before the supernova. The triple can now lose more mass and receive a higher velocity kick while stil surviving. The ability to sustain greater kick velocities is explained by the fact that, depending on the mass loss, the kick velocity now has to exceed a fraction of the sum of v_0 and v_k (for zero mass loss v_0+$v_k$$\sim$ 746 km/s) due to the opposing directions of the two velocities. We also see that total triple survival can occur beyond a mass loss ratio of 0.5, because the kick velocity can oppose the dissociating effect

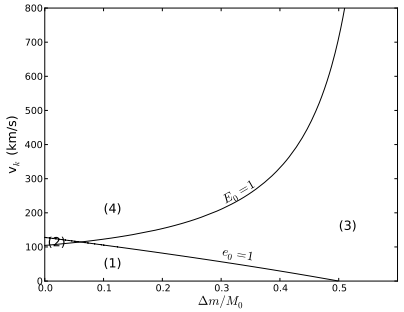
of the mass loss (as mentioned in Hills 1983). Bare in mind that while the $\Delta m/M_0 = 0$ case is non-physical we include it for the completeness" sake.

In Figure 5.4 we show how the post-SN systemic velocity of the triple depends on the mass loss Δm for a hierarchical triple system with primary, secondary and tertiary stars with masses ($m_{1,0}$, m_2, m_3) = (3, 2, 1) $M_\odot$, inner and outer binary semi-major axes (a_0, A_0) = (10, 50) $R_\odot$ and the kick velocity in the direction of the pre-SN inner orbit relative velocity. We plot our results for the case that the SN went off at the inner orbit apastron ($\theta_0 = 180$ degrees) or at the inner orbit periastron ($\theta_0 = 0$ degrees) for a symmetric SN (i.e. $v_k = 0$ km/s) and a SN with a kick $v_k \sim 31$ km/s, in the cm reference frame (i.e. with the cm at rest at $t = 0$). In Figure 5.4a. we see that for a symmetric supernova, the systemic velocity of the inner binary increases with the amount of mass loss, which is an intuitive result. We see that even with zero mass loss the triple has a systemic velocity, namely the velocity it started with in this reference frame ($V_{sys} \sim 17.5$ km/s). We furthermore see that the increase of the triple systemic velocity happens more steeply for these cases where the SN goes off at periastron - with the steepest curve for the highest inner binary eccentricity - than when the supernova goes off at apastron - with the steepest curve is for lowest eccentricity. For an asymmetric supernova with kick $v_k \sim 31$ km/s, see Figure 5.4b., we observe similar behaviour, but with the difference of the zero mass loss case: in this case the triple system has a lower velocity than it started with ($V_{sys} \sim 2.5$ km/s), which is due to the kick. This result is dependent on the direction of the kick.
The pre-SN triple systemic velocity is dependent on both the inner binary and the outer binary. Its dependence on the inner binary is via the masses $m_{1,0}$ and m_2 of the primary and secondary respectively and the inner binary orbital parameters which fully constrain the relative velocity of these stars (see equation (5.5)). Its dependence on the outer binary is via the mass m_3 of the tertiary and the outer orbit orbital parameters which fully constrain the outer binary relative velocity (see equation (5.21)). The post-SN triple systemic velocity is merely the sum of the pre-SN systemic velocity and its change, which is only due to the inner binary through the mass loss Δm and kick velocity $\mathbf{v_k}$.

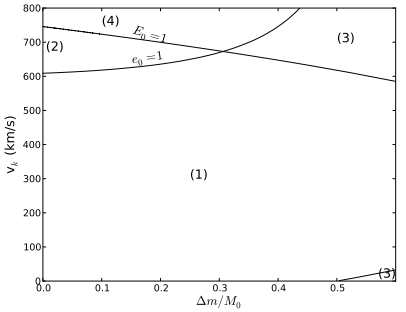
5.2.4 Hierarchical systems of multiplicity > 3

There exist two kind of hierarchical multiple star systems with more than three stars:

1. systems that have n stars and hierarchy $n - 1$, i.e. multiple star systems with its stars hierarchically ordered in series (hereafter serial systems). Examples of such systems include quadruples with hierarchy 3, but also binaries and triples are serial systems.

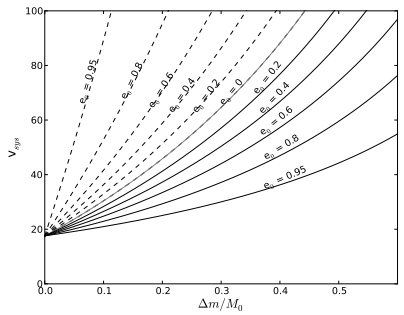


(a) $e_0 = 0$, $E_0 = 0$, $\theta_0 = 0°$, $\Theta_0 = 0°$, $i_0 = 0$, $\alpha_0 = 0°$, $\mathbf{v_k}$ = (1,0,0)



(b) $e_0 = 0$, $E_0 = 0$, $\theta_0 = 0°$, $\Theta_0 = 0°$, $i_0 = 0$, $\alpha_0 = 0°$, $\mathbf{v_k}$ = (-1,0,0)

Figure 5.3: The plots above show the survivability of the hierarchical triple system for varying mass loss Δm and kick velocity v_k. The systems have masses of $m_{1,0}$, m_2, m_3 = 3, 2, 1 $M_\odot$ respectively and inner and outer binary semi-major axes a_0, A_0 = 10, 50 $R_\odot$ respectively. There are four possible post-SN scenarios: (1) the whole triple survives, (2) the inner binary survives but the third star escapes, (3) the inner binary dissociates and the outer binary survives, or (4) the triple completely dissociates. The areas in the plots are labeled according to their respective post-SN scenario.



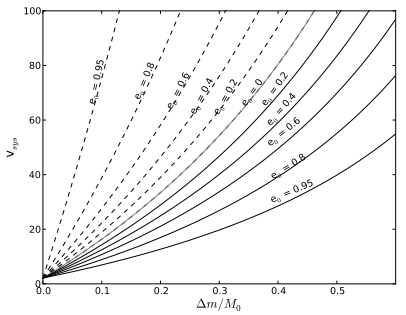


Figure 5.4: The dependence of the post-SN systemic velocity of the triple as a function of mass loss Δm. We present the results for the case in which the SN occurs at the moment that the exploding star is at the apastron of the inner binary ($\theta_0 = 0$, dashes) and apastron ($\theta_0 = 180$ degrees, solid curves) for a range of pre-SN inner binary eccentricities. We show this dependency for two cases: $v_k = 0$ km/s in the left panel, and for a kick of $v_k \sim 31$ in the right panel km/s.

2. systems that have n stars and hierarchy $n-2$ or below, i.e. multiples composed of serial systems which are hierarchically ordered in parallel (hereafter parallel systems). An example of such system is a quadruple with hierarchy 2 (i.e. a binary-binary system).

Serial systems

The effect of a SN on a serial system is calculated by applying the effective binary method (see section 5.2.2) by recursively replacing the inner binary by an effective star at the center of mass of that binary, until the total system is reduced to a single effective binary. When considering a serial system of n stars each with mass, position and velocity given by ($m_{1,0}$,$\mathbf{r_1}$,$\mathbf{v_{1,0}}$), (m_2,$\mathbf{r_2}$,$\mathbf{v_2}$), ... , (m_n,$\mathbf{r_n}$,$\mathbf{v_n}$) respectively, in which the primary star undergoes a SN, one starts by reducing the inner binary to an effective star, as was done in section 5.2.2. The inner binary consists of the primary and secondary star at positions $\mathbf{r_1}$ and $\mathbf{r_2}$ respectively. This binary is reduced to an effective star of mass $m_{cm,0} = m_{1,0} + m_2$ at position $\mathbf{r_{cm,0}}$ given by equation (5.17) and having velocity $\mathbf{v_{cm,0}}$ given by equation (5.18). Due to the SN of the primary this effective star experiences a mass loss Δm, an instantaneous translation $\mathbf{\Delta R}$ given by equation (5.19), and a random kick velocity $\mathbf{v_{sys}}$ given by equation (5.12). After applying these effects on this effective binary, one can calculate the post-SN orbital parameters and velocities and the systemic velocity $\mathbf{v_{sys}^{(2)}} = \mathbf{V_{sys}}$ of this effective binary, given by equation (5.31), using the prescription for a SN in a binary.[3] The total system is now reduced to a serial system of $n-1$ objects (real and effective stars).

Subsequently, one reduces the current inner binary - consisting of the effective and tertiary star at positions $\mathbf{r_{cm,0}}$ and $\mathbf{r_3}$ respectively - to an effective star of mass $m_{cm,0}^{(2)} = m_{cm,0} + m_3$, at position

$$\mathbf{r_{cm,0}^{(2)}} = \frac{m_{cm,0}\mathbf{r_{cm,0}} + m_3\mathbf{r_3}}{m_{cm,0} + m_3} \tag{5.36}$$

with a velocity

$$\mathbf{v_{cm,0}^{(2)}} = \frac{m_{cm,0}\mathbf{v_{cm,0}} + m_3\mathbf{v_3}}{m_{cm,0} + m_3}. \tag{5.37}$$

Due to the SN of the primary star, this effective star also experiences a mass loss Δm, an instantaneous translation $\mathbf{\Delta R^{(2)}}$ - this time, the translation vector has non-zero y- and z-components - and a random kick velocity $\mathbf{v_{sys}^{(2)}}$. After applying these effects on this effective binary, one can calculate the post-SN orbital parameters and velocities and the systemic velocity $\mathbf{v_{sys}^{(3)}}$ of this effective

[3] The number between parentheses denotes the hierarchy up to which the system has been reduced to a effective star.

binary using the prescription for a SN in a binary. The total system is now reduced to a serial system of $n-2$ objects (real and effective stars).

This procedure is carried on until the entire multiple is reduced to a single effective binary, consisting of the nth star at position $\mathbf{r_n}$ and a effective star of mass $m_{cm,0}^{(n-2)} = m_{cm,0}^{(n-3)} + m_{n-1}$ at position

$$\mathbf{r_{cm,0}^{(n-2)}} = \frac{m_{cm,0}^{(n-3)}\mathbf{r_{cm,0}^{(n-3)}} + m_{n-1}\mathbf{r_{n-1}}}{m_{cm,0}^{(n-3)} + m_{n-1}} \tag{5.38}$$

with a velocity

$$\mathbf{v_{cm,0}^{(n-2)}} = \frac{m_{cm,0}^{(n-3)}\mathbf{v_{cm,0}^{(n-3)}} + m_{n-1}\mathbf{v_{n-1}}}{m_{cm,0}^{(n-3)} + m_{n-1}}. \tag{5.39}$$

This effective star also experiences mass loss Δm, an instantaneous translation $\mathbf{\Delta R^{(n-2)}}$ and a random kick velocity $\mathbf{v_{sys}^{(n-2)}}$. After applying these effects on this (final) effective binary, one can calculate the post-SN orbital parameters and velocities and the systemic velocity $\mathbf{v_{sys}^{(n-1)}}$ for this effective binary (and therefore of the total system) using the binary method.

When it is not the primary star which undergoes a SN, but the mth star in the hierarchy, the procedure is carried out by first reducing the inner serial system of $m-1$ stars to an effective star at its center of mass. One can then apply the above explained method, as there is no computational difference in whether the primary or the secondary of a(n effective) binary undergoes the SN.

Parallel systems

The effect of a SN on a parallel system is calculated by reducing each parallel branch (which itself is a serial system) to an effective star until an effective serial configuration is reached; after this, one can use the method explained in the previous section. We consider a parallel system of i parallel branches, each consisting of an arbitrary number n_i of stars with mass, position and velocity given by (m_1,$\mathbf{r_1}$,$\mathbf{v_1}$), ... , (m_{n_i},$\mathbf{r_{n_i}}$,$\mathbf{v_{n_i}}$) respectively, in which the mth star - which is part of branch j - undergoes a SN. One starts by reducing all $i-1$ branches $\neq j$ to effective stars. One then calculates the effect of the SN on branch j (i.e. systemic velocity and mass loss) using the method described in section 5.2.4. The total system is now reduced to an effective serial system of i effective stars in which the jth effective star undergoes an effective SN with the systemic velocity of branch j as the kick velocity. The effect of this effective SN on the total system, can be calculated by applying the method described in section 5.2.4 to this effective serial system. As an example we will now demonstrate the effect of a SN on a binary-binary system.

An example of the effect of a supernova in binary-binary system

We consider a hierarchical binary-binary system of stars with mass, position and velocity given by ($m_{1,0}$,$\mathbf{r_1}$,$\mathbf{v_{1,0}}$), (m_2,$\mathbf{r_2}$,$\mathbf{v_2}$), (m_3,$\mathbf{r_3}$,$\mathbf{v_3}$) and (m_4,$\mathbf{r_4}$,$\mathbf{v_4}$) respectively, in which the primary star undergoes a SN. The binary consisting of the primary and the secondary star (primary binary) has the configuration and the parameters as in section 5.2.1 and has a center of mass (cm_1, i.e. effective star 1) of mass $m_{cm1,0} = m_{1,0}+m_2 = M_0$ at position given by equation (5.17) with a velocity $\mathbf{v_{cm1,0}}$ given by equation (5.18). The secondary binary consists of the tertiary and quaternary star and its center of mass (cm_2, i.e. effective star 2) has a mass $m_{cm2} = m_3 + m_4 = M_2$, is at position

$$\mathbf{r_{cm2}} = (1-\kappa)\mathbf{r_3} + \kappa\mathbf{r_4}$$

and has velocity

$$\mathbf{v_{cm2}} = (1-\kappa)\mathbf{v_3} + \kappa\mathbf{v_4},$$

before the SN, where $\kappa = \frac{m_4}{M_2}$. The cm_1 and cm_2 constitute an effective binary defined by semi-major axis, A_0, eccentricity, E_0, and true anomaly, Θ_0. The separation distance is denoted by $\mathbf{R}_0$. Before the SN the effective binary orbital plane has inclination i_0 with respect to the primary binary orbital plane and the separation distance of the effective binary projected onto the xy-plane makes an angle α_0 with the separation distance of the primary binary. We assume an instantaneous SN[4]. In the effective SN the cm_1 experiences a mass loss Δm, an instantaneous translation $\mathbf{\Delta R}$ along the x-axis given by equation (5.19) and a random kick velocity $\mathbf{v_{sys}}$ given by equation (5.12). The orbital parameters change as a result of the SN: the primary binary parameters change according to the description in section 5.2.1 and the effective binary orbital parameters change to semi-major axis A, eccentricity E and true anomaly Θ; the secondary binary orbital parameters do not change when SN-shell impact is not taken into account. Before the SN the binary-binary system has a total mass $M_{bb,0} = m_{cm1,0} + m_{cm2}$, we use the cm_1 coordinate system to pin down the primary binary and add to this coordinate system the tertiary and quaternary at a position such that $R_0 \gg r_0$, and we choose a reference frame in which the center of mass of the total binary-binary system (CM_{bb}) is at rest (the CM_{bb} reference frame) and in which the cm_1 is at the origin at $t = 0$. The separation distance between the cm_1 and the cm_2, $\mathbf{R_0}$, is given by equation (5.20) and the velocity of the cm_1 relative to the cm_2 is

$$\mathbf{V_0} = \mathbf{v_{cm1,0}} - \mathbf{v_{cm2}} = (V_{0x}, V_{0y}, V_{0z}) \tag{5.40}$$

[4]See section 5.2.1 and note that these statements about the inner companion (secondary) star also hold for the outer companion (tertiary and quaternary) stars.

prior to the SN. The effective kick velocity $\mathbf{v_{sys}}$ makes an angle Φ with the pre-SN relative velocity $\mathbf{V_0}$. After the SN the separation distance between the cm_1 and the cm_2 is $\mathbf{R}$ given by equation (5.22) and the velocity of the cm_1 relative to the cm_2 is $\mathbf{V}$ given by equation (5.23), the cm_1 mass $m_{cm1} = m_{cm1,0} - \Delta m = M$ and total binary-binary mass $M_{bb} = m_{cm1} + m_{cm2} = M + M_2$. Applying the relations above and equations (5.1) and (5.2) to our binary-binary system, we obtain relations for the post-SN semi-major axis A and eccentricity E in terms of both the pre- and post-SN orbital parameters and velocities given by equations (5.26) and (5.27) respectively with $M_{t,0}$ replaced by $M_{bb,0}$. To compute the systemic velocity due to the SN, we express the pre-SN velocities of the cm_1 and the cm_2 in the CM_{bb} reference frame. Using the pre-SN mass ratio $\lambda_0 = \frac{m_{cm2}}{M_{bb,0}}$, the pre-SN velocities are given by

$$\mathbf{v_{cm1,0}} = \lambda_0 \Big(V_{0x}, V_{0y}, V_{0z} \Big) \tag{5.41}$$

$$\mathbf{v_{cm2}} = (\lambda_0 - 1) \Big(V_{0x}, V_{0y}, V_{0z} \Big). \tag{5.42}$$

We calculate the instantaneous velocity of the cm_1 after the SN (due to the assumption of an instantaneous SN, the velocity of the cm_2 after the SN remains unchanged):

$$\mathbf{v_{cm1}} = \lambda_0 \Big(V_{0x} + \frac{v_{sys,x}}{\lambda_0}, V_{0y} + \frac{v_{sys,y}}{\lambda_0}, V_{0z} + \frac{v_{sys,z}}{\lambda_0} \Big) \tag{5.43}$$

With the post-SN mass ratio $\lambda = \frac{m_{cm2}}{M_{bb}}$, the systemic velocity of the effective binary (and therefore of the binary-binary system) is

$$\begin{aligned} \mathbf{V_{sys}} &= (1-\lambda)\mathbf{v_{cm1}} + \lambda \mathbf{v_{cm2}} \\ &= (1-\lambda) \Big(\frac{\lambda_0 - \lambda}{1-\lambda} V_{0x} + (\mu_0 - \mu) v_{0x} + (1-\mu) v_{kx}, \\ &\quad \frac{\lambda_0 - \lambda}{1-\lambda} V_{0y} + (\mu_0 - \mu) v_{0y} + (1-\mu) v_{ky}, \\ &\quad \frac{\lambda_0 - \lambda}{1-\lambda} V_{0z} + (1-\mu) v_{kz} \Big). \end{aligned} \tag{5.44}$$

Note that because the branch harboring the SN-progenitor (SN branch) is a binary, this calculation the SN-effect on the binary-binary system is almost identical to calculation of the SN-effect on a hierarchical triple. The computations become more interesting for systems with a SN branch of higher multiplicity.

5.3 Application: Formation of J1903+0327

PSR J1903+0327 was observed by Champion et al. (2008) who determined it to be a millisecond pulsar (MSP). This MSP is observed to have a 1 $M_\odot$ main

sequence companion with a highly eccentric and distant orbit ($e \simeq 0.44$, orbital period $\simeq 95.2$ days). These properties are atypical for MSPs because MSPs are expected to be spun-up via mass transfer (Bhattacharya and van den Heuvel 1991), which in turn widens and circularizes the orbit, while its companion evolves through a giant phase. Phinney (1992), for example, suggest an eccentricity $e < 10^{-3}$ is typical for MSP binaries. The exception to this has been MSPs in globular clusters which have interactions with other objects that may perturb the orbit of the binary. However, Freire et al. (2011) find it to be unlikely that this MSP system has its origin in an exchange interaction in such a dense stellar environment.

It has been suggested that J1903+0327 maybe the result of a hierarchical triple (Champion et al. 2008, Portegies Zwart et al. 2011 and Bejger et al. 2011) where the inner companion has been lost after spinning-up the MSP, leaving only the MSP and the former tertiary to be observed. Should J1903+0327 be the result of such a system the methods in the previous sections provide a strong beginning to investigate how such a system might evolve.

5.3.1 Initial conditions

We generate sets of 10^5 initial conditions, as described below, with each set constituting a stable triple system, and then simulated the effect of an instantaneous SN occurring at the primary star. The model we follow (many of our initial conditions are drawn from Portegies Zwart et al. (2011)) consist of a primary, secondary and tertiary star with zero age masses of 10 $M_\odot$, 1 $M_\odot$ and 0.9 $M_\odot$ respectively. The initial conditions are generated by selecting the semi-major axis, A_0, eccentricity, E_0, and the orbital inclination, i, for the tertiary. A_0 takes values on the range [200, 10 000]$R_\odot$ from a flat distribution, E_0 is chosen on the range [0, 1) from a distribution that is flat in log space, and i_0 is chosen on the range [0, π] with a sinusoidal distribution. Combining these values with the zero age masses of the stars as well as a pre-set value for the initial semi-major axis of the inner binary, $a_0 = 200 R_\odot$ we then test for stability of the system using:

$$\begin{aligned} \frac{A_0(1-E_0)}{a_0} &> 3\Big(1+\frac{m_3}{M_0}\Big)^{1/3}\Big(\frac{7}{4}+\frac{1}{2}\cos i_0 - \cos^2 i_0\Big)^{1/3} \\ &\times (1-E_0)^{-1/6} \end{aligned} \tag{5.45}$$

(Zhuchkov et al. 2010). If the system is stable with this set of parameters, we choose the remaining parameters, namely the angle α_0 described in the previous sections, the direction and magnitude of the kick. Because we have assured that the system is dynamically stable before starting our simulations our assumption of a hierarchical system is guaranteed. We observe that due to the SN kick, systems with very high inclination are preferentially removed or their

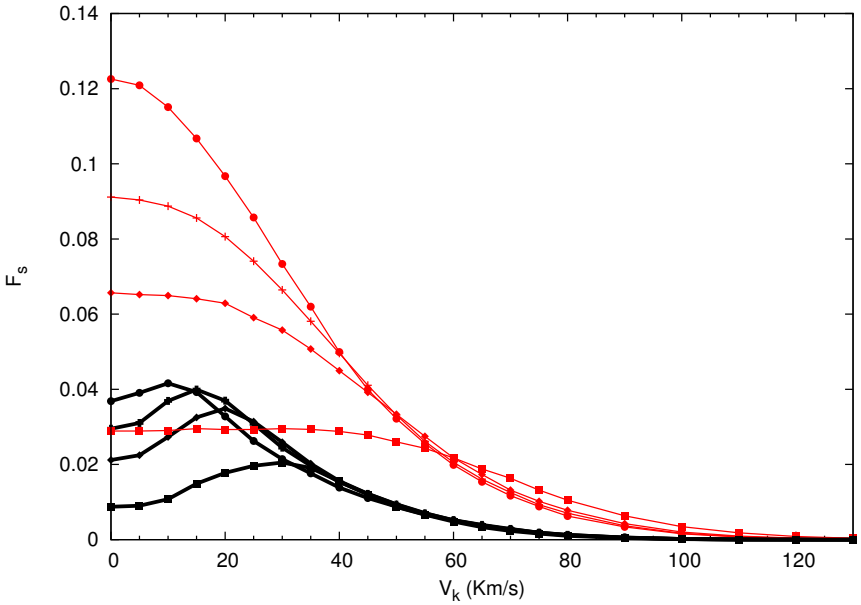


Figure 5.5: The fraction of surviving and stable system (thin red and thick black (colors online only) lines respectively) as a function of the kick velocity. The lines in each set correspond to different semi-major axis, 50, 30, 20, and 10 $R_\odot$ (circle, cross, diamond, and square respectively). All curves are normalized to the total number of surviving systems with a semi-major axis of 50 $R_\odot$.

inclination is reduced thus as a result we do not include the effects of Kozai iterations.

5.3.2 Simulations

The inner binary undergoes a common envelope (CE) phase, circularizing the orbit, reducing the inner semi-major axis to a value between 5 $R_\odot$ and 60 $R_\odot$, and reducing the mass of the primary to 2.7 $M_\odot$. The effect of these changes on the stability of the system can immediately be seen in equation (5.45). Then, due to the SN, the primary undergoes a mass loss of 1.3 $M_\odot$ and receives a corresponding kick. The velocity of the kick is fixed between 5 and 160 km/s for each set of simulations and the kick direction is randomly chosen such that for all simulations the direction is isotropic. We then analyze the survivability and stability of each system. A system survives the SN and resulting kick if it remains bound, and it is determined to be stable if, while remaining bound, the system also satisfies the stability criterion in equation (5.45).

We ran Monte Carlo simulations for four different inner binary semi-major axes (10, 20, 30, and 50 $R_\odot$). For each semi-major axis value we run 25 simula-

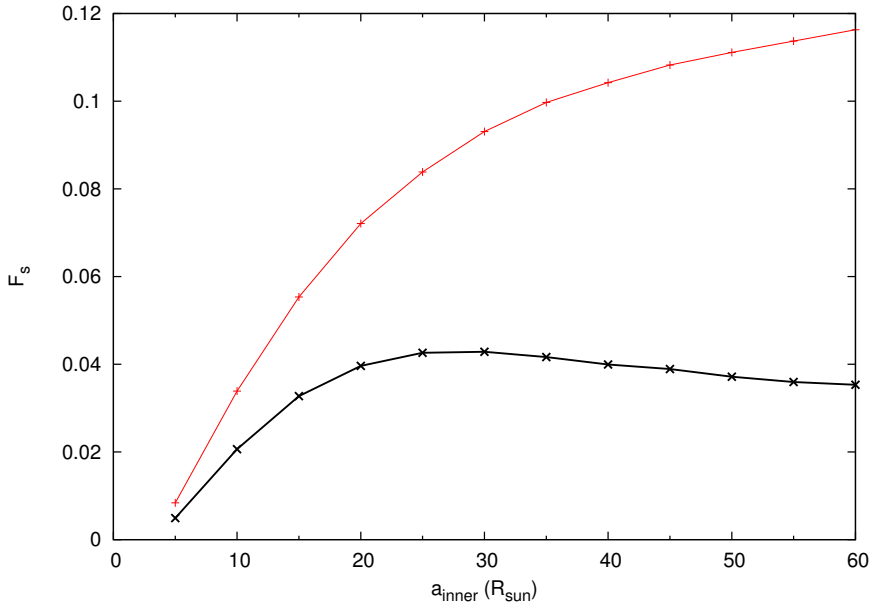


Figure 5.6: The fraction of surviving and stable systems (upper and lower lines respectively) with respect to the inner semi-major axis. A constant kick velocity of 20 km/s is used.

tions (each of the 25 simulations consists of 10^5 sets of initial conditions) each with a constraint kick velocity (between 0 and 130 km/s). In Figure 5.5 we plot the kick velocity versus the fraction of surviving and stable systems. For each pair of curves the thin red upper curve corresponds to the survivability fraction and the thick black lower curve to the fraction that survives and remains stable. Curves with same kick velocity have the same point-symbols. Each point represents the fraction of surviving or stable systems normalized to the total number of surviving systems with a semi-major axis of $50R_{\odot}$. Increasing the semi-major axis from 10 to 30 $R_{\odot}$ strongly increases the overall probability of a system to survive and remain stable. However, with a kick velocity of 45 km/s and higher the probability of a system remaining stable is nearly the same when the semi-major axis is $\geqslant 20R_{\odot}$. Figure 5.5 shows the effect of the Blaauw & Boersma recoil (Blaauw 1961 & Boersma (1961)) on the system when the SN kick is small; as the SN kick velocity approaches the Blaauw & Boersma recoil velocity the stability increases due to the kick and recoil off-setting one another, in part or in full. As the SN kick velocity increases it begins to overwhelm the Blaauw & Boersma effect.

In Figure 5.6 we show the effect the inner semi-major axis has on survivability and stability (the upper and lower lines respectively) using a constant

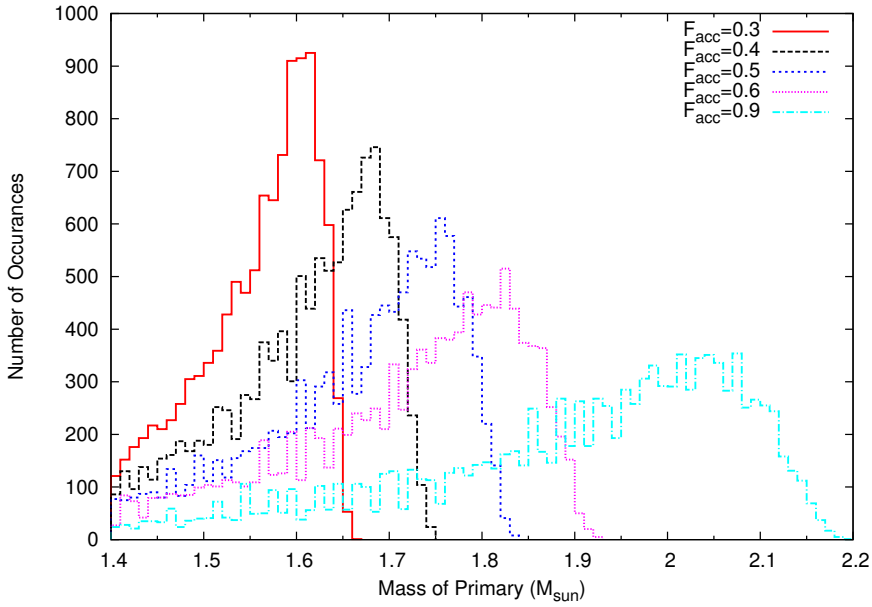


Figure 5.7: The number of occurrences for which the system becomes unstable due to mass transfer at a given mass of the primary. The curves corresponds to F_{acc} values of 0.3, 0.4, 0.5, 0.6, and 0.9 as shown in the key. The peak value and FWHM for each curve in this figure, as well as similar curves for other values of F_{acc}, are plotted in Figure 5.8.

kick velocity of 20 km/s. Again each data point represents the fraction of systems that survive or survive and in addition remains stable out of a set of 10^5 initial conditions. Here we see the significant role of the inner semi-major axis on the survivability of the system. If we note for a particular kick velocity which value of a_0 the stability fraction begins to level, we can see a corresponds to the merging of the stability curves in Figure 5.5. For the case of a 20 km/s SN kick velocity, as in Figure 5.6, we see that any value of a_0 greater than about 30 $R_\odot$ will have similar stability fractions while systems with lower values of a_0 should have a lower stability fraction as we see in Figure 5.5.

Next, we chose all of the systems that remain stable after the SN and subject them to a mass transfer phase. Here we iteratively remove one one-hundredth of the mass of the secondary and transfer a fraction of it to the primary, which after the SN would have formed a neutron star (NS). Following the work of Pols and Marinus (1994) we find:

$$a_f = a_i \left[\left(\frac{m_{1,f}}{m_{1_i}} \right)^{(1/(1-\chi))} \frac{m_{2,f}}{m_{2_i}} \right]^{-2} \times \left(\frac{M_i}{M_f} \right) \tag{5.46}$$

where a_f is the new semi-major axis, a_i is the semi-major axis before the mass transfer, $m_{1,i}$ and $m_{2,i}$ are the masses of the primary and secondary before the

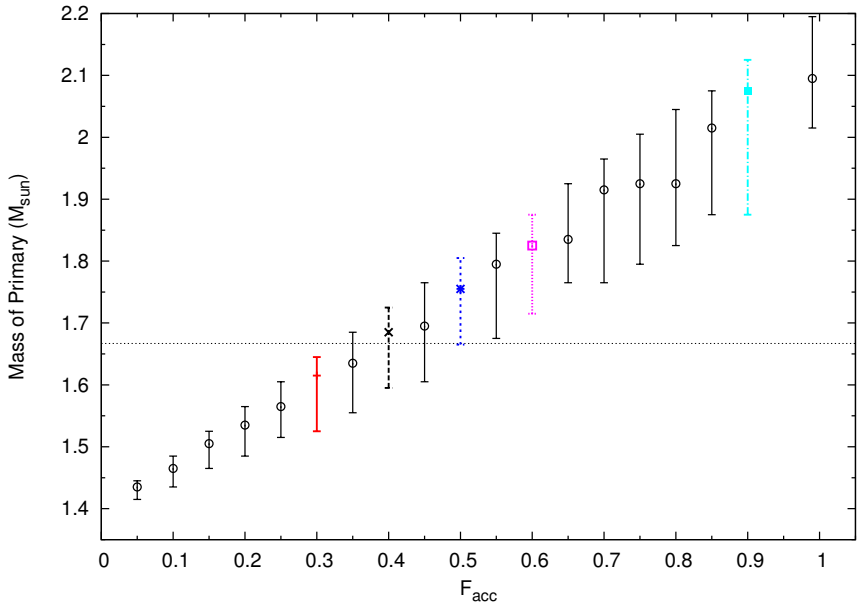


Figure 5.8: The final mass of primaries with respect to the fraction of accreted mass. The dashed horizontal line is placed at the observed mass of J1903+0327. The points represent the peak value of curves which plot the number of times a system becomes unstable while at a given mass of the primary (like those in Figure 5.7); the upper and lower bars represent the FWHM of the curves. The values that are colored (online) and that have different line types correspond to the curves in Figure 5.7 (e.g. the blue, dot-dash line at F_{acc}=0.9 is obtained from the right most peaked curve in Figure 5.7, which is also a blue, dot-dash line).

mass transfer and $m_{1,f}$ and $m_{2,f}$ are the masses of the primary and secondary after the mass transfer, M_i and M_f are the total masses of the binary before and after the mass transfer, and finally χ is the ratio of the change in mass of the system to the change in mass of the donor (i.e. the secondary). If we define the fraction of mass accreted, F_{acc}, as the fraction of mass lost from the secondary which is accreted onto the primary we find that the $1/(1-\chi)$ term simply becomes $1/F_{acc}$. After each iterative mass transfer, and the resulting change in the semi-major axis, we test the triple for stability using equation (5.45). When the system becomes dynamically unstable we stop simulating as the assumption of a hierarchical system has broken down. We record the mass of the primary when the system becomes dynamically unstable and plot the mass in Figure 5.7 versus the number of times systems becomes unstable at that mass. For this plot we used F_{acc} values of 0.3, 0.4, 0.5, 0.6 and 0.9, which correspond to the lines which peak from the left to right respectively, and a constant kick velocity. We see that the peak value for each F_{acc} shifts to a larger primary

mass as F_{acc} increases. This relation is expected since as F_{acc} becomes larger more of the mass lost from the secondary is accreted onto the primary. So for the case of $F_{acc} = 0.3$ only 30% of the mass lost from the secondary could ever accrete onto the primary thereby reducing the maximum possible mass of the primary. If we assumed that all of the mass of the secondary is lost (an unphysical case since the mass transfer would end before this could happen, but this provides an extreme upper limit) then while the secondary would have lost $1M_{\odot}$ the primary would have only accreted $0.3M_{\odot}$ resulting in a maximum primary mass of 1.7 $M_{\odot}$. If we were to assume that mass transfer would stop when the secondary decreased to a mass of $0.3M_{\odot}$ then the secondary would have lost $0.7M_{\odot}$ and only $0.21M_{\odot}$ (or 30% of $0.7M_{\odot}$) would have been accreted by the primary resulting in a mass of $1.61M_{\odot}$. We have examined 21 curves like those in Figure 5.7, we measured and plotted their peak value and the full-width-half-maximum (FWHM) in Figure 5.8. The error bars denote the FWHM of the curves, the plotted point is the peak value for each curve, and the mass of J1903+0327 is shown as a dashed line. Examination of Figure 5.8 shows that given the observed mass and the assumptions we used in preparing the simulated systems, J1903+0327's progenitor system would have most likely had an F_{acc} value between between 0.35 and 0.5, with the peak value of 0.4 most closly maching the observed mass.

It should be noted however, not all of the barionic mass transfered results in an equivalent increase in gravitational mass of the primary since $M_{accrete} = \Delta M_{grav} + \Delta E_{binding}/c^2$ (Bagchi 2011), where $M_{accrete}$ is the mass accreted from the secondary, ΔM_{grav} is the change in gravitational mass of the primary, and $\Delta E_{binding}$ is the binding energy of the system. We find that for the masses being transfered in our simulations the effect is of using $M_{accrete} = \Delta M_{grav}$ is less than the our uncertanty in the final results.

Finally, we preform the same analysis that produced Figure 5.7 but use an initial primary mass of 1.2, 1.3, 1.4 (as used in all of the previous simulations), 1.5, and 1.6 $M_{\odot}$. These simulations were preformed for eight inner semi-major axes (10, 20, 30, 40, 50, 60, 70, and 100 $R_{\odot}$) at the start of mass transfer. The F_{acc} value with the peak number of occurrences closest to the observed mass of J1903+0327 (1.667 $M_{\odot}$) was recorded, as was the number of occurrences at that peak; these values were plotted in Figure 5.9. Upon examining Figure 5.9 we find that as the initial mass of the primary increases the most likely F_{acc} value and its domain decrease. To understand these results we recall that as the initial mass of the primary increases the amount of mass needed to reach the observed mass of J1903+0327 is decreased. So, for example, if the initial mass of the progenitor of J1903+0327's primary (before it began to accrete material from the secondary) was 1.6 $M_{\odot}$ it would only need to accrete 0.067 $M_{\odot}$ before the system reached the observed mass. A very small F_{acc} value can result in the transfer of such a small amount of material allowing the F_{acc} to stay low;

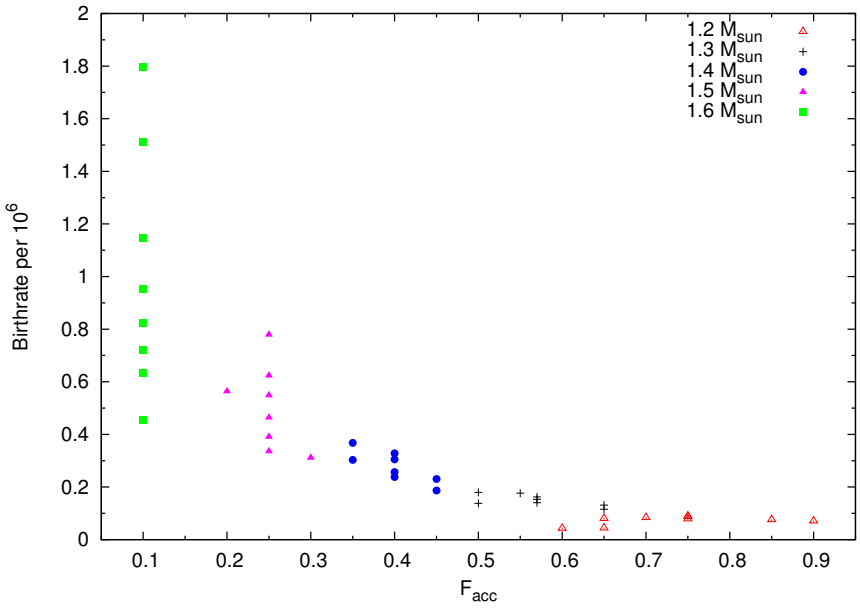


Figure 5.9: The number of systems per millon simulations with a final primary mass of 1.667 $M_{\odot}$ (the observed mass of J1903+0327) as a function of the fraction of accreted mass, for different initial primary masses (shown in the key).

with a lager F_{acc} value the system will often reach a final primary mass greater than 1.667 $M_{\odot}$ thus limiting the domain. Whereas if the initial primary mass was 1.2 $M_{\odot}$, an F_{acc} value of 0.1 would never allow for enough mass to be transfered, but there are a large range of F_{acc} values that can allow for that amount of mass transfer that would not quickly overshoot the observed mass. This assumes, as we have, that the mass transfer is stable as long as the triple is dynamically stable. We find that for an initial mass of the primary of 1.4 $M_{\odot}$, the value used for all the other simulations, the peak F_{acc} value is not sensitive to the semi-major axis at the beginning of the mass transfer; the F_{acc} value ranges between 0.35 and 0.45 which lies within our expected range of 0.35 to 0.5 found above from Figure 5.8.

5.4 Conclusion

We have examined the effect of an asymmetric supernova (SN) on a hierarchical multiple star system and considered how it can be modeled by applying the effective binary method. This is done by recursively replacing the inner binary by an effective star at the center of mass of that binary. The effective star experiences an effective SN with the effects of sudden mass loss, an instantaneous

translation and an effective kick velocity, i.e. the systemic velocity of the inner binary. We have coded the equations in this paper in a small python script.

We point out that the effective SN is different from a physical SN which has the mass loss occur from the position of the star undergoing the physical SN. The off-center mass loss in an effective SN becomes important only if the shell impact on the companion(s) is considered, and otherwise causes no difference between a real and effective SN calculation. Furthermore, we calculated the runaway velocities for dissociating binaries and effective binaries. We subsequently demonstrated how calculating the effect of a SN on a multiple can be generalized to multiples in which a star other than the primary is undergoing the SN.

We used this method to examine the case for J1903+0327 forming from a hierarchical triple. We assume initial masses of 10, 1.0, and 0.9 $M_{\odot}$ for the primary, secondary, and tertiary respectively, as well as an inner semi-major axis of 200 $R_{\odot}$. We find that if J1903+0367 was to form through such a mechanism it would be most likely to have a very low SN kick velocity so that it would remain stable after the SN, and a large inner semi-major axis after the CE phase to increase the likelihood that the triple would become unstable once the NS/MSP reached a mass of 1.667 $M_{\odot}$ (Freire et al. 2011). We also find that, given our assumptions, the transfer efficiency, F_{acc}, for J1903+0327 would have likely been between 0.35 and 0.5.

5.5 Acknowledgements

We thank Elena Maria Rossi for her useful suggestions.

CHAPTER 6 Summary

The fundamental thing in astronomy is the star. Every study in astronomy is based on, in, about, around, or somehow related to stars and their physical processes. This thesis is no different. In particular, I focus on different forms of collapse related to stars and groups of stars.

Most stars are born in groups, and some of these groups can be amazingly massive with many thousands or more stars. As stars form in a group, or cluster, the cluster itself may start to contract, or collapse, and this collapse can lead to interesting systems. As the cluster collapses all the stars begin moving faster as well as ever closer together, this can lead to–among other things–collisions, the formation of binaries or larger sets, and the ejection of stars from the system as they are slingshot outward.

When stars reach the end of their life, having burned all of their nuclear fuel one of only a few things can happen to them. If the star is less than about 8-10 times the mass of our Sun, they will push off most of their material through strong winds and periodic pulsations. If it is more massive it will lose most of its material in a collapse followed by an awe-inspiring explosion called a supernova. If it was a very massive star, more than about 20 times the mass of the Sun, than it might collapse into a black hole after the supernova. Black holes like these are called stellar mass black holes[1], because they are expected to have masses between a few times the mass of our Sun to tens of times the mass of the Sun.

Chapters 2 and 3 of this thesis examine how stars behave when they are born in clusters, while the other two chapters, namely 5 and 4, examine what large stars do when they die. In the former I examine what happens to clusters as the stars are just being born; are the clusters likely to contract as the stars are

[1] Other classes of black holes exist: supermassive black holes are more than about one million times the mass of the Sun and are observed at the center of galaxies. If the mass of a black hole is between about one hundred and one million times the mass of the Sun it would be called an intermediate mass black hole–though no such objects have been definitively identified, currently HLX-1, as discussed in Chapter 4, is the leading candidate for such an object.

formed, and if they are likely to contract, then by how much. I also examine how stars arrange themselves within these clusters; often young clusters are seen to have the most massive stars near the center of the cluster and we have identified the most likely way that happens. In the latter case I make an estimate of the number of intermediate mass black holes that we should expect to be within about 325 million light years from Earth. Finally, in Chapter 5 I show what can happen in a triple star system when one of the stars goes supernova.

All of these studies have been done not primarily by looking into the night sky and observing what happens, but rather by using a computer to simulate what stars will do under the influence of gravity and other physical processes. But why would we use computers and simulations when there are so many stars at which we could point our telescopes?

6.1 The Role of Simulations

Consider, for a moment, that aliens observed Earth and, with their sophisticated technology, they were able to take a photograph containing the image of every living human at one instance in time. From this photograph the aliens would likely work out that most humans are between the ages of 20 and 60 (Earth) years old. The aliens may discover from the photo and clever theories and measurements that the young humans eventually advance to the middle-aged class and that the middle-aged humans advance to the still older class.

While the aliens could learn many things about humans from that photograph of a single moment in time, it stands to reason that they would learn vastly more from a video showing all living humans and their activities during some amount of time. And the longer the video the more and more secrets would be unlocked, allowing them to study not only how humans age and are grouped, but how they migrate from one place to another, and if the video were long enough maybe even how civilizations rise and fall.

Astronomers (human ones at least) have this same difficulty. By using telescopes we have taken photographs (and data) of many stars, and from this information we have pieced together an amazing history of the Universe. We have learned that stars are born often times with siblings, and then they enter a long mid-life phase which is usually very stable, and then they enter a dynamic late-life phase, and finally die in, usually, rather beautiful ways. We have learned, just from our "star snapshot", about galaxies, and cosmic voids, and black holes, and supernova, and on and on. But we can make a video, or an expected video at least, through the use of simulations. Simulations allow us to use a computer, programmed with the laws of physics, and determine what a galaxy might have looked like a million or even a billion years ago. They allow us to see the past Universe in a way that we could not otherwise see, and to

extrapolate how the Universe will change in the future which would otherwise require us to observe it for millions of years.

Simulations are not guaranteed to be correct and they should be approached thoughtfully. However, with careful considerations and basic assumptions we can approximate what is and has been happening in Universe near and far. Simulations are a powerful tool for the astronomer, and it is through these theoretical methods that I have performed the work detailed in this thesis.

6.2 Collapsing Clusters

In Chapters 2 and 3 I detail the results from more than 500 simulations of star clusters. Each simulation was started with the stars in that simulation having different velocities than the stars in the other simulations; in some simulations the stars were given so much velocity, kinetic energy, that most of the stars were flung away from the system–traveling too fast for the gravity from the other stars to keep everything bound. In other simulations the stars were given the exact velocity so that no stars were lost and they moved in orbits almost as if they had always been moving in that way, called virial systems; and in other simulations,called cold systems, the stars were given no initial velocity at all and in those simulations the stars immediately started to fall toward the center of the cluster, this is a star cluster in collapse.

6.2.1 Taking a Star Cluster's Temperature

In Chapter 2 I show that the choice of which velocity, kinetic energy, the system is initially given makes a dramatic impact on how the system evolves. Because the simulations had shown the effect of the initial stellar velocity on the evolution of the cluster it became possible to identify the initial stellar velocities of a young cluster if that cluster had been observed in detail.

Somewhere in the Large Magellanic Cloud, a neighboring galaxy, is a very young star cluster called R136. Due to its age and the fact that it has been observed many times R136 proved to be an ideal observational companion to this theoretical study. Comparing the measured radius of the cluster core, the distribution of the stars, the ratio of kinetic to potential energy, and the cluster's age to the simulations we were able to determine the initial velocity of the stars in R136 was most likely between about 0.4 and 0.5 time the velocity they would have been in virial system.

When this analysis was extended to include 15 more young star clusters the most common initial velocity was found to be between 0.6 and 0.7 times the initial velocity in the virial system. If other star clusters are like the ones studied here then we have learned that nature may tend to make star cluster cool, but not cold. However, to fully understand the physics in these star clusters we need

to push the simulations even further; we need to consider the physics of gas and dust in the cluster, and just how many stars are initially in binaries, for example. As we add more and more complexity to our simulations, our videos of an alien system, we will find more and more details about just how nature works.

6.2.2 Why do all of the Big Stars Clump Together?

Chapter 3 is about one thing, what causes all of the most massive stars to clump together in young clusters? Young cluster are known to mass segregate, that is the more massive stars tend to be clumped together, but the way they do this so quickly was not understood. Two ideas had been proposed: The first idea was that as the young cluster contracts it becomes very dense, and when they are all very close to each other the most massive stars tend to find the other massive stars and then stay close to one another, due to gravity. The second idea suggested was that is the star cluster contracts, little sub-clusters form and, because of their size, these sub-clusters mass segregate very rapidly and that effect is preserved after all of the sub-clumps had merged.

Because there was so much data to examine in the simulations we needed to develop a new, faster method to measure if, and to what degree, a star system was mass segregated. That was accomplished the new method is orders of magnitude faster than the previous method and its results are more robust.

After developing the new method I was able to design an experiment where I took one simulation and measured the mass segregation of the system at each moment in time for the length of the simulation. Then, after running the simulation again but for only part of the time, I randomly rearranged the masses, being sure to not change the velocity or position of each star, and then finished the simulation. I did this five different times, each time starting from the same, original setup and moving the masses at a different time. Twice I randomly switched the masses while the star cluster was collapsing, twice I randomly rearranged the masses after the collapse, and once I randomly reordered the masses at the moment the system was the most dense.

If the amount of mass segregation did not change significantly after swapping the masses at and after the collapse then either our method was not working or neither proposed idea was correct about how the cluster became mass segregated; this however was not the case.

If, after switching the masses around before the moment the system was its most contracted, the mass segregation *was* significantly changed at the end of the simulation then the second scenario is correct because in that case it matters where the masses are before the deepest moment of the collapse. If however, the mass segregation was *not* significantly changed at the end of the simulation then it means the mass segregation occurs when the system is in the deep part of the collapse and so the first scenario is correct.

The result showed that the first scenario is more correct. If the masses are jumbled before the collapse it makes little to no difference on the final mass segregation of the system. That means the important time, for mass segregation, is when the system is very dense and the time before that when the second proposed idea would be working is of little importance.

6.3 Collapsing Stars

When massive stars die they experience a collapse leading to a supernova and if they are massive enough they may collapse again into a black hole. In Chapter 5 I look at the effect a supernova will have on a system of three or more stars. When a star goes supernova it loses much of its mass and so the gravitational force felt by the other stars is reduced, which can lead to the stars no longer being gravitationally bound to one another. In Chapter 4 I estimate the number of intermediate mass black holes, IMBHs, that should be in the local Universe.

6.3.1 Supernova

It is not uncommon for stars to be found in gravitationally bound groups of two, three or more. If one, or more, of the stars in these small star systems is massive enough to go supernova then there will be a large and sudden loss of mass in the system. This mass loss may cause a previously stable system to become unstable due to the change in the gravitational forces between the stars.

In Chapter 5 we examine triple systems where two stars are close together and the third star is relatively far away, called a hierarchal triple, the two close stars can be approximated as a single star from the perspective of the outer star. Using this method I determine the conditions required for the system to remain stable after the supernova, and inversely which conditions will lead to the stars no longer being bound together.

Using this method I ran simulations to determine if it was possible for the currently observed millisecond pulsar[2] J1903+0327 to have been formed in a triple system which became unstable after a supernova. I was able to determine that the system could form this way and the likely mass of the stars before the supernova. Again, by making use of simulations (a video of some part of the Universe) we are able to learn much more than by observations (a photograph) alone.

[2] A millisecond pulsar is a star with rotates once every few milliseconds (one one-thousandths of a second). They are important for a variety of reasons, including being very accurate as a clock.

6.3.2 Intermediate Mass Black Holes

While we have a strong understanding of many things in the Universe there are many more things we do not understand. An example of something we do not understand are where all Intermediate Mass Black Holes (IMBHs) are. These objects would have a mass between about one hundred and one million times the mass of our Sun, but as of yet an IMBH has not been definitively observed, where as less massive and more massive black hole have been detected. However, there is no good theory as to why nature should not produce these mid-sized black holes so we continue looking for them.

There have been several suggested candidates in the past which turned out to be different types of objects. One possible IMBH, HLX-1, is the strongest candidate to date, with another good candidate in M82 X-1. Using these two candidates as prototypes, and the assumption that they are both in fact IMBHs, I estimate in Chapter 4the number of IMBHs that statistically must be out there in order for these two black holes to observed. In other words, how many IMBHs would we need to have in the nearby Universe in order to detect two?

This estimate is based on assuming why these black holes are visible and finding the likelihood that such a detectable system would form and be observable right now. I found that, given our assumptions, there would need to be around 100 million IMBHs within about 325 million light years. That would mean around 1000 IMBH per galaxy, if there were an equal number per galaxy.

CHAPTER 7 Samenvatting

De ster is de fundamentele eenheid in sterrenkunde, al het sterrenkundig onderzoek is, zoals de naam al zegt, op één of andere manier gerelateerd aan sterren en hun fysische processen. In dit proefschrift is dit niet anders. Om specifiek te zijn, in dit werk focus ik me op verschillende vormen van ineenstorting gerelateerd aan sterren en groepen van sterren.

De meeste sterren worden geboren in groepen en sommige van deze groepen bestaan uit vele duizenden sterren en kunnen ongelofelijk zwaar zijn. Tijdens de vorming van een groep van sterren, ook wel sterrenhoop genoemd, kan het gebeuren dat de sterrenhoop begint te krimpen, of zelfs ineenstort, en het ineenstorting van deze sterrenhopen kan interessante systemen opleveren. Tijdens het ineenstorten van de sterrenhoop gaan de sterren steeds sneller bewegen en komen ze dichter bij elkaar. Het feit dat de sterren dichter bij elkaar komen heeft vele gevolgen bijvoorbeeld: er ontstaan dubbelsterren, ook wel binaire sterren genoemd, of zelfs systemen die bestaan uit meer dan twee om elkaar draaiende sterren, sterren kunnen uit de sterrenhoop worden gekatapulteerd en het is zelfs mogelijk dat sterren op elkaar botsen.

Een ster heeft niet het eeuwige leven en als aan het eind van zijn leven alle nucleaire brandstof verbruikt is zijn er nog maar een paar dingen die met de ster kunnen gebeuren. Als de ster lichter is dan 8 tot 10 zonnemassa's[1] dan zal de ster op een gegeven moment periodisch gaan pulseren en het meeste van wat er nog van de ster over is zal worden weggeblazen door sterke winden. Als de ster zwaarder is dan 10 zonnemassa's zal het meeste van het materiaal verdwijnen in een alles overwelmende explosie, een zogenaamde supernova. Als het een zeer zware ster is, van meer dan 20 zonnemassa's, dan kan er een zwart gat gevormd worden na de supernova. Dit soort zwarte gaten noemen we stellaire zwarte gaten[2], omdat verwacht wordt dat ze een gewicht hebben dat tussen een paar

[1] Eén zonnemassa is gelijk aan het gewicht van de zon.

[2] Er bestaan ook andere soorten zwarte gaten: Superzware zwarte gaten, deze zijn meer dan een miljoen keer zwaarder dan de zon en zijn veelvuldig geobserveerd in het centrum van sterrenstelsels. Als het gewicht van het zwarte gat tussen de honderd en een miljoen zonnemassa's

zonnemassa's en enkele tientallen zonnemassa's ligt.

Hoofdstukken 2 en 3 van dit proefschrift gaan over het gedrag van sterren die geboren worden in sterrenhopen, terwijl hoofdstukken 4 en 5 als thema het overlijden van grote sterren hebben.

In de eerste twee onderzoek ik wat er gebeurt met sterrenhopen vlak nadat de sterren geboren zijn; hoe waarschijnlijk is het dat sterrenhopen krimpen als ze net gevormd zijn, en als het waarschijnlijk is dan willen we graag weten hoeveel ze precies krimpen. Tegelijkertijd onderzoek ik hoe de sterren zichzelf binnen deze sterrenhopen ordenen. Vaak zien we dat in jonge sterrenhopen de zwaarste sterren zich in het centrum bevinden en in dit proefschrift hebben we de meest waarschijnlijke oorzaak hiervoor geïdentificeerd.

In de laatste hoofstukken laat ik zien wat er gebeurt als in een systeem van drie sterren één van deze sterren een supernova wordt. Verder benader ik het aantal middelzware zwarte gaten dat we kunnen verwachten in een gebied van 325 miljoen lichtjaar rond de Aarde.

Sterrenkunde wordt vaak geassocieerd met 's avonds naar de sterren kijken om te zien wat er met ze gebeurt, maar dat is niet de primaire onderzoeksmethode die in dit proefschrift gebruikt wordt, maar in plaats daarvan wordt een computer gebruikt om te simuleren hoe zwaartekracht en andere fysische processen de sterren beïnvloeden. Maar waarom zouden we simulaties gebruiken als er zoveel sterren zijn waarop we onze telescopen kunnen richten?

7.1 De rol van simulaties

Stelt u zich eens voor dat er buitenaardse wezens zijn die de Aarde bestuderen en met hun geavanceerde technologie in staat zijn om een foto te maken met daarop elke levende mens.

Met behulp van deze foto zullen de aliens instaat zijn om te concluderen dat de meeste mensen tussen de 20 en 60 (aard-) jaren oud zijn. Verder zullen ze met behulp van de foto, slimme metingen en theorieën, waarschijnlijk ontdekken dat de jonge mensen uiteindelijk uit zullen groeien naar mensen van middelbare leeftijd en de mensen van middelbare leeftijd zullen groeien naar een oudere leeftijdsklasse.

Hoewel de buitenaardse wezens van dat ene moment, gevangen in de foto, veel over de mens kunnen leren is het vanzelf sprekend dat ze nog zoveel meer kunnen leren van een film die het leven van alle mensen en hun activiteiten gedurende de lengte van de film laat zien. Hoe langer de film hoe meer geheimen

---

ligt dan wordt het een middelzwaar zwart gat genoemd–echter er is tot nu toe geen definitieve observatie van een dergelijk zwart gat gedaan. Op dit moment is HLX-1 de belangrijkste kandidaat om als middelzwaar zwart gat geclassificeerd te worden, dit object wordt in meer detail besproken in Hoofdstuk 4.

de aliens kunnen ontdekken, wat hun in staat stelt om niet alleen te bestuderen hoe mensen ouder worden en hoe ze gegroepeerd zijn, maar ook hoe ze zich verplaatsen van de ene naar de andere plaats en, als de film lang genoeg zou zijn, zelfs hoe beschavingen ontstaan, groeien en weer ten onder gaan.

Sterrenkundige (althans de menselijke) hebben hetzelfde probleem. Door gebruik te maken van telescopen hebben we foto's gemaakt (en data verzameld) van de vele sterren om ons heen, en met behulp van deze informatie hebben we de verbazingwekkende geschiedenis van het heelal kunnen achterhalen.

Zo hebben we bijvoorbeeld geleerd dat sterren geboren worden, vaak tegelijkertijd met broers en zussen, in een gewelddadige omgeving, waarna ze tijdens hun middelbare leeftijd een lange periode van relatieve rust kennen. Maar uiteindelijk komen ze in hun nadagen, welke weer zeer dynamische en geweldadig zijn en tenslotte sterven ze op een vaak spectaculair mooie manier. We hebben geleerd over sterrenstelsels, kosmische leegtes, zwarte gaten, supernova's, etc., enkel door gebruik te maken van foto's. Maar we kunnen een film maken door gebruik te maken van simulaties. Door computers te gebruiken, geprogrammeerd met de wetten van de fysica, kunnen we simulaties uitrekenen om te bepalen hoe een sterrenstelsel er een miljoen of zelfs een miljard jaar geleden uitzag. Ze stellen ons in staat om te kijken naar het verleden van het heelal, iets wat op geen enkel andere manier mogelijk is, en te extrapoleren hoe het heelal in de toekomst zal veranderen, iets wat eigenlijk miljoenen jaren van observaties zou vereisen.

Het is niet gegarandeerd dat simulaties correct zijn en we moeten ze zorgvuldig en weloverwogen gebruiken. Maar, met gedegen uitgangspunten en een zorgvuldige benadering kunnen we bepalen wat er in het heelal, zowel dichtbij als ver weg, in het verleden gebeurt is en in de toekomst nog gaat gebeuren. Simulaties zijn voor sterrenkundigen een krachtig hulpmiddel en met behulp van deze theoretische methoden heb ik het werk, zoals beschreven in dit proefschrift, kunnen uitvoeren.

7.2 Instortende sterrenhopen

In Hoofdstukken 2 en 3 beschrijf ik de resultaten van meer dan 500 simulaties van sterrenhopen.

De begin snelheid waarmee we de sterren in de modellen initialiseren is in elke simulatie anders; in sommige simulaties was de snelheid, ook wel kinetische energie genoemd, van de sterren zo hoog dat het grootste deel van de sterren het systeem uit vloog–ze bewogen zo snel dat de gezamenlijke zwaartekracht van de andere sterren in het systeem niet sterk genoeg was om deze sterren vast te houden.

In andere simulaties hebben we de sterren precies de snelheid gegeven die

ervoor zorgt dat ze niet uit het systeem vliegen. In plaats daarvan bewogen de sterren in die systemen langs banen waarbij het lijkt alsof ze altijd in een dergelijke baan bewogen hadden, dit is een zogenaamd viriaal systeem. In weer andere simulaties, die we koude systemen noemen, hadden de sterren een snelheid die een fractie was van de sterren in een viriaal systeem. In onze laatste set van simulaties hadden de sterren helemaal geen begin snelheid en in deze simulaties begonnen de sterren, als gevolg van de zwaartekracht, meteen naar het centrum van de sterrenhoop te vallen. Dergelijke systemen noemen we ineenstortende sterrenhopen.

7.2.1 De temperatuur van een sterrenhoop bepalen

In Hoofdstuk 2 laat ik zien dat de keuze van de begin snelheid, kinetische energie, een dramatisch effect heeft op de manier waarop een sterrenhoop zich ontwikkeld.

De simulaties hebben ons laten zien dat de keuze van de initiële snelheid van de sterren een bepalend effect heeft op de evolutie van de sterrenhoop. Daardoor wordt het mogelijk om de initiële snelheid van sterren in een jonge sterrenhoop te bepalen als we deze sterrenhoop in detail hebben geobserveerd.

In de Grote Magelhaense Wolk (Large Magellanic Cloud), een naburig sterrenstelsel, bevindt zich een erg jonge sterrenhoop genaamd R136. Door zijn leeftijd, en het feit dat R136 veelvuldig is geobserveerd, is dit een ideale observationele kandidaat voor dit theoretische werk. We hebben de straal van de kern, de distributie van sterren, de ratio van de kinetische en potentiele energie en de leeftijd van de sterrenhoop vergeleken. Daardoor waren we instaat om te bepalen dat toen R136 gevormd werd, de snelheid van de sterren waarschijnlijk tussen de 0.4 en 0.5 keer de snelheid was van sterren in een vergelijkbaar viriaal systeem.

Nadat deze analyse was uitgebreid met 15 andere jonge sterrenhopen bleek dat de meest voorkomende initiële snelheid tussen de 0.6 en 0.7 keer de begin snelheid van viriale systemen lag. Als andere sterrenhopen vergelijkbaar zijn met de sterrenhopen die we hier onderzocht hebben dan hebben we geleerd dat in de natuur sterrenhopen wel koel, maar niet koud ontstaan.

Echter, om een volledig begrip te krijgen van de fysica in sterrenhopen moeten we de simulaties uitbreiden; we moeten bijvoorbeeld ook de fysica van gas en stof in de sterrenhopen meenemen, en weten hoeveel sterren er nou geboren worden als dubbelsterren. Naarmate we meer en meer complexiteit aan onze simulaties toevoegen zullen we meer en meer details achterhalen over hoe de natuur werkt en worden de films van de buitenaardse systemen steeds realistischer.

7.2.2 Waarom klonteren alle grote sterren samen?

In Hoofdstuk 3 staat één vraag centraal: wat zorgt ervoor dat de zwaarste sterren in jonge sterrenhopen zich bij elkaar groeperen?

Van jonge sterrenhopen is bekend dat er massa segregatie plaats vindt, dat betekent dat de zwaardere sterren samenklonteren, maar hoe het komt dat dit zo snel gebeurt, is nog niet bekend. In dit hoofdstuk worden er twee mogelijke scenario's voorgesteld. In het eerste scenario krimpen jonge sterrenhopen en worden daardoor erg compact. Doordat alle sterren zich vlak bij elkaar bevinden zal het sneller gebeuren dat de meest zware sterren in contact komen met andere zware sterren en als gevolg van de zwaartekracht zullen ze ook dicht bij elkaar blijven. In het tweede voorgestelde scenario worden er meerdere kleine sterrenhopen gevormd terwijl de sterrenhoop krimpt. In deze kleine sterrenhopen treed vervolgens erg snel massa segregatie op, omdat ze zo klein zijn. En als uiteindelijk alle kleine sterrenhopen weer zijn samengesmolten tot één enkele sterrenhoop zou in dit scenario het massa segregatie effect behouden gebleven moeten zijn.

De simulaties die we voor dit hoofdstuk hebben gedraaid hebben zoveel te onderzoeken data geproduceerd dat bestaande onderzoeksmethoden niet langer geschikt waren. Daarom moesten we een nieuwe, snellere methode ontwikkelen om te meten of er sprake was van massa segregatie in een sterrenhoop en zo ja in welke mate. Dit is uiteindelijk gelukt en de nieuwe methode is orders van grote sneller dan de vorige methoden en bovendien zijn de resultaten van betere kwaliteit.

Met deze nieuwe methode was ik in staat om een experiment te ontwerpen waarmee ik van een systeem, tijdens de simulatie, continue de massa segregatie kon meten. Daarna, nadat de simulatie voor een korte periode opnieuw gedraaid was, deed ik de gewichten van de sterren willekeurig herverdelen hierbij er voor zorgend dat de massa en snelheid niet werden aangepast. Na de herverdeling werd de simulatie hervat en werd uitgevoerd tot de eindtijd van de simulatie. Deze herverdeling hebben we op verschillende tijdstippen uitgevoerd. Twee keer deed ik de herverdeling van de gewichten tijdens de ineenstorting van de sterrenhoop, twee keer deed ik de herverdeling nadat de sterrenhoop ineengestort was en één keer vond de willekeurige herverdeling plaats op het moment dat sterrenhoop het meest compact was.

Als de mate van massa segregatie na de herverdeling van de massa's niet noemenswaardig was veranderd, tijdens en na de ineenstorting van de sterrenhoop, dan was er of iets mis met onze methode of geen van beide voorgestelde scenario's is correct. Dit bleek echter niet het geval te zijn.

Als we de gewichten herverdelen voordat het systeem ineengestort is en aan het einde van de simulatie zou blijken dat de massa segregatie *significant* anders was dan in de oorspronkelijke simulatie, dan is het tweede scenario de juiste.

Omdat in dat geval het belangrijk is waar de zwaarste sterren zich bevinden voor de ineenstorting. Echter als de massa segregatie *niet significant* veranderd is aan het einde van de simulatie dan betekent het dat de massa segregatie plaatsvindt terwijl het systeem aan het ineenstorten is en dan is het eerste scenario de juiste. De resultaten van de simulaties laten zien dat het eerste scenario het meest waarschijnlijk is. Als de gewichten door elkaar gegooid zijn voordat het systeem ineenstort dan zien we nauwelijks verschil in de uiteindelijke massa segregatie van het systeem. Dat betekent dat het meest belangrijke moment voor massa segregatie is op het moment dat het systeem het meest dicht en compact is en op dat moment heeft ons tweede scenario amper invloed.

7.3 Ineenstortende Sterren

Als zware sterren doodgaan, zullen ze ineenstorten met als gevolg een supernova en, als ze zwaar genoeg zijn, storten ze daarna nog een keer in en vormen dan een zwart gat. In Hoofdstuk 5 kijk ik naar de effecten die een supernova heeft op een systeem van drie of meer sterren. Als een ster een supernova ondergaat verliest deze het grootste deel van zijn massa, hierdoor wordt de zwaartekracht die de andere sterren in het systeem voelen verminderd, wat er vervolgens toe kan leiden dat sterren niet langer door de zwaartekracht met elkaar gebonden zijn. In Hoofdstuk 4 benader ik het aantal middelgrote zwarte gaten, MGZG, dat aanwezig moet zijn in het nabije heelal.

7.3.1 Supernova

Het is niet ongebruikelijk om sterren te vinden die zich vanwege de zwaartekracht in groepen van twee, drie of meer bevinden. Als één, of meerdere, van de sterren in deze kleine sterrenhopen zwaar genoeg is om een supernova te vormen dan zal er een significante en snelle reductie optreden in de massa van deze sterrenhoop. Dit grote verlies in massa kan een stabiele sterrenhoop veranderen in een onstabiele sterrenhoop, doordat door de gewichtsverandering de zwaartekracht tussen de sterren anders wordt.

In Hoofdstuk 5 onderzoeken we systemen bestaande uit drie sterren waarbij twee sterren zich vlak bij elkaar bevinden en de derde ster relatief ver weg is, dit wordt ook wel een hiërarchisch drieling systeem genoemd. Voor de buitenste ster kunnen we de twee sterren die zich vlak bij elkaar bevinden representeren als een enkele ster. Door gebruik te maken van deze representatie bepaal ik welke condities vereist zijn om te zorgen dat het systeem na een supernova stabiel blijft, en andersom welke condities zullen leiden tot een systeem van sterren dat niet langer door zwaartekracht gebonden is.

Door wederom gebruik te maken van de bovenstaande representatie heb ik simulaties gedraaid om uit te zoeken of het mogelijk is dat de geobserveerde

millisecondepulsar[3] J1903+0327 gevormd is in een systeem van drie sterren dat onstabiel geworden is na een supernova. Ik was in staat om te bepalen dat het systeem inderdaad op deze manier gevorm kan zijn en wat de meeste waarschijnlijke massa's van de sterren waren voor de supernova. Wederom, door gebruik te maken van simulaties (een film van een deel van het heelal) waren we in staat om veel meer te leren dan wanneer we enkel gebruik gemaakt hadden van observaties (foto's).

7.3.2 Middelgrote Zwarte Gaten

Ondanks dat we veel dingen begrijpen in het heelal zijn er nog veel meer dingen die we niet begrijpen. Een voorbeeld van iets wat we niet begrijpen zijn middelgrote zwarte gaten (MGZG). Deze objecten zouden een gewicht hebben van tussen de 100 en een miljoen zonnemassa's, maar tot nu toe zijn er geen definitieve observaties van een MGZG, terwijl er wel lichtere en zwaardere zwarte gaten zijn gedetecteerd. Echter, er is geen goede theorie over waarom de natuur niet instaat zou zijn om dit soort zwarte gaten te vormen dus we blijven verwachten ze ooit te vinden.

In het verleden zijn er verschillende kandidaten geweest maar elke keer bleek dat het toch om een ander soort object ging. Op dit moment lijkt HLX-1 de meest geschikte kandidaat om te worden geclassificeerd als MGZG, op de voet gevolgd door M82 X-1. Door deze twee kandidaten te gebruiken als prototype, en daarbij de aanname te doen dat het inderdaad MGZGs zijn, maak ik in Hoofdstuk 4 een schatting van hoeveel MGZGs er statistisch gezien zouden moeten zijn. Gebaseerd op het feit dat we deze twee kunnen observeren. In andere woorden, hoeveel MGZGs moeten er in het nabije heelal zijn willen we er twee detecteren.

Deze schatting maakt gebruik van aannames waarom deze zwarte gaten zichtbaar zijn, en de waarschijnlijkheid dat dit soort detecteerbare systemen juist op dit moment vormen. Ik vond dat, gegeven onze aannames, er rond de 100 miljoen MGZGs zijn binnen een gebied van 325 miljoen lichtjaar. Dat betekent dat er ongeveer 1000 MGZGs per sterrenstelsel zijn, mits er in elk sterrenstelsel even veel zouden zijn.

[3] Een millisecondepulsar is een ster die elke paar milliseconden (een milliseconde is één duizendste van een seconde) om zijn as draait. Dit soort sterren zijn, om verschillende redenen, belangrijk onder andere omdat ze gebruikt kunnen worden als een zeer precieze klok.

List of publications

Peer-Reviewed Publications

- *Rapid Mass Segregation in Collapsing Clusters*
  D. Caputo, N. de Vries, and S. F. Portegies Zwart.
  (In preperation)

- *On Estimating the Total Number of Intermediate Mass Black Holes*
  D. Caputo, N. de Vries, A Patruno, and S. F. Portegies Zwart.
  (Submitted to Monthly Notices of the Royal Astronomical Society)

- *On the Effects of Subvirial Initial Conditions and the Birth Temperature of R136*
  D. Caputo, N. de Vries, and S. F. Portegies Zwart.
  Monthly Notices of the Royal Astronomical Society, 445:674-685, November 2014.
  doi10.1093/mnras/stu1769

- *Asymmetric Supernova in Hierarchical Multiple Star Systems and Aapplication to J1903+0327*
  J. T. Pijloo, D. Caputo, and S. F. Portegies Zwart.
  Monthly Notices of the Royal Astronomical Society, 424:2914-2925, August 2012.
  doi10.1111/j.1365-2966.2012.21431.x

- *Cellular-Swarm Optimization: A Scalable Multimodal Swarm Optimizer*
  R. Dolan, D. Caputo , and G. DeSouza.
  2012 IEEE Congress on Evolutionary Computation

- *The Swarm Computer, an Analog Cellular-Swarm Hybrid Architecture*
  R. Dolan, G. DeSouza, and D. Caputo.
  Hybrid Intelligent Systems 2010, 119-124, 2010.
  doi/10.1109/HIS.2010.5600079.

Selected Conference Proceedings and Presentations

- *Fishing on the Sea of Big Data: The Swarming Agent Method*
  D. Caputo and R. Dolan.
  TarGet Conference 2014, November 2014.

- *Searching for Data: Swarming Agent Method*
  D. Caputo, and R. Dolan.
  Advances in Computational Astrophysics: Methods, Tools, and Outcome, Volume 453 of Astronomical Society of the Pacific Conference Series, July 2012.

- *PAH Formation: 3.3 And 11.3 μm Data*
  D. Caputo, A. Speck, K. Volk, M. Barlow, and R. Wesson.
  American Astronomical Society Meeting #214, May 2009.

Bibliography

S. J. Aarseth, D. N. C. Lin, and J. C. B. Papaloizou. On the collapse and violent relaxation of protoglobular clusters. *ApJ*, 324:288–310, January 1988. doi: 10.1086/165895.

F. C. Adams, E. M. Proszkow, M. Fatuzzo, and P. C. Myers. Early Evolution of Stellar Groups and Clusters: Environmental Effects on Forming Planetary Systems. *ApJ*, 641:504–525, April 2006. doi: 10.1086/500393.

R. J. Allison, S. P. Goodwin, R. J. Parker, R. de Grijs, S. F. Portegies Zwart, and M. B. N. Kouwenhoven. Dynamical Mass Segregation on a Very Short Timescale. *ApJ*, 700:L99–L103, August 2009a. doi: 10.1088/0004-637X/700/2/L99.

R. J. Allison, S. P. Goodwin, R. J. Parker, S. F. Portegies Zwart, R. de Grijs, and M. B. N. Kouwenhoven. Using the minimum spanning tree to trace mass segregation. *MNRAS*, 395:1449–1454, May 2009b. doi: 10.1111/j.1365-2966.2009.14508.x.

R. J. Allison, S. P. Goodwin, R. J. Parker, S. F. Portegies Zwart, and R. de Grijs. The early dynamical evolution of cool, clumpy star clusters. *MNRAS*, 407:1098–1107, September 2010. doi: 10.1111/j.1365-2966.2010.16939.x.

M. Andersen, H. Zinnecker, A. Moneti, M. J. McCaughrean, B. Brandl, W. Brandner, G. Meylan, and D. Hunter. The Low-Mass Initial Mass Function in the 30 Doradus Starburst Cluster. *ApJ*, 707:1347–1360, December 2009. doi: 10.1088/0004-637X/707/2/1347.

P. André. Nearby Protoclusters as Laboratories for Understanding Star Formation on Galactic Scales. *Ap&SS*, 281:51–66, July 2002. doi: 10.1023/A:1019599328220.

I. Arad and P. H. Johansson. A numerical comparison of theories of violent relaxation. *MNRAS*, 362:252–262, September 2005. doi: 10.1111/j.1365-2966.2005.09293.x.

I. Arad and D. Lynden-Bell. Inconsistency in theories of violent relaxation. *MNRAS*, 361:385–395, August 2005. doi: 10.1111/j.1365-2966.2005.09133.x.

M. Bagchi. The role of binding energies of neutron stars on the accretion-driven evolution. *MNRAS*, 413:L47–L50, May 2011. doi: 10.1111/j.1745-3933.2011.01030.x.

H. Baumgardt, J. Makino, P. Hut, S. McMillan, and S. Portegies Zwart. A Dynamical Model for the Globular Cluster G1. *ApJ*, 589:L25–L28, May 2003. doi: 10.1086/375802.

J. Bédorf and S. Portegies Zwart. The effect of many minor mergers on the size growth of compact quiescent galaxies. *MNRAS*, 431:767–780, May 2013. doi: 10.1093/

mnras/stt208.

J. Bédorf, E. Gaburov, M. Fujii, K. Nitadori, T. Ishiyama, and S. Portegies Zwart. 24.77 pflops on a gravitational tree-code to simulate the milky way galaxy with 18600 gpus. In , editor, *The Proceedings of Super Computing 2014*, volume 0000 of *Super Computing*, 2014.

M. Bejger, M. Fortin, P. Haensel, and J. L. Zdunik. Implications of the measured parameters of PSR J1903+0327 for its progenitor neutron star. *A&A*, 536:A87, December 2011. doi: 10.1051/0004-6361/201117468.

D. Bhattacharya and E. P. J. van den Heuvel. Formation and evolution of binary and millisecond radio pulsars. *Phys. Rep.*, 203:1–124, 1991. doi: 10.1016/0370-1573(91)90064-S.

A. Blaauw. On the origin of the O- and B-type stars with high velocities (the "runaway" stars), and some related problems. *Bull. Astron. Inst. Netherlands*, 15:265–+, May 1961.

L. Blecha, N. Ivanova, V. Kalogera, K. Belczynski, J. Fregeau, and F. Rasio. Close Binary Interactions of Intermediate-Mass Black Holes: Possible Ultraluminous X-Ray Sources? *ApJ*, 642:427–437, May 2006. doi: 10.1086/500727.

J. Boersma. Mathematical theory of the two-body problem with one of the masses decreasing with time. *Bull. Astron. Inst. Netherlands*, 15:291–301, May 1961.

I. A. Bonnell and M. B. Davies. Mass segregation in young stellar clusters. *MNRAS*, 295:691, April 1998. doi: 10.1046/j.1365-8711.1998.01372.x.

B. Brandl, B. J. Sams, F. Bertoldi, A. Eckart, R. Genzel, S. Drapatz, R. Hofmann, M. Loewe, and A. Quirrenbach. Adaptive Optics Near-Infrared Imaging of R136 in 30 Doradus: The Stellar Population of a Nearby Starburst. *ApJ*, 466:254, July 1996. doi: 10.1086/177507.

B. Campbell, D. A. Hunter, J. A. Holtzman, T. R. Lauer, E. J. Shayer, A. Code, S. M. Faber, E. J. Groth, R. M. Light, R. Lynds, E. J. O'Neil, Jr., and J. A. Westphal. Hubble Space Telescope Planetary Camera images of R136. *AJ*, 104:1721–1742, November 1992. doi: 10.1086/116355.

D. P. Caputo, N. de Vries, and S. Portegies Zwart. On the effects of subvirial initial conditions and the birth temperature of R136. *MNRAS*, 445:674–685, November 2014. doi: 10.1093/mnras/stu1769.

L. I. Caramete and P. L. Biermann. The mass function of nearby black hole candidates. *A&A*, 521:A55, October 2010. doi: 10.1051/0004-6361/200913146.

S. Casertano and P. Hut. Core radius and density measurements in N-body experiments Connections with theoretical and observational definitions. *ApJ*, 298:80–94, November 1985. doi: 10.1086/163589.

D. J. Champion, S. M. Ransom, P. Lazarus, F. Camilo, C. Bassa, V. M. Kaspi, D. J. Nice, P. C. C. Freire, I. H. Stairs, J. van Leeuwen, B. W. Stappers, J. M. Cordes, J. W. T. Hessels, D. R. Lorimer, Z. Arzoumanian, D. C. Backer, N. D. R. Bhat, S. Chatterjee, I. Cognard, J. S. Deneva, C.-A. Faucher-Giguère, B. M. Gaensler, J. Han, F. A. Jenet, L. Kasian, V. I. Kondratiev, M. Kramer, J. Lazio, M. A. McLaughlin, A. Venkataraman, and W. Vlemmings. An Eccentric Binary Millisecond Pulsar in the Galactic Plane. *Science*, 320:1309–, June 2008. doi: 10.1126/science.1157580.

S. Chandrasekhar. Dynamical Friction. I. General Considerations: the Coefficient of

Dynamical Friction. *ApJ*, 97:255, March 1943. doi: 10.1086/144517.

J. E. Dale, J. Ngoumou, B. Ercolano, and I. A. Bonnell. Before the first supernova: combined effects of H II regions and winds on molecular clouds. *MNRAS*, 442: 694–712, July 2014. doi: 10.1093/mnras/stu816.

J. H. J. de Bruijne. Science performance of Gaia, ESA's space-astrometry mission. *Ap&SS*, 341:31–41, September 2012. doi: 10.1007/s10509-012-1019-4.

G. de Marchi, A. Nota, C. Leitherer, R. Ragazzoni, and C. Barbieri. The Population of Massive Stars in R136 from Faint Object Camera Ultraviolet Observations. *ApJ*, 419:658, December 1993. doi: 10.1086/173516.

G. C. Dewangan, L. Titarchuk, and R. E. Griffiths. Black Hole Mass of the Ultraluminous X-Ray Source M82 X-1. *ApJ*, 637:L21–L24, January 2006. doi: 10.1086/499235.

M. Dickinson, C. Papovich, H. C. Ferguson, and T. Budavári. The Evolution of the Global Stellar Mass Density at 0<z<3. *ApJ*, 587:25–40, April 2003. doi: 10.1086/368111.

T. Ebisuzaki, J. Makino, T. G. Tsuru, Y. Funato, S. Portegies Zwart, P. Hut, S. McMillan, S. Matsushita, H. Matsumoto, and R. Kawabe. Missing Link Found? The "Runaway" Path to Supermassive Black Holes. *ApJ*, 562:L19–L22, November 2001. doi: 10.1086/338118.

D. J. Eisenstein and P. Hut. HOP: A New Group-Finding Algorithm for N-Body Simulations. *ApJ*, 498:137, May 1998. doi: 10.1086/305535.

C. J. Evans, W. D. Taylor, V. Hénault-Brunet, H. Sana, A. de Koter, S. Simón-Díaz, G. Carraro, T. Bagnoli, N. Bastian, J. M. Bestenlehner, A. Z. Bonanos, E. Bressert, I. Brott, M. A. Campbell, M. Cantiello, J. S. Clark, E. Costa, P. A. Crowther, S. E. de Mink, E. Doran, P. L. Dufton, P. R. Dunstall, K. Friedrich, M. Garcia, M. Gieles, G. Gräfener, A. Herrero, I. D. Howarth, R. G. Izzard, N. Langer, D. J. Lennon, J. Maíz Apellániz, N. Markova, F. Najarro, J. Puls, O. H. Ramirez, C. Sabín-Sanjulián, S. J. Smartt, V. E. Stroud, J. T. van Loon, J. S. Vink, and N. R. Walborn. The VLT-FLAMES Tarantula Survey. I. Introduction and observational overview. *A&A*, 530:A108, June 2011. doi: 10.1051/0004-6361/201116782.

S. A. Farrell, N. A. Webb, D. Barret, O. Godet, and J. M. Rodrigues. An intermediate-mass black hole of over 500 solar masses in the galaxy ESO243-49. *Nature*, 460: 73–75, July 2009. doi: 10.1038/nature08083.

S. A. Farrell, M. Servillat, J. Pforr, T. J. Maccarone, C. Knigge, O. Godet, C. Maraston, N. A. Webb, D. Barret, A. J. Gosling, R. Belmont, and K. Wiersema. A Young Massive Stellar Population around the Intermediate-mass Black Hole ESO 243-49 HLX-1. *ApJ*, 747:L13, March 2012. doi: 10.1088/2041-8205/747/1/L13.

P. C. C. Freire, C. G. Bassa, N. Wex, I. H. Stairs, D. J. Champion, S. M. Ransom, P. Lazarus, V. M. Kaspi, J. W. T. Hessels, M. Kramer, J. M. Cordes, J. P. W. Verbiest, P. Podsiadlowski, D. J. Nice, J. S. Deneva, D. R. Lorimer, B. W. Stappers, M. A. McLaughlin, and F. Camilo. On the nature and evolution of the unique binary pulsar J1903+0327. *MNRAS*, 412:2763–2780, April 2011. doi: 10.1111/j.1365-2966.2010.18109.x.

M. S. Fujii, T. R. Saitoh, and S. F. Portegies Zwart. The Formation of Young Dense Star Clusters through Mergers. *ApJ*, 753:85, July 2012. doi: 10.1088/0004-637X/753/1/85.

E. Gaburov, S. Harfst, and S. Portegies Zwart. SAPPORO: A way to turn your graphics cards into a GRAPE-6. *New Astronomy*, 14:630–637, October 2009. doi: 10.1016/j.newast.2009.03.002.

E. Gaburov, S. Harfst, and S. Portegies Zwart. Sapporo: N-body simulation library for GPUs, October 2012. Astrophysics Source Code Library.

A. Gal-Yam. Luminous Supernovae. *Science*, 337:927–, August 2012. doi: 10.1126/science.1203601.

A. M. Geller, R. de Grijs, C. Li, and J. R. Hurley. Consequences of Dynamical Disruption and Mass Segregation for the Binary Frequencies of Star Clusters. *ApJ*, 779: 30, December 2013. doi: 10.1088/0004-637X/779/1/30.

A. M. Ghez, S. Salim, N. N. Weinberg, J. R. Lu, T. Do, J. K. Dunn, K. Matthews, M. R. Morris, S. Yelda, E. E. Becklin, T. Kremenek, M. Milosavljevic, and J. Naiman. Measuring Distance and Properties of the Milky Way's Central Supermassive Black Hole with Stellar Orbits. *ApJ*, 689:1044–1062, December 2008. doi: 10.1086/592738.

M. Gieles and S. F. Portegies Zwart. The distinction between star clusters and associations. *MNRAS*, 410:L6–L7, January 2011. doi: 10.1111/j.1745-3933.2010.00967.x.

M. Gieles, H. Sana, and S. F. Portegies Zwart. On the velocity dispersion of young star clusters: super-virial or binaries? *MNRAS*, 402:1750–1757, March 2010. doi: 10.1111/j.1365-2966.2009.15993.x.

J. C. Gladstone. The sub-classes of ultraluminous X-ray sources . *Mem. Soc. Astron. Italiana*, 84:629, 2013.

O. Godet, B. Plazolles, T. Kawaguchi, J.-P. Lasota, D. Barret, S. A. Farrell, V. Braito, M. Servillat, N. Webb, and N. Gehrels. Investigating Slim Disk Solutions for HLX-1 in ESO 243-49. *ApJ*, 752:34, June 2012. doi: 10.1088/0004-637X/752/1/34.

O. Godet, J. Lombardi, F. Antonini, N. A. Webb, D. Barret, J. Vingless, and M. Thomas. Implications of the delayed 2013 outburst of the ESO 243-49 HLX-1. *ArXiv e-prints*, August 2014.

D. Gouliermis, S. C. Keller, M. Kontizas, E. Kontizas, and I. Bellas-Velidis. Mass segregation in young Magellanic Cloud star clusters: Four clusters observed with HST. *A&A*, 416:137–155, March 2004. doi: 10.1051/0004-6361:20031702.

E. Gourgoulhon, P. Chamaraux, and P. Fouque. Groups of galaxies within 80 Mpc. I - Grouping hierarchical method and statistical properties. *A&A*, 255:69–86, February 1992.

M. Gritschneder and D. N. C. Lin. Explaining the Observed Velocity Dispersion of Dwarf Galaxies by Baryonic Mass Loss during the First Collapse. *ApJ*, 765:38, March 2013. doi: 10.1088/0004-637X/765/1/38.

J. E. Gunn and J. P. Ostriker. On the Nature of Pulsars. III. Analysis of Observations. *ApJ*, 160:979–+, June 1970. doi: 10.1086/150487.

S. Harfst, A. Gualandris, D. Merritt, R. Spurzem, S. Portegies Zwart, and P. Berczik. Performance analysis of direct N-body algorithms on special-purpose supercomputers. *New Astronomy*, 12:357–377, July 2007. doi: 10.1016/j.newast.2006.11.003.

S. Harfst, S. Portegies Zwart, and A. Stolte. Reconstructing the Arches cluster - I. Constraining the initial conditions. *MNRAS*, 409:628–638, December 2010. doi: 10.1111/j.1365-2966.2010.17326.x.

D. C. Heggie and R. D. Mathieu. Standardised Units and Time Scales. In P. Hut and S. L. W. McMillan, editors, *The Use of Supercomputers in Stellar Dynamics*, volume 267 of *Lecture Notes in Physics, Berlin Springer Verlag*, page 233, 1986. doi: 10.1007/BFb0116419.

V. Hénault-Brunet, C. J. Evans, H. Sana, M. Gieles, N. Bastian, J. Maíz Apellániz, N. Markova, W. D. Taylor, E. Bressert, P. A. Crowther, and J. T. van Loon. The VLT-FLAMES Tarantula Survey. VII. A low velocity dispersion for the young massive cluster R136. *A&A*, 546:A73, October 2012. doi: 10.1051/0004-6361/201219471.

J. G. Hills. The effects of sudden mass loss and a random kick velocity produced in a supernova explosion on the dynamics of a binary star of arbitrary orbital eccentricity - Applications to X-ray binaries and to the binary pulsars. *ApJ*, 267:322–333, April 1983. doi: 10.1086/160871.

D. A. Hunter, E. J. Shaya, J. A. Holtzman, R. M. Light, E. J. O'Neil, Jr., and R. Lynds. The Intermediate Stellar Mass Population in R136 Determined from Hubble Space Telescope Planetary Camera 2 Images. *ApJ*, 448:179, July 1995. doi: 10.1086/175950.

P. Hut, J. Makino, and S. McMillan. Building a better leapfrog. *ApJ*, 443:L93–L96, April 1995. doi: 10.1086/187844.

P. Kaaret and H. Feng. Confirmation of the 62 Day X-Ray Periodicity from M82. *ApJ*, 669:106–108, November 2007. doi: 10.1086/521598.

V. Kalogera. Orbital Characteristics of Binary Systems after Asymmetric Supernova Explosions. *ApJ*, 471:352–+, November 1996. doi: 10.1086/177974.

A. King and J.-P. Lasota. HLX-1 may be an SS433 system. *ArXiv e-prints*, July 2014.

P. Kroupa. On the variation of the initial mass function. *MNRAS*, 322:231–246, April 2001. doi: 10.1046/j.1365-8711.2001.04022.x.

J. B. Kruskal. On the shortest spanning subtree of a graph and the traveling salesman problem. *Proceedings of the American Mathematical Society*, 7:48–50, 1956.

J.-P. Lasota, T. Alexander, G. Dubus, D. Barret, S. A. Farrell, N. Gehrels, O. Godet, and N. A. Webb. The Origin of Variability of the Intermediate-mass Black-hole ULX System HLX-1 in ESO 243-49. *ApJ*, 735:89, July 2011. doi: 10.1088/0004-637X/735/2/89.

J.-F. Liu and J. N. Bregman. Ultraluminous X-Ray Sources in Nearby Galaxies from ROSAT High Resolution Imager Observations I. Data Analysis. *ApJS*, 157:59–125, March 2005. doi: 10.1086/427170.

D. Lynden-Bell. Statistical mechanics of violent relaxation in stellar systems. *MNRAS*, 136:101, 1967.

A. D. Mackey and G. F. Gilmore. Surface brightness profiles and structural parameters for 53 rich stellar clusters in the Large Magellanic Cloud. *MNRAS*, 338:85–119, January 2003. doi: 10.1046/j.1365-8711.2003.06021.x.

N. Madhusudhan, S. Rappaport, P. Podsiadlowski, and L. Nelson. Models for the Observable System Parameters of Ultraluminous X-Ray Sources. *ApJ*, 688:1235–1249, December 2008. doi: 10.1086/592237.

E. M. Malumuth and S. R. Heap. UBV stellar photometry of the 30 Doradus region of the large Magellanic Cloud with the Hubble Space Telescope. *AJ*, 107:1054–1066, March 1994. doi: 10.1086/116917.

H. Matsumoto, I. Tatsuya, T. G. Tsuru, S. Matsushita, K. Watarai, and S. Mineshige. Peculiar Characteristics of the Hyper-Luminous X-Ray Source M82 X-1. *Progress of Theoretical Physics Supplement*, 155:379–380, 2004. doi: 10.1143/PTPS.155.379.

S. McMillan, E. Vesperini, and N. Kruczek. Rapid Mass Segregation in Massive Star Clusters. *ArXiv e-prints*, October 2012.

A. Merloni, P. Predehl, W. Becker, H. Böhringer, T. Boller, H. Brunner, M. Brusa, K. Dennerl, M. Freyberg, P. Friedrich, A. Georgakakis, F. Haberl, G. Hasinger, N. Meidinger, J. Mohr, K. Nandra, A. Rau, T. H. Reiprich, J. Robrade, M. Salvato, A. Santangelo, M. Sasaki, A. Schwope, J. Wilms, and t. German eROSITA Consortium. eROSITA Science Book: Mapping the Structure of the Energetic Universe. *ArXiv e-prints*, September 2012.

G. Meylan. The Properties of 30 Doradus. In G. H. Smith and J. P. Brodie, editors, *The Globular Cluster-Galaxy Connection*, volume 48 of *Astronomical Society of the Pacific Conference Series*, page 588, January 1993.

A. F. J. Moffat, W. Seggewiss, and M. M. Shara. Probing the luminous stellar cores of the giant H II regions 30 DOR in the LMC and NGC 3603 in the Galaxy. *ApJ*, 295:109–133, August 1985. doi: 10.1086/163356.

E. C. Moran, K. Shahinyan, H. R. Sugarman, D. O. Velez, and M. Eracleous. Black Holes at the Centers of Nearby Dwarf Galaxies. *ArXiv e-prints*, August 2014.

P. Mucciarelli, P. Casella, T. Belloni, L. Zampieri, and P. Ranalli. A variable Quasi-Periodic Oscillation in M82 X-1. Timing and spectral analysis of XMM-Newton and RossiXTE observations. *MNRAS*, 365:1123–1130, February 2006. doi: 10.1111/j.1365-2966.2005.09754.x.

T. K. Nakamura. Statistical Mechanics of a Collisionless System Based on the Maximum Entropy Principle. *ApJ*, 531:739–743, March 2000. doi: 10.1086/308484.

T. Okajima, K. Ebisawa, and T. Kawaguchi. A Stellar-Mass Black Hole in the Ultraluminous X-Ray Source M82 X-1? *ApJ*, 652:L105–L108, December 2006. doi: 10.1086/510153.

C. Olczak, R. Spurzem, and T. Henning. Rapid mass segregation in young star clusters without substructure? In N. H. Brummell, A. S. Brun, M. S. Miesch, and Y. Ponty, editors, *IAU Symposium*, volume 271 of *IAU Symposium*, pages 389–390, August 2011. doi: 10.1017/S1743921311017935.

F. Özel, D. Psaltis, R. Narayan, and J. E. McClintock. The Black Hole Mass Distribution in the Galaxy. *ApJ*, 725:1918–1927, December 2010. doi: 10.1088/0004-637X/725/2/1918.

D. R. Pasham, T. E. Strohmayer, and R. F. Mushotzky. A 400-solar-mass black hole in the galaxy M82. *Nature*, 513:74–76, September 2014. doi: 10.1038/nature13710.

A. Patruno and L. Zampieri. Optical emission from massive donors in ultraluminous X-ray source binary systems. *MNRAS*, 386:543–552, May 2008. doi: 10.1111/j.1365-2966.2008.13063.x.

A. Patruno, M. Colpi, A. Faulkner, and A. Possenti. Radio pulsars around intermediate-mass black holes in superstellar clusters. *MNRAS*, 364:344–352, November 2005. doi: 10.1111/j.1365-2966.2005.09568.x.

B. Paxton, L. Bildsten, A. Dotter, F. Herwig, P. Lesaffre, and F. Timmes. Modules for Experiments in Stellar Astrophysics (MESA). *ApJS*, 192:3, January 2011. doi: 10.1088/0067-0049/192/1/3.

F. I. Pelupessy and S. Portegies Zwart. The evolution of embedded star clusters. *MNRAS*, 420:1503–1517, February 2012. doi: 10.1111/j.1365-2966.2011.20137.x.

F. I. Pelupessy, A. van Elteren, N. de Vries, S. L. W. McMillan, N. Drost, and S. F. Portegies Zwart. The Astrophysical Multipurpose Software Environment. *A&A*, 557:A84, September 2013. doi: 10.1051/0004-6361/201321252.

N. Peretto, P. André, and A. Belloche. Probing the formation of intermediate- to high-mass stars in protoclusters. A detailed millimeter study of the NGC 2264 clumps. *A&A*, 445:979–998, January 2006. doi: 10.1051/0004-6361:20053324.

E. S. Phinney. Pulsars as Probes of Newtonian Dynamical Systems. *Royal Society of London Philosophical Transactions Series A*, 341:39–75, October 1992. doi: 10.1098/rsta.1992.0084.

P. Podsiadlowski, N. Langer, A. J. T. Poelarends, S. Rappaport, A. Heger, and E. Pfahl. The Effects of Binary Evolution on the Dynamics of Core Collapse and Neutron Star Kicks. *ApJ*, 612:1044–1051, September 2004. doi: 10.1086/421713.

O. R. Pols and M. Marinus. Monte-Carlo simulations of binary stellar evolution in young open clusters. *A&A*, 288:475–501, August 1994.

S. Portegies Zwart and T. Boekholt. On the Minimal Accuracy Required for Simulating Self-gravitating Systems by Means of Direct N-body Methods. *ApJ*, 785:L3, April 2014. doi: 10.1088/2041-8205/785/1/L3.

S. Portegies Zwart, E. P. J. van den Heuvel, J. van Leeuwen, and G. Nelemans. The Formation of the Eccentric-orbit Millisecond Pulsar J1903+0327 and the Origin of Single Millisecond Pulsars. *ApJ*, 734:55–+, June 2011. doi: 10.1088/0004-637X/734/1/55.

S. Portegies Zwart, S. McMillan, I. Pelupessy, and A. van Elteren. Multi-physics Simulations using a Hierarchical Interchangeable Software Interface. In R. Capuzzo-Dolcetta, M. Limongi, and A. Tornambè, editors, *Advances in Computational Astrophysics: Methods, Tools, and Outcome*, volume 453 of *Astronomical Society of the Pacific Conference Series*, page 317, July 2012.

S. F. Portegies Zwart and S. L. W. McMillan. The Runaway Growth of Intermediate-Mass Black Holes in Dense Star Clusters. *ApJ*, 576:899–907, September 2002. doi: 10.1086/341798.

S. F. Portegies Zwart and E. P. J. van den Heuvel. A runaway collision in a young star cluster as the origin of the brightest supernova. *Nature*, 450:388–389, November 2007. doi: 10.1038/nature06276.

S. F. Portegies Zwart, J. Makino, S. L. W. McMillan, and P. Hut. Star cluster ecology. III. Runaway collisions in young compact star clusters. *A&A*, 348:117–126, August 1999.

S. F. Portegies Zwart, J. Dewi, and T. Maccarone. Intermediate mass black holes in accreting binaries: formation, evolution and observational appearance. *MNRAS*, 355:413–423, December 2004. doi: 10.1111/j.1365-2966.2004.08327.x.

S. F. Portegies Zwart, S. L. W. McMillan, and M. Gieles. Young Massive Star Clusters. *ARA&A*, 48:431–493, September 2010. doi: 10.1146/annurev-astro-081309-130834.

E.-M. Proszkow and F. C. Adams. Dynamical Evolution of Young Embedded Clusters: A Parameter Space Survey. *ApJS*, 185:486–510, December 2009. doi: 10.1088/0067-0049/185/2/486.

E.-M. Proszkow, F. C. Adams, L. W. Hartmann, and J. J. Tobin. Kinematic Signatures of Subvirial Initial Conditions in Young Clusters. *ApJ*, 697:1020–1031, June 2009. doi: 10.1088/0004-637X/697/2/1020.

T. P. Roberts. X-ray observations of ultraluminous X-ray sources. *Ap&SS*, 311:203–212, October 2007. doi: 10.1007/s10509-007-9547-z.

E. Sabbi, D. J. Lennon, M. Gieles, S. E. de Mink, N. R. Walborn, J. Anderson, A. Bellini, N. Panagia, R. van der Marel, and J. Maíz Apellániz. A Double Cluster at the Core of 30 Doradus. *ApJ*, 754:L37, August 2012. doi: 10.1088/2041-8205/754/2/L37.

E. Sabbi, J. Anderson, D. J. Lennon, R. P. van der Marel, A. Aloisi, M. L. Boyer, M. Cignoni, G. de Marchi, S. E. de Mink, C. J. Evans, J. S. Gallagher, III, K. Gordon, D. A. Gouliermis, E. K. Grebel, A. M. Koekemoer, S. S. Larsen, N. Panagia, J. E. Ryon, L. J. Smith, M. Tosi, and D. Zaritsky. Hubble Tarantula Treasury Project: Unraveling Tarantula's Web. I. Observational Overview and First Results. *AJ*, 146:53, September 2013. doi: 10.1088/0004-6256/146/3/53.

E. E. Salpeter. The Luminosity Function and Stellar Evolution. *ApJ*, 121:161, January 1955. doi: 10.1086/145971.

R. Schödel, A. Eckart, C. Iserlohe, R. Genzel, and T. Ott. A Black Hole in the Galactic Center Complex IRS 13E? *ApJ*, 625:L111–L114, June 2005. doi: 10.1086/431307.

F. Selman, J. Melnick, G. Bosch, and R. Terlevich. The ionizing cluster of 30 Doradus. III. Star-formation history and initial mass function. *A&A*, 347:532–549, July 1999.

J. F. Sepinsky, B. Willems, and V. Kalogera. Equipotential Surfaces and Lagrangian Points in Nonsynchronous, Eccentric Binary and Planetary Systems. *ApJ*, 660:1624–1635, May 2007. doi: 10.1086/513736.

I. S. Shklovskii. Possible Causes of the Secular Increase in Pulsar Periods. *Soviet Ast.*, 13:562–+, February 1970.

R. Soria, P. J. Hakala, G. K. T. Hau, J. C. Gladstone, and A. K. H. Kong. Optical counterpart of HLX-1 during the 2010 outburst. *MNRAS*, 420:3599–3608, March 2012. doi: 10.1111/j.1365-2966.2011.20281.x.

D. N. Spergel and L. Hernquist. Statistical mechanics of violent relaxation. *ApJ*, 397:L75–L78, October 1992. doi: 10.1086/186548.

O. Straub, O. Godet, N. Webb, M. Servillat, and D. Barret. Investigating the mass of the intermediate mass black hole candidate HLX-1 with the SLIMBH model. *ArXiv e-prints*, March 2014.

T. M. Tauris and R. J. Takens. Runaway velocities of stellar components originating from disrupted binaries via asymmetric supernova explosions. *A&A*, 330:1047–1059, February 1998.

A. A. Tokovinin. MSC - a catalogue of physical multiple stars. *A&AS*, 124:75–84, July 1997. doi: 10.1051/aas:1997181.

R. A. Treumann and W. Baumjohann. Incomplete-exclusion statistical mechanics in violent relaxation. *A&A*, 558:A40, October 2013. doi: 10.1051/0004-6361/201322122.

E. P. J. van den Heuvel and S. F. Portegies Zwart. Are Superluminous Supernovae and Long GRBs the Products of Dynamical Processes in Young Dense Star Clusters? *ApJ*, 779:114, December 2013. doi: 10.1088/0004-637X/779/2/114.

E. P. J. van den Heuvel and J. van Paradijs. Intrinsic Kicks at Birth Are Required to Explain the Observed Properties of Single and Binary Neutron Stars. *ApJ*, 483: 399–+, July 1997. doi: 10.1086/304249.

A. J. Walsh, P. C. Myers, and M. G. Burton. Star Formation on the Move? *ApJ*, 614: 194–202, October 2004. doi: 10.1086/423425.

N. Webb, D. Cseh, E. Lenc, O. Godet, D. Barret, S. Corbel, S. Farrell, R. Fender, N. Gehrels, and I. Heywood. Radio Detections During Two State Transitions of the Intermediate-Mass Black Hole HLX-1. *Science*, 337:554–, August 2012. doi: 10.1126/science.1222779.

J. C. Wheeler, M. Lecar, and C. F. McKee. Supernovae in binary systems. *ApJ*, 200: 145–157, August 1975. doi: 10.1086/153771.

K. Wiersema, S. A. Farrell, N. A. Webb, M. Servillat, T. J. Maccarone, D. Barret, and O. Godet. A Redshift for the Intermediate-mass Black Hole Candidate HLX-1: Confirmation of its Association with the Galaxy ESO 243-49. *ApJ*, 721:L102–L106, October 2010. doi: 10.1088/2041-8205/721/2/L102.

R. Y. Zhuchkov, O. V. Kiyaeva, and V. V. Orlov. Criteria for the stability of triple systems and their application to observations of multiple stars. *Astronomy Reports*, 54:38–47, January 2010. doi: 10.1134/S1063772910010051.

Curriculum Vitae

I was born on February 23, 1981 in Worcester, Massachusetts in the United States of America. In 1986, I moved to St. Louis, Missouri where I would complete my primary and secondary education. In 2008, I graduated with a Bachelor's degree in Physics from the University of Missouri. After graduation, I began my Master's degree in Physics, with a focus on Astronomy at the University of Missouri with Prof. Dr. Angela Speck. During my time there, I did research in observational Astrophysics, specifically PAHs (Polycyclic Aromatic Hydrocarbons). I was granted time twice, as the primary investigator, on the Gemini North telescope in Hawaii. I was also awarded the Chambliss Medal for exemplary research from the American Astronomical Society for my work on PAH's. I completed my Master's thesis, "Investigating the formation mechanism of Polycyclic Aromatic Hydrocarbons and adapting particle swarm optimization techniques to search large data sets" in 2010. Later that same year I started my PhD position with Prof. Dr. Simon Portegies Zwart at Leiden University in The Netherlands in computational astrophysics.

Acknowledgements

This thesis would not have happened without the friendship, help, guidance, and support of many people to whom I owe a debt of gratitude. This list of thanks is both inadequate to repay the debt and incomplete in its scope.

First, I thank God for the desire to understand and the subject matter to study. It is a truly beautiful creation.

I am blessed to have such a wonderful family. Samantha you have been my friend, support, confidant, and encourager, you have both lifted me up and grounded me. I am thankful everyday for you and your love. My life would be more shallow without you, it is as if you have added a new dimension to my life that I was previously unaware of. And I continue to be thankful that you have graciously yet to realize just how out of my league you are. I hope you have enjoyed our four-year, European honeymoon as much as I have.

Eleanor and Jonas if it were not for you I would have finished this thesis a whole year earlier, but there would be so much less joy in my life, I wouldn't trade a second of it. I am so proud to be your father and I love watching you grow. I cannot wait to teach you about the mysteries of life, the Universe, and everything (well at least somethings).

Mom, thank you for all of your love throughout the years, it has helped form me into the man I have become. I suppose now you cannot give me a hard time about "not finishing my education". Kim and Jerry, thank you for letting me whisk your daughter away to Europe, and for not holding it against me.

Several people played key roles in the work I have done over the past several years. Nathan your support, help, and ideas were fundamental to this thesis and its completion; your friendship has meant a great deal to me, more than you know, and I thank you for giving it so freely. Xander without your wisdom and guidance I would have missed the mark, thank you. Alessandro you have been a wonderful sounding board, whether about the philosophy of science or reassuring me that astronomical numbers are okay in astronomy. Simon thank you

for the opportunity to marvel at the Universe with you and for your scientific insight.

Many work colleges have become close friends. Jeroen and Alex thank you for all the great times and laughs in and out of our office. Jeroen, many thanks for translating the summary to Dutch. I have enjoyed getting to know both of you and I could not have asked for better officemates or friends. Steven I have always enjoyed playing chess with you, as well as your photography, and even your pun-laden humor, thank you for all you have shared with me. Xiaohu, you always have a kind and encouraging word, thank you for friendship. Adrian our conversations have been very enjoyable, as were the dinners and piano music. Thank you for inviting me over. Thank you Edwin for being my HLX-1 buddy, for listening to all of my ideas and only laughing a little. Masaki I wish you many more wonderful late nights, thank you for sharing a few of them with me.

I have been very fortunate to have been in such a dynamic and interesting research group. Arjen, Inti, and Marcell thank you for all of the AMUSE lessons and bug fixes. Tjarda, Thomas, Lucy, Carmon, and the rest of the Castle group (past and present) thank you for the conversations, the challenging thoughts, and the fun times.

I have had the joy of supervising two amazing students, both of whom truly exceeded my expectation. Tjibaria and Huibert thank you both for letting me be a part of your development, and I look forward to seeing what your bright futures hold.

Over the years in Leiden I have had the pleasure of getting to know some wonderful people, both in and out of the University. Evghenii I cannot recall how we first became friends, but I sure am glad that we did; our conversations have been thought provoking and rich with new ideas. Ed, I have shared more meals with you than with anyone I am not related to, and it has been a pleasure to share them with you. Samuël and Kindra thank you both for sharing your life, your families, and Middelburg with us. Chris I remain impressed with your strength and your kindness.

There are several advisors, friends, and teachers from the past who continue to have a strong impact on me. Angela I would never have come this far it were not for your great teaching and for your wonderful mentorship; you have been a bright light in my life. Aigen thank you for the very timely encouragement early on, you gave me strength to continue. Paul, your voice to pursue excellence remains with me.